UNIVERSITÀ DEGLI STUDI DI GENOVA
SCUOLA POLITECNICA DI INGEGNERIA E ARCHITETTURA

Department of Mechanical Engineering, Energy, Management and Transports

DISSERTATION SUBMITTED FOR THE DEGREE OF DOCTOR OF PHILOSOPHY

Model education in the POD space for loss prediction in LPT cascades

Supervisors:

Prof. Simoni Daniele
Prof. Lengani Davide

PhD student:

Yepmo Henang Vianney

November 2020

This page intentionally left blank

Abstract

The present work deals with post-processing by means of Proper Orthogonal Decomposition (POD) of data obtained from experimental investigations on Low-Pressure Turbine (LPT) cascades. The aim is to provide a strategy useful to coarsening design space grids and hence, reduce the data acquisition time during experimental investigations or high-fidelity simulations.

The experimental work has been conducted in a wind tunnel installed at the Laboratory of Aerodynamics and Turbomachinery of the University of Genova. The experimental procedure consists in surveying the flow upstream and downstream of the cascade, aiming to evaluate the total pressure drop through the cascade, and hence the overall losses. Specifically, effects on losses of design parameters such as freestream turbulence intensity, vane solidity, incoming wake parameters (velocity defect, turbulent content and reduced frequency), flow Reynolds number and incidence flow angle have been evaluated.

Then, POD has been applied to data constituted by total pressure loss coefficient distributions in the pitchwise direction under different conditions in order to:

- *highlight the loss trend vs the design space parameter variation*
- *identify the minimum number of requested conditions in the design space, i.e., the number of independent conditions useful for the education of a predictive model*

These objectives have been achieved due to the POD capability in providing compact subspaces able to reproduce the same loss trend observed in the physical space. Moreover, in the POD subspace it has been possible to define a smooth kernel with the number of independent conditions in order to estimate the loss distribution of the remaining conditions. Hence, a model has been educated by means of Least Squares Method (LSM) on the POD design space coefficients choosing the predictors as low order polynomials of the independent variables.

Results will show good agreement between measured and modelled loss distribution varying each design space parameter, showing that the model is able to predict loss distribution within the uncertainty measurement. Furthermore, keeping the same strategy for the education of the kernel on another dataset characterizing the loss distribution of two cascades with different geometrical parameters, loss distribution and magnitude are still well captured. Thus, analysis show that the rank of the problem is much lower than the tested conditions, and consequently a reduced number of tests are really necessary. This technique could be useful to reduce the number of scale-resolving simulations or detailed experiments without significant loss of accuracy.

Content

List of figures

List of tables

Nomenclature

Roman Symbols

c_x	flow axial velocity
C	vane chord
C_f	Skin friction coefficient
C_x	vane axial chord
C_{pt}	total pressure coefficient $= \frac{p_{t,in} - p_{t,ex}}{p_{t,in} - p_{ex}}$
$C_{pt\_reference}$	reference total pressure coefficient
C'_{pt}	deviatoric total pressure coefficient = $C_{pt} - C_{pt\_reference}$
D	bar diameter
f_{bar}	bar passing frequency
f^+	reduced frequency $= \frac{f_{bar}\, C_x}{c_x}$
g	cascade pitch
K	Acceleration parameter
Ma	Mach number
N_{bar}	bar count
N_{ds}	number of combinations defining the design space
N_y	sampling points in the pitchwise direction
p	static pressure
p_t	total pressure
Re	flow Reynolds number
u	bar peripheral velocity
x	axial direction
X	predictor matrix
y	pitchwise direction

Greek Symbols

α	Flow angle
β	fitting coefficients in the POD eigenvectors space
γ	Intermittency function
δ_x	Boundary layer thickness
ϑ	Momentum thickness
λ_ϑ	Momentum thickness acceleration parameter
$\lambda^{(k)}$	POD eigenvalue of mode k
μ	Dynamic viscosity
ν	Kinematic viscosity
σ	Bayesian standard deviation
τ_w	Wall shear stress
$\phi^{(k)}$	POD mode
ϕ_{red}	reduced POD modes matrix
φ	flow coefficient $= \frac{c_x}{u}$
$\chi^{(k)}$	POD eigenvectors of mode k
χ_{red}	reduced POD eigenvectors matrix
ω_p	total pressure loss coefficient $= \frac{\overline{p_{t,in}} - \overline{p_{t,ex}}}{\overline{p_{t,in}} - p_{ex}}$

Superscripts

$\bar{}$	Time-averaged properties
$'$	deviatoric quantities

Subscripts

in	cascade inlet section
ex	cascade outlet section

Acronyms / Abbreviations

BL	Boundary layer
CCA	Constant current anemometer
C_p	Static pressure coefficient
C_{pt}	Total pressure coefficient
CTA	Constant temperature anemometer

DRss	Suction side diffusion rate = $\frac{(Ma_{peak}-Ma_{TE})/Ma_{TE}}{s_{peak}/s_{TE}}$
DNS	Direct Numerical Simulation
FSTI	Freestream turbulence intensity
HWA	Hot wire anemometer
LDV	Laser Doppler Velocimetry
LE	Leading edge
LES	Large Eddy Simulation
LPT	Low-Pressure Turbine
LRR	Low Rank Representation
LSM	Least-Squares Method
N-S	Navier-Stokes
PIV	Particle Image Velocimetry
POD	Proper Orthogonal decomposition
Re	Reynolds number
Re_ϑ	Momentum thickness Reynolds number
Re_x	Reynolds number based on the streamwise coordinate
TE	Trailing edge
Tu	Turbulence intensity
Zw	Incompressible Zweifel number $= 2\frac{g}{C_x}\left[\tan(\alpha_{in})+\tan(\alpha_{out})\right]cos^2(\alpha_{out})$

Chapter 1 Introduction

Although gas turbines (GT) can be considered mature technologies since their conception and have reached a stage where rises in performance are hard to obtain, the engineering community still finds innovative ways to improve their efficiency, weight, noise and operating cost. These improvements must meet the current legislations and regulations established by various countries and international organizations like the Kyoto protocol just to cite an example.

Nowadays, improvements on GT for aeronautical engines are mainly focused on the Low-Pressure Turbine LPT component. In fact, according to Wisler D.C [1], a 1 percent increase in LPT efficiency gives rise to 0.7–0.9 percent increase in engine efficiency. Although the paper dates back 20 years, the LPT performances still hold a major interest, as witnessed by the very wide and recent literature on it [2- 5]. Moreover, for GTs-based turbofan, mainly used in civil aviation, the LPT component is about 1/3 of the weight since it provides at the same time power to the fan and to the first stages of the compressor [6]. Hence, the design of high-efficiency and low-weight LPT is of paramount importance and it needs to take into account many requirements and constraints.

Over the years, both high-fidelity simulations and experimental campaigns have shed light into the physical mechanisms and phenomena affecting the LPT efficiency. Effects of geometrical and flow parameters have been largely investigated in literature aiming to understand and quantify their individual and/or combined effect on LPT performance. For instance, inspection of blade camber line, thickness distribution, blade trailing edge profile has been shown in [2, 6, 7]. Concerning the flow parameters, physical phenomenon like rotor stator interaction, potential flow field has been investigated by Coull et al. [8], Simoni et al. [9] and Michelassi et al. [10]. These studies have all provided deeper characterizations of the flow within LPT modulus and hence, useful information for their aerodynamic optimization.

A current trend in LPT design is the reduction of blade and vane count aiming to satisfy the weight engine constraint. This has led to high and ultra-high-lift blades, characterizing by high levels of diffusion provoking under certain circumstances (low-Reynolds operation) the occurrence of separation in the rear part of suction side of the blades [6, 11]. Hence, the concept of controlled boundary layer diffusion has been introduced in order to mitigate the separated flow effects (see [12] for example). It implies design of either completely laminar blades with very low suction side diffusion, or blades with a so-called roof-top pressure distribution, where transition or laminar separation and turbulent reattachment occur just downstream the suction peak position. Therefore, a focus has been put on the surface velocity (pressure) distribution optimization. For instance, Curtis et al. [6], Coull et al. [13] and Berrino et al. [14] provided parametric studies on the peak velocity position on the suction side vanes; they led to the conclusion that aft-loaded designs had the most limited profile losses for a large range of flow Reynolds number and flow incidence angle in the case of unsteady flows. This configuration also provided the best “robustness” to the incidence flow angle. Moreover, the study of Coull et al. [6] showed that the optimum peak velocity position with a fixed diffusion factor depends on several factors including the

Reynolds number and the reduced frequency. Freestream turbulence can play an effect as well.

The adoption of high-lift blades in LPT modulus has recently also led to secondary flow investigations. In fact, due to the higher cross-passage pressure gradient within the cascade, 3D structures are more intense in the endwall regions and need to be carefully understood in order to accurately account for the overall loss level. Recent studies attribute 30% of aerodynamic losses in modern LPT cascades to secondary flows [15]. Impact of key design parameters on secondary flows in LPT cascades has been for example examined by Coull [2]; by means of RANS simulations in a linear cascade, the author quantified secondary losses while varying design parameters like the flow angles, blade thickness and suction surface aerodynamics. Similar works can be found in the recent literature [16-18].

All the aforementioned investigations usually make a systematic inspection of the effects due to either flow or geometric parameters on LPT efficiency. This operating mode has also been used during the present experimental campaign. Here the effects due to the upstream rotor configuration (bar diameter, spacing and reduced frequency), the vane loading, the flow Reynolds number and the incidence flow angle has been investigated. Tests have been carried out reproducing the real phenomena affecting the LPT operation like the wake-boundary layer interaction process, wake migration and dilation into the potential flow region, potential effects and secondary flow evolution among others. However, the drawback is the increasing, and sometimes unsustainable time necessary to sample either numerically or experimentally, the parameter hyperspace. Therefore, the question if it is possible to reduce the data acquisition time through a compression of the hyperspace dimension raises. Model reduction techniques and specifically Proper Orthogonal Decomposition (POD) could answer this question since they have been largely used in literature to build Low-Rank Representations (LRRs) of high dimensional dataset [19-20]. Particularly, the POD provides a modal decomposition with a limited number of modes, allowing the construction of LRRs.

In the present work, POD has been applied to total pressure loss coefficients acquired for different combinations of design space parameters in order to construct Reduced Order Models (ROMs) and to describe the loss sensitivity to the parameter variation. Indeed, as it will be shown, POD is able to provide a rapid identification of the main causes of losses i.e., the dominant parameter affecting the process of loss generation. From a mathematical point of view, the POD data reduction also identifies the rank of the problem, i.e., the number of tested conditions within the design space really independent.

Using the independent tested conditions, a model has been educated by means of Least Squares Method (LSM) within the POD design space coefficients since it is able to reproduce the same loss trend observed in the physical space. Additionally, prediction of the remaining tested conditions has been done. It will be shown that predicted values are contained within the uncertainty measurement, making this technique attractive to save time during experimental investigations or scale-resolving simulations.

Thesis overview

Chapter 2 will present a review of the literature introducing to the boundary layer evolution within LPT cascades with an emphasize on the wake-boundary layer interaction, since it is

one of the main process affecting the loss generation. Additionally, the effects due to the key parameters on the unsteady flow in LPT cascades will also be presented. The last section of this chapter deals with empirical correlations aiming to evaluate losses in turbomachines.

In Chapters 3 and 4, an in-depth description of the experimental facility as well as the LPT cascades under observation and the instrumentation are provided. Therefore, post-processing techniques will be shown in Chapter 5. An emphasis is placed on the Proper Orthogonal Decomposition (POD) since it is the cornerstone of the present work. In fact, due to the high dimension of the data acquired, POD has been used in order to construct ROMs, and hence reduce the dimension of the original datasets. It will be first present the POD applications in the fluid dynamics community: detection of coherent structures within turbulent flows, loss splitting in LPT cascades and Galerkin projection, among others. Therefore, the mathematical procedure underlying the POD technique will be shown.

Results are shown in Chapter 6; characterization of both turbulence grid and moving bar system by means of phase-locked measurements will be shown first. Therefore, it will be discussed the accuracy of the experimental technique here proposed to evaluate losses characterizing LPT operation and compared with the classical method largely used in literature. The detailed analysis of the observed accuracy for the different combination of the flow parameters will be further discussed. A focus on the Reynolds lapse rate as well as on the effect of freestream turbulence intensity, vane solidity, incidence flow angle and rotor fundamental parameters on losses will be provided. In addition, thanks to the data acquisition technique, discussion about the wakes shedding phenomenon within the vane passage and the background turbulence advection while varying the tested parameters will be provided.

In the second part of this chapter, POD will be applied to loss coefficients acquired for the different combination of the fundamental parameters of the incoming wake driving the unsteady flow operation moving bar system. This aims to find an optimal compact basis which contains the main information of the dataset as well as the number of independent tested conditions within the dataset. Using this POD basis and the independent tested conditions, a smooth kernel will be defined by a fitting procedure aiming to predict losses, i.e., evaluate losses of the dependent tested conditions in the design space. Comparison between both measured and predicted data will show a good agreement. Furthermore, this strategy will be applied to a second dataset of higher dimension than the previous one, made of loss coefficients acquired on two cascades characterized by significantly different deflection and solidity. This aims to check the smooth kernel capability in predicting loss distribution. Once again, modelled data will reproduce well experimental ones, confirming this POD-based technique as an optimal tool to save time during detailed experiments without jeopardizing accuracy.

Chapter 2 Literature review

Losses in LPT cascades are mainly due to both viscous effects and mixing processes [15]. Therefore, a detailed analysis of viscous effects must be considered in order to provide a deeper understanding of the loss generation in real LPT operation.

The present chapter introduces to the boundary layer theory which is well-known to be related to viscous fluids in motion. An emphasis is laid on the boundary layer laminar-to-turbulent transition, the wakes shedding phenomenon within LPT cascades and its impact on the boundary layer transition. Furthermore, an overview of the main literature describing the effects of the background turbulence, the flow Reynolds number and the pressure gradient imposed to the flow on the boundary layer transition and loss processes is reported. At the end of the chapter, correlations aiming to quantify losses, and the effects due to the main parameters on loss generation, are reviewed.

2.1 Introduction to boundary layer

A fundamental concept in fluid dynamics studies of real fluids is the boundary layer, which was first introduced by Ludwig Prandtl in 1904 [21]. According to this theory, when a fluid flows over a given wall, it is possible to identify two distinct regions: the first located sufficiently far from the wall where the viscous effects are negligible and therefore the flow field is governed with a good approximation by the Euler equations (potential flow); the second region is located in the near-wall region. Here, viscous effects are preponderant and high velocity gradients in the wall-normal direction are observed. This region is known as *boundary layer*, usually defined as the portion of fluid in the near-wall region where electro-chemical forces are intense, ensuring the no-slip condition at the wall and a velocity defect in the wall-normal direction. Usually, in order to identify the extension of this region where viscous effects are predominant, it is common to define the boundary layer thickness, known as the portion of fluid which includes 99% of velocity variation compared to the freestream velocity.

Depending on the geometry and the velocity distribution along the main flow direction, the boundary layer has a different evolution and extension. One of the most basic configurations to understand this phenomenon is the flat plate over which a fluid flows (Fig. 2.1). At the plate leading edge, the flow has a uniform velocity. Downstream of the leading edge and moving in the flow direction, it is possible to distinguish three different conditions (states) of the boundary layer:

- *laminar boundary layer*: the fluid motion is well organized as the fluid particles have a parallel motion. Specifically, the flow creates less skin friction and it is less stable
- *transitional boundary layer*: the flow is in part laminar and in part turbulent. There are some fluctuations within the fluid layer due to the intermittence switch from the laminar to the turbulent condition
- *turbulent boundary layer*: characterized by fluid oscillations which tend to disrupt the organized motion; this leads to swirls and eddies of different sizes. However, a

portion of fluid, very close to the wall, namely *viscous sub-layer* or *laminar substrate*, is still present. Here the viscous forces are still predominant

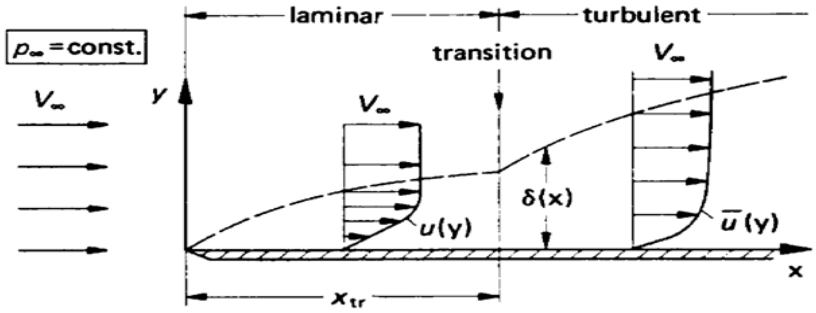

Fig. 2.1 Boundary layer evolution over a flat plate

As it can be seen in Fig. 2.1, each zone is characterized by a different growth rate in the flow direction. Specifically, the laminar boundary layer is subject to a lower growth rate compared to the turbulent one due to the different mixing process between the adjacent portions of fluid, which is more intense in the turbulent state.

The flow around a given body or within a channel is usually resolved using the mass, momentum (Navier-Stokes equations) and energy conservation equations. However, this approach presents considerable numerical efforts and therefore simplified analysis have been developed over the years, based on opportune hypotheses relating to the phenomenon under observation while keeping a similarity between the real physical and the mathematical model. In the case of the boundary layer evolution over a flat plate, Blasius [22] provided a theoretical solution of a simplified mathematical model. He obtained a self-similar solution for the boundary layer equations, formulated in terms on non-dimensional vorticity function, shown in Fig. 2.2 where η and $f'(\eta)$ are similarity functions.

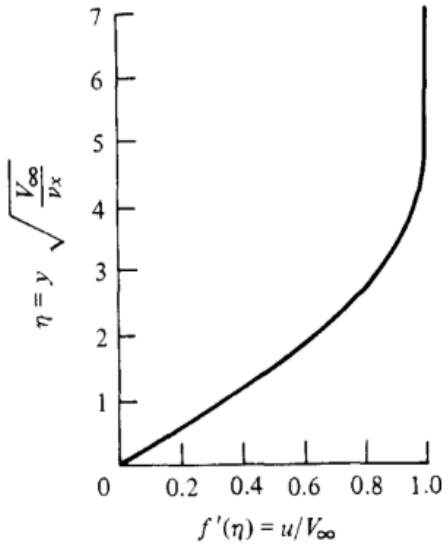

Fig. 2.2 The Blasius self-similar velocity profile in a laminar boundary layer developing on a flat plate with zero incidence.

Furthermore, he predicted the growth of the boundary layer thickness as a function of the distance *x* from the plate leading edge according to:

$$\delta_x = \frac{5\,x}{Re_x^{1/2}} \tag{2.1}$$

Another parameter useful to characterize the boundary layer is the skin friction coefficient C_f defined as the ratio between the wall shear stress τ_w and the dynamic load $\frac{1}{2}\rho_\infty U_\infty^2$. Blasius predicted the following equation

$$C_{f,lam} = \frac{0.664}{Re_x^{1/2}} \tag{2.2}$$

As it can be seen, the laminar boundary layer thickness over a flat plate grows as $x^{1/2}$.

Moving downstream along the plate of Fig. 2.1, the local Reynolds number becomes sufficiently high to induce transition to turbulent state. In this case, the Blasius solution is no longer accurate and prediction of δ_x and C_f in the case of fully developed turbulent boundary layer can be done according to empirical (or semi-empirical) correlations:

$$\delta_x = \frac{0.37x}{Re_x^{1/5}} \tag{2.3}$$

$$C_{f,turb} = \frac{0.074}{Re_x^{1/5}} \tag{2.4}$$

The turbulent boundary layer thickness grows faster than the laminar one since it varies as $x^{4/5}$. The friction coefficient is instead proportional to $Re^{-1/5}$ (Prandtl's law), yielding to larger friction drag coefficient.

The lack of an exact similarity solution for the turbulent boundary layer is due to the occurrence of a viscous sub-layer near the wall where the viscous effects dominate. More specifically, three different regions with different growth and velocity distribution can be identified in a turbulent boundary layer: the viscous sub-layer, the buffer layer and the logarithmic layer, as shown in the plot reported in Fig.2.3. These three flow regions are defined as a function of the wall distance expressed in terms of the dimensionless coordinate $y^+ = \frac{y}{\nu}\sqrt{\frac{\tau_w}{\rho}}$. The velocity corresponding to each of these three regions is instead expressed in terms of the dimensionless velocity $u^+ = u\sqrt{\frac{\rho}{\tau_w}}$, where $\sqrt{\frac{\tau_w}{\rho}}$ is the so-called friction velocity u_τ, that is $u^+ = \frac{u}{u_\tau}$. In the viscous sub-layer ($y^+ < 5$), u^+ is directly proportional to

y^+. In this region the flow is laminar due to the high influence of viscosity near the wall. For $y^+ > 30$ there is the so-called logarithmic zone, in which the flow can be considered turbulent and subjected to strong velocity fluctuations in both intensity and direction. In this region, the logarithmic law is valid and u^+ is proportional to the logarithm of y^+, that is $u^+ = \frac{1}{k}\ln(y^+) + C^+$ where k and C^+ are the von Karman constants. The zone between the viscous and the logarithmic layers, called buffer zone, has gradually changing properties from the viscous to the logarithmic regions.

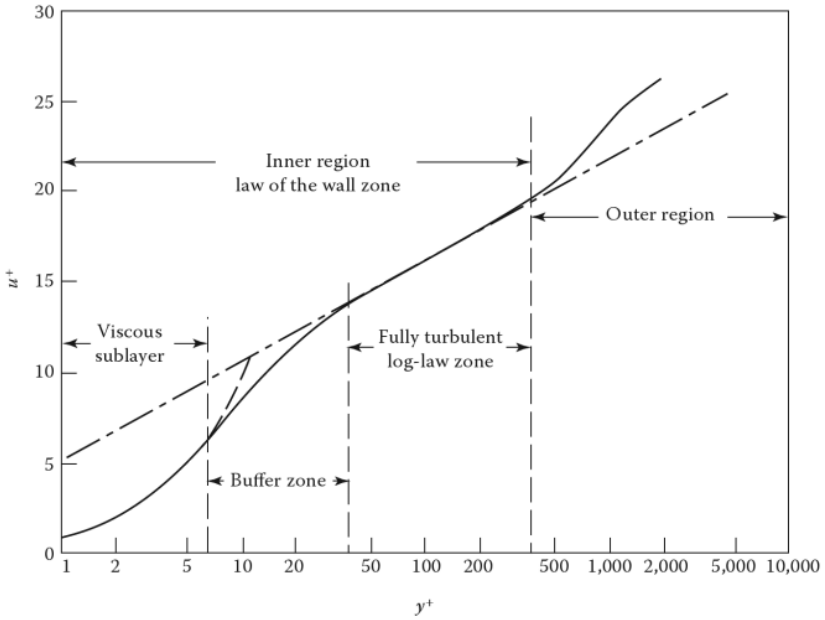

Fig. 2.3 Viscous sublayer (y^+<5), Buffer layer (5<y^+<30) and Fully turbulent or Log-low region (y^+> 30).

2.1.1 Differential equations of the boundary layer

The differential equations governing the boundary layer evolution comes from a simplified version of the Navier-Stokes equations. For a three-dimensional incompressible viscous flow, they assume the following form:

$$\frac{\partial u}{\partial t} + u\frac{\partial u}{\partial x} + v\frac{\partial u}{\partial y} + w\frac{\partial u}{\partial z} = -\frac{1}{\rho}\frac{\partial p}{\partial x} + \nu\left(\frac{\partial^2 u}{\partial x^2} + \frac{\partial^2 u}{\partial y^2} + \frac{\partial^2 u}{\partial z^2}\right) \tag{2.5}$$

$$\frac{\partial v}{\partial t} + u\frac{\partial v}{\partial x} + v\frac{\partial v}{\partial y} + w\frac{\partial v}{\partial z} = -\frac{1}{\rho}\frac{\partial p}{\partial y} + \nu\left(\frac{\partial^2 v}{\partial x^2} + \frac{\partial^2 v}{\partial y^2} + \frac{\partial^2 v}{\partial z^2}\right) \tag{2.6}$$

$$\frac{\partial w}{\partial t} + u\frac{\partial w}{\partial x} + v\frac{\partial w}{\partial y} + w\frac{\partial w}{\partial z} = -\frac{1}{\rho}\frac{\partial p}{\partial z} + \nu\left(\frac{\partial^2 w}{\partial x^2} + \frac{\partial^2 w}{\partial y^2} + \frac{\partial^2 w}{\partial z^2}\right) \tag{2.7}$$

$$\frac{\partial u}{\partial x} + \frac{\partial v}{\partial y} + \frac{\partial w}{\partial z} = 0 \tag{2.8}$$

These equations lead to the following ones in the case of two-dimensional steady flows:

$$u\frac{\partial u}{\partial x} + v\frac{\partial u}{\partial y} = -\frac{1}{\rho}\frac{\partial p}{\partial x} + \nu\left(\frac{\partial^2 u}{\partial x^2} + \frac{\partial^2 u}{\partial y^2}\right) \tag{2.9}$$

$$u\frac{\partial v}{\partial x} + v\frac{\partial v}{\partial y} = -\frac{1}{\rho}\frac{\partial p}{\partial y} + \nu\left(\frac{\partial^2 v}{\partial x^2} + \frac{\partial^2 v}{\partial y^2}\right) \tag{2.10}$$

$$\frac{\partial u}{\partial x} + \frac{\partial v}{\partial y} = 0 \tag{2.11}$$

The system above can be further manipulated by introducing some simplifications based on considerations about the orders of magnitude of each term in the equations, as first suggested by Prandtl. More specifically, since within the boundary layer the wall-normal derivatives are significantly higher than the streamwise ones as well as $v << u$, the above system of equations can be further simplified obtaining:

$$u\frac{\partial u}{\partial x} + v\frac{\partial u}{\partial y} = -\frac{1}{\rho}\frac{\partial p}{\partial x} + \frac{1}{\rho}\frac{\partial}{\partial y}\left(\mu\frac{\partial v}{\partial y}\right) \tag{2.12}$$

$$\frac{\partial p}{\partial y} = 0 \tag{2.13}$$

$$\frac{\partial u}{\partial x} + \frac{\partial v}{\partial y} = 0 \tag{2.14}$$

From eq. 2.13, it is evident that within the boundary layer pressure does not change in the wall-normal direction, i.e., the pressure in the boundary layer can be determined by means of the inviscid theory.

The self-similar solution of Blasius shown previously is obtained from eqs. 2.12 and 2.14 through the definition of the self-similar variables $\eta = \frac{y}{\delta(x)} = y\sqrt{\frac{V_\infty}{\nu x}}$ and $\psi = f(\eta)\sqrt{\nu x V_\infty}$. The variable ψ is the streamline function which satisfies eq. 2.14. Therefore, $u = \frac{\partial \psi}{\partial y} = V_\infty f'(\eta)$ and $v = -\frac{\partial \psi}{\partial x} = \frac{1}{2}\sqrt{\frac{V_\infty}{\nu x}}[\eta f'(\eta) - f(\eta)]$. Substitution into eq. 2.12 provides the Blasius equation

$$2f'''(\eta) + f''(\eta)f(\eta) = 0 \tag{2.15}$$

Solution of eq. 2.15 shown in Fig. 2.2 can be therefore obtained once fixed the boundary conditions, i.e., $f(0) = 0$, $f'(0) = 0$ and $f'(\infty) = 1$. Note that Blasius equation is obtained with zero pressure gradient in the streamwise direction. The more general form for laminar flow is known as Falkner-Skann equation.

For turbulent boundary layers, the equations keep a similar formulation to the laminar case, with the addition of new terms describing the effects of turbulence into the momentum equations. In order to derive the equations for the turbulent case, the velocity components and pressure appearing in the N-S equations need to be decomposed into a mean over time value and a fluctuating component, according to the well-known Reynolds decomposition:

$$u(t) = \bar{u} + u' \tag{2.16}$$

$$p(t) = \bar{p} + p' \tag{2.17}$$

Where $\bar{u}$ and $\bar{p}$ are the mean values, constant over time and defined as $\bar{u} = \lim_{t\to\infty} \frac{1}{t}\int_0^t u(\tau)\, d\tau$ and $\bar{p} = \lim_{t\to\infty} \frac{1}{t}\int_0^t p(\tau)\, d\tau$ respectively.

Substituting the definition of u(t) and p(t) given by eqs. 2.16 and 2.17 in the two-dimensional Navier-Stokes equations and averaging the whole set of equations the Reynolds Averaged Navier-Stokes (RANS) equations for turbulent flows can be obtained:

$$\bar{u}\frac{\partial \bar{u}}{\partial x} + \bar{v}\frac{\partial \bar{u}}{\partial y} = -\frac{1}{\rho}\frac{\partial \bar{p}}{\partial x} + \frac{1}{\rho}\frac{\partial}{\partial x}\left(\mu\frac{\partial \bar{u}}{\partial x} - \rho\overline{u'^2}\right) + \frac{1}{\rho}\frac{\partial}{\partial y}\left(\mu\frac{\partial \bar{u}}{\partial y} - \rho\overline{u'v'}\right) \tag{2.18}$$

$$\bar{u}\frac{\partial \bar{v}}{\partial x} + \bar{v}\frac{\partial \bar{v}}{\partial y} = -\frac{1}{\rho}\frac{\partial \bar{p}}{\partial y} + \frac{1}{\rho}\frac{\partial}{\partial x}\left(\mu\frac{\partial \bar{v}}{\partial x} - \rho\overline{u'v'}\right) + \frac{1}{\rho}\frac{\partial}{\partial y}\left(\mu\frac{\partial \bar{v}}{\partial y} - \rho\overline{v'^2}\right) \tag{2.19}$$

$$\frac{\partial \bar{u}}{\partial x} + \frac{\partial \bar{v}}{\partial y} = 0 \tag{2.20}$$

where the new terms $\overline{u'v'}$, $\overline{u'^2}$ and $\overline{v'^2}$ are respectively the tangential and normal components of the Reynolds stress tensor responsible for the time averaged stresses induced in the fluid by turbulent fluctuations. Applying now the same considerations on the orders of magnitude applied in the laminar case, the system of RANS equations can be simplified, obtaining the equations for the turbulent boundary layer:

$$\bar{u}\frac{\partial \bar{u}}{\partial x} + \bar{v}\frac{\partial \bar{u}}{\partial y} = -\frac{1}{\rho}\frac{\partial \bar{p}}{\partial x} + \frac{1}{\rho}\frac{\partial}{\partial y}\left(\mu\frac{\partial \bar{u}}{\partial y} - \rho\overline{u'v'}\right) \tag{2.21}$$

$$\frac{\partial \bar{p}}{\partial y} = 0 \tag{2.22}$$

$$\frac{\partial \bar{u}}{\partial x} + \frac{\partial \bar{v}}{\partial y} = 0 \tag{2.23}$$

As in the laminar boundary layer, the turbulent one shows a negligible pressure gradient in the wall-normal direction. The set of equations shows the presence of an additional term, namely $-\rho\overline{u'v'}$ which is known as the tangential term of the Reynolds stress tensor in the case of two-dimensional flows.

2.1.2 Steady flow transition

The boundary layer transition governs the laminar-to-turbulent passage. The parameter of greatest importance of this phenomenon is the flow Reynolds number, i.e., the ratio between the inertia forces and the viscous ones. For high values of this parameter, viz. when the inertial forces are greater than the viscous ones, turbulent spots are generated within the boundary layer and they will grow leading to a turbulent state.

The transition mechanism usually occurs in three different ways, as explained in [23, 24]

- natural transition
- by-pass transition
- separated flow transition

a) Natural transition

This transition mode usually occurs at low FSTI values (FSTI <0.1%). When the Reynolds number exceeds a critical value, the laminar boundary layer self-amplifies small disturbances at a fixed frequency (Tollmien-Schlichting waves shown in region 1 of Fig. 2.4). In this case, boundary layer is characterized by a linear growth of the disturbances in the first phase (e.g., Linear Stability Theory which is the basis of the Orr-Sommerfeld equation). These perturbations expand and generate turbulent spots that coalesce and form an entirely turbulent boundary layer at the end of the transition. However, due to the highly disturbed environment characteristic of LPT cascades, the boundary layer that develops in this component is generally not subject to this transition mode.

b) By-pass transition

In this case, the presence of disturbances such as high freestream turbulence or surface roughness do not allow the formation of Tollmien-Schlichting waves and the transition occurs through the direct formation of turbulent spots. In this specific case, regions 1, 2 and 3 shown in Fig. 2.4 are bypassed. This transition mode involves a reduced length of the unstable zone and anticipates the transition to the turbulent regime, as shown in Fig. 2.4.

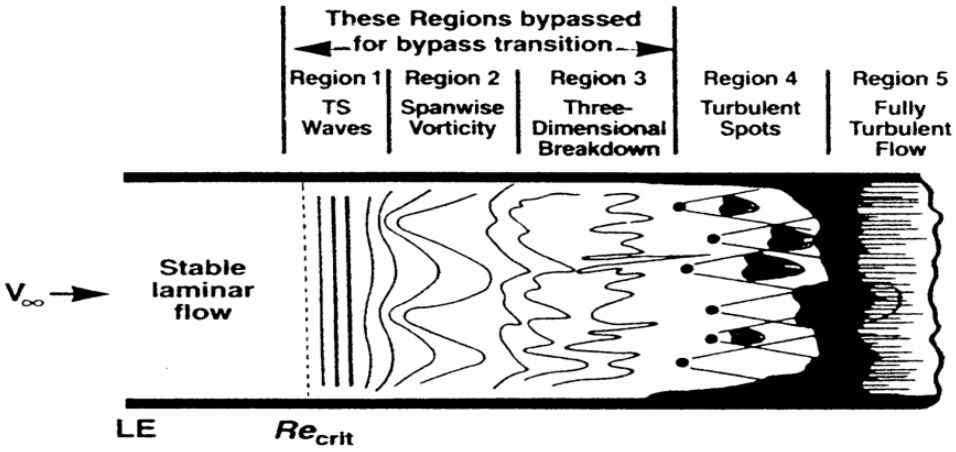

Fig. 2.4 Natural and by-pass transition modes

The by-pass transition represents the most common transition mechanism in turbines given the high level of turbulence within these components. For this reason, this mechanism deserves a detailed explanation.

The direct formation of turbulent spots leading to by-pass transition is a very complex mechanism which is achieved through the formation and break-up of particular flow structures extended in the streamwise direction called "*Klebanoff streaks*" [25], which are localized high and low speed streamwise elongated filaments embedded within the boundary layer. This transition process starts from the disturbance inherently present in the freestream. Since the boundary layer is sensitive only to the low-frequency disturbances present in the freestream, it carries out a filtering operation of the high-frequency disturbances according to a process known as shear-sheltering of the boundary layer. This process by which external disturbances generate instability in the boundary layer is known as receptivity. Once the low-frequency disturbances penetrate the boundary layer, they undergo an amplification process that leads to the formation of streaky structures. High and low speed streaks introduce a strong non-homogeneity in the momentum distribution within the boundary layer, as visible in Fig. 2.5. The streaky structures are then subject to an instability phenomenon leading to their breakdown with consequent generation of turbulent spots within the boundary layer, characteristic of the transition inception. Specifically, according to DNS of Jacobs and Durbin [26], the breakdown of streaky structures is due to the migration of low-speed streaks toward the boundary layer edge, followed by their interaction with the non-penetrating high frequency structures carried by the freestream. During their breakdown, the streaks undergo two types of instability: sinuous and varicose. In the first case, the streaky structures have a sinuous motion, while in the second they undergo a succession of contractions and elongations in all the directions. An example of a streak with sinuous motion is shown in Fig. 2.6. Here, the structure undergoes both lift-up and ejection from the wall with a consequent formation of a small structure on its flank, which leads to the formation of a hairpin vortex, well-known in literature to be typical of turbulent boundary layer. By the time further hairpin vortices will be formed inducing high normal and spanwise velocity fluctuations inside the flow, sustaining the turbulence activity.

It should also be noted that the instability process that leads to this transition mode is influenced by the interaction between the different streaks present in the boundary layer

itself. To make this concept clearer, the flow evolution in a plane orthogonal to the wall at various locations in the transitional zone is shown Fig. 2.7. Contours indicate the streamwise component of the perturbation velocity while the arrow on the left indicates the boundary layer thickness. It can be seen the large-scale freestream penetration into the boundary layer at $Re_\theta = 222$ leading to the formation of streaky structures in the near-wall region. Both low-speed streaks (dark patches) and high-speed streaks (white patches) are therefore visible within the boundary layer and they are randomly distributed over the spanwise direction. Furthermore, as Re_θ increases low-speed streaks become more unstable and extended in both directions. Therefore, interaction with the freestream turbulence occurs as well as interaction with adjacent streaks. The last plot shows that breakdown has filled the boundary layer, and turbulent spots would be detected near the wall.

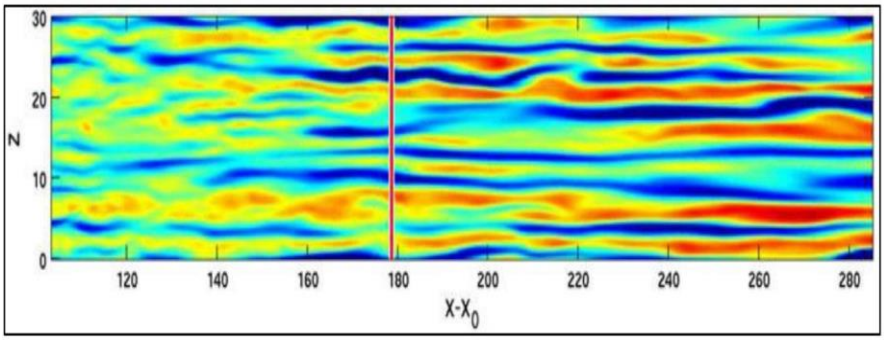

Fig. 2.5 Klebanoff streaks (in red high-speed-streaks and in blue low-speed-streaks)

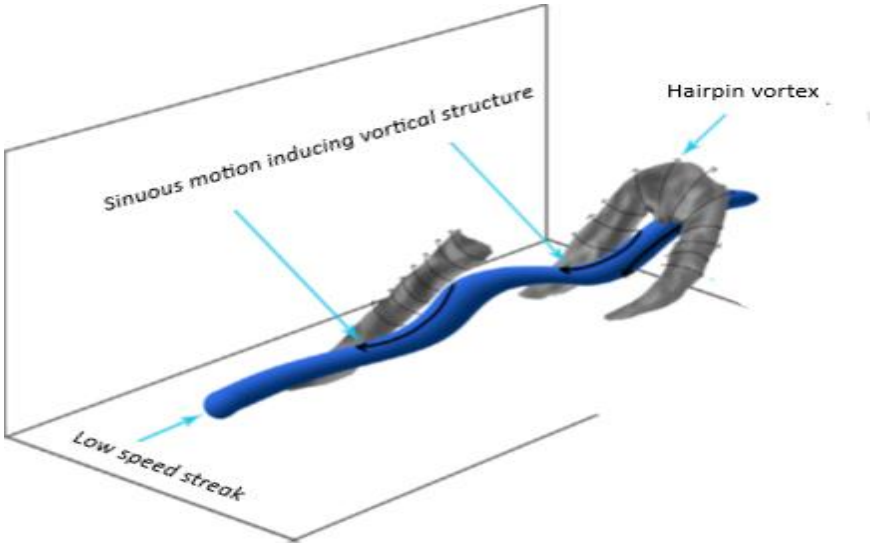

Fig. 2.6 Pictorial representation of the motion of a low-speed streak in the boundary layer

This provides evidence of that by-pass transition originates near the boundary layer edge after a complex mechanism including lift-up of the streaky structures, low-speed streaks freestream interaction and streaky structures interaction, leading to the formation of coherent structures typical of turbulent boundary layer. Recent works further characterize the role of the streaks in the by-pass transition mode of the boundary layer over flat plate geometries

under steady inflow conditions [27-28]. In the case of LPT, the situation is more complex as it will be shown later, due to large number of parameters which influence the transition process.

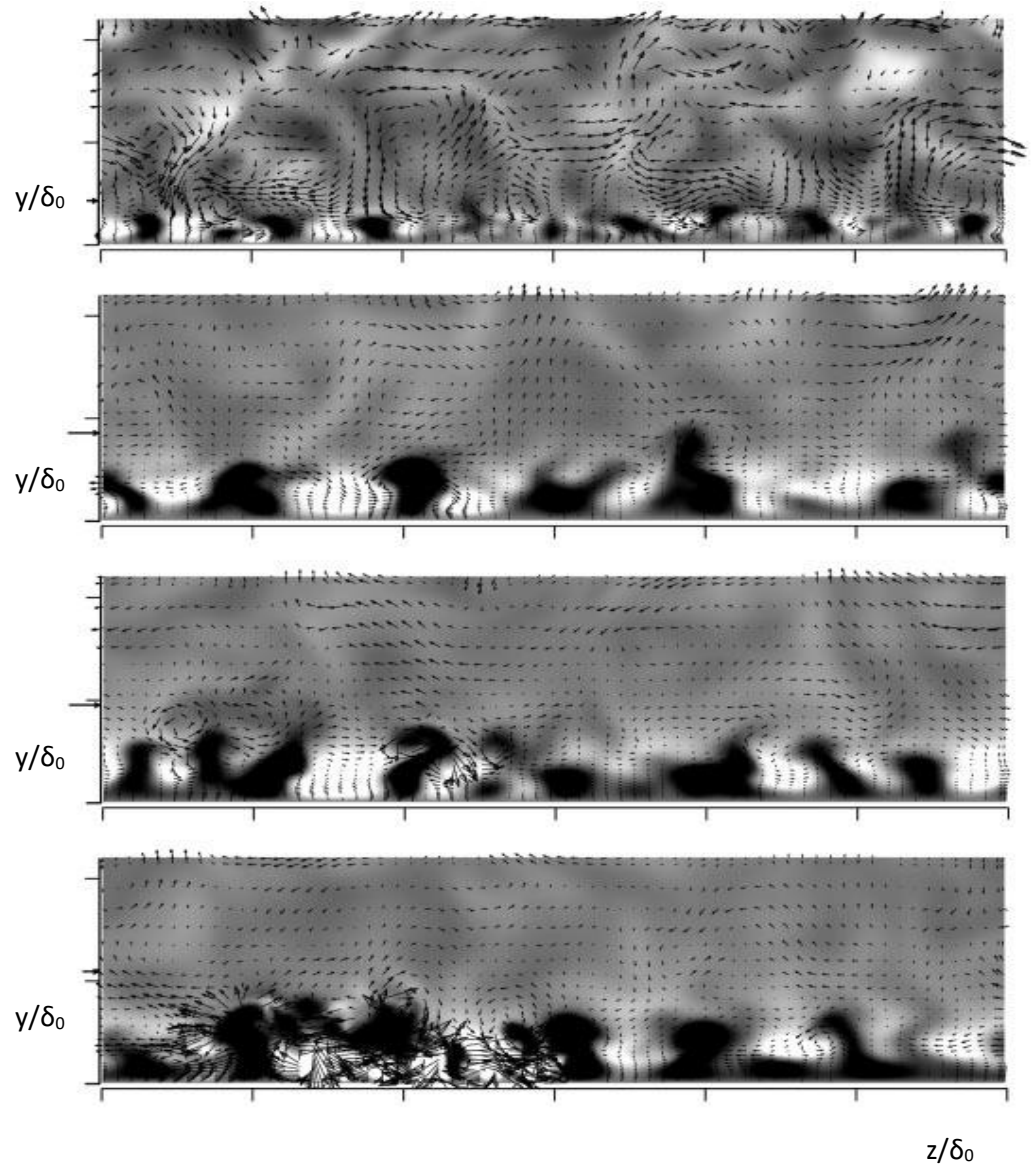

Fig. 2.7 Interaction between low-speed structures and freestream. Sequence of sections at Re_θ = 222, 331, 364 and 403. [26]

The breakup of streaky structures leads to the formation of turbulent spots. In literature, they were first introduced by Emmons [29] in order to describe the development of the last stage of transition. Turbulent spots are triangular in shape and spread at an angle of about 22°, as shown in Fig. 2.8. ~~One important property of turbulent spots is the self-similarity, i.e.,~~ The spot leading and trailing edges propagate at two different velocities, respectively $0.88\,U_\infty$ and $0.5\,U_\infty$, as experimentally detected by Schubauer and Klebanoff [30] in the case of a zero-pressure gradient flow. This different propagation of the leading and trailing edges of the spots has been confirmed over the years by other authors (see [31] for instance). Moreover, since the spots spread longitudinally and laterally, spots originating from different locations

merge to form a continuous turbulent boundary layer. The spots are then followed by a region unreceptive to disturbances and characterized by high values of shear stress, namely the calmed zone. This region moves at a velocity that is about 0.3 of the freestream velocity and it avoids an abrupt discontinuity between the turbulent velocity profile at the rear of the turbulent spots and the undisturbed laminar velocity profile. It is a laminar-like region with a full velocity profile and hence it is more resistant to the flow separation than the laminar boundary layer as shown by Schubauer and Klebanoff [30], Hodson and Howell [32] among others.

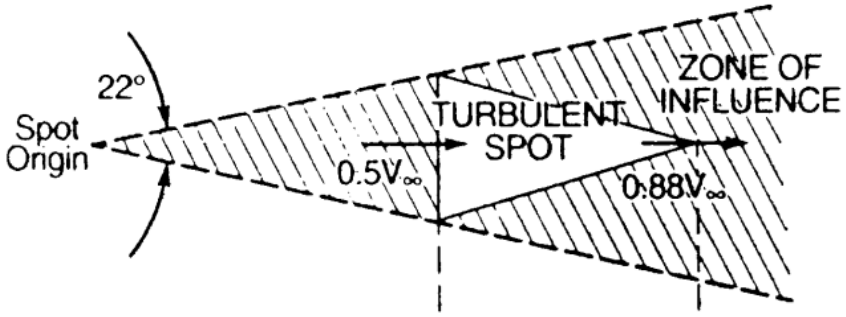

Fig. 2.8 Schematic view of a turbulent spot

c) Separated flow transition

The last transition mode is the separated one, which occurs when the laminar boundary layer separates from the wall (Fig. 2.9). Hence, there is a separation bubble characterized by low shear stress and a constant static pressure value. Hatman and Wang [33-36] defined three separated flow transition modes:

- *transitional separation mode*: in this case, the transition onset occurs before the separation point through the formation of Tollmien-Schlichting waves within the attached flow. Into the separated shear layer, the Kelvin-Helmholtz instabilities provoke a vortex shedding process. This vortex shedding together with the transitional shear layer accelerates the flow turbulent reattachment. According to Hatman and Wang, this kind of separation usually occurs when $Re_{\theta\_sep} > 320$.
- *laminar separation short mode*: The transition onset occurs downstream of the separation point. In this case characterized by moderate flow Reynolds number and mild adverse pressure gradient, the disturbances introduced within the separated boundary layer activate the Kelvin-Helmholtz instabilities. They are represented by large-scale coherent structures, which break-up into small-scale structures characterized by random evolution. These latter induce the boundary layer transition in the free shear-layer as they are ejected from the near-wall region enhancing a turbulent mixing with a consequent turbulent reattachment. This separation mode usually occurs when $240 < Re_{\theta\_sep} < 320$.
- *laminar separation long mode*: same dynamics as the short mode, the only difference is the extension of the separated bubble since it is characterized by low flow Reynolds number and strong adverse pressure gradient

Usually in LPT, due to the operating condition, it is common to observe the second type of separated flow transition, namely laminar separation short mode. This leads to the formation

of short bubbles over the LPT vanes, and if there is an opportune variation of external disturbances, they can undergo a change to long bubbles: this process is known as bubble bursting.

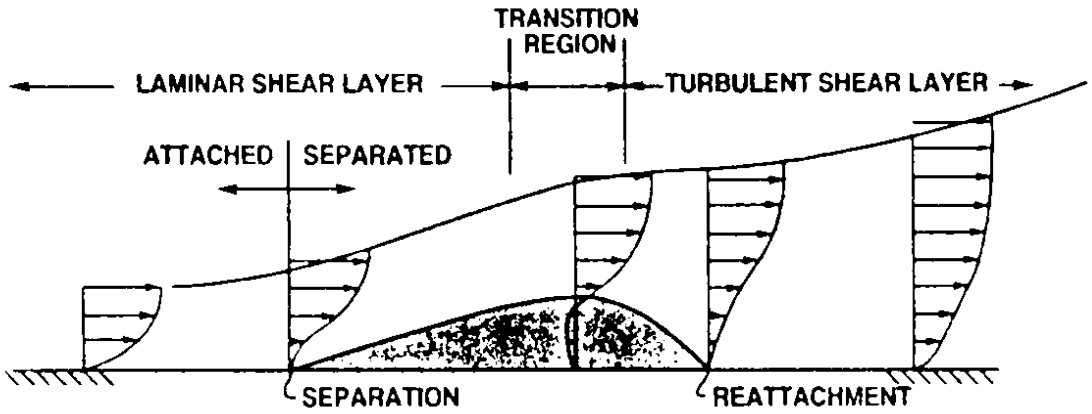

Fig 2.9 Time-averaged structure of separation bubble

In LPT cascades, the laminar-to-turbulent transition is more complex due to the wide range of parameters affecting the transition phenomenon like the adverse pressure gradient, the freestream turbulence intensity level, the surface roughness just to cite a few examples. All these parameters, in addition to the wakes shed from the upstream cascades make the transition process an extremely complex phenomenon.

2.1.3 Wake-boundary layer transition

The highly disturbance environment characterizing the LPT cascade operation makes the laminar-to-turbulent transition phenomenon more complex than what explained in the previous subsection.

Speidel [37] was one of the firsts to provide a work on the wake-boundary layer interaction. He conducted experiments on a symmetrical airfoil with a flow with a fixed value of FSTI in order to quantify the airfoil performance. At that time, he simulated the periodic unsteady phenomenon with a wire oscillating in the pitchwise direction and found out that losses were a function of a reduced frequency parameter according to

$$\omega = \Omega \frac{s}{U} \tag{2.24}$$

Where s is the distance over which the wakes affect the transition process, U is the mean velocity over the surface and Ω the wake frequency. Therefore, he found out the increase in losses with respect to the steady case, which was directly related to the wakes shedding frequency.

Over the years, qualitative investigations of this phenomenon have been yielded in order to complete the quantitative analysis of Spiedel. For instance, Meyer [38] argued that the wakes shed by a cascade can be assimilated in the relative framework to negative-jets superimposed

to the freestream and are ‘’*chopped into segments*’’ as they convect into the downstream cascade. These segments are consequently pushed toward the blade suction side due to the high cross-pressure gradient characteristic of LPT cascades, leading to an excitation of the suction side boundary layer with a consequent alteration of its spatio-temporal evolution (see the sketch of Fig. 2.10). Subsequent works of have confirmed this theory (see [32, 39-40] for example).

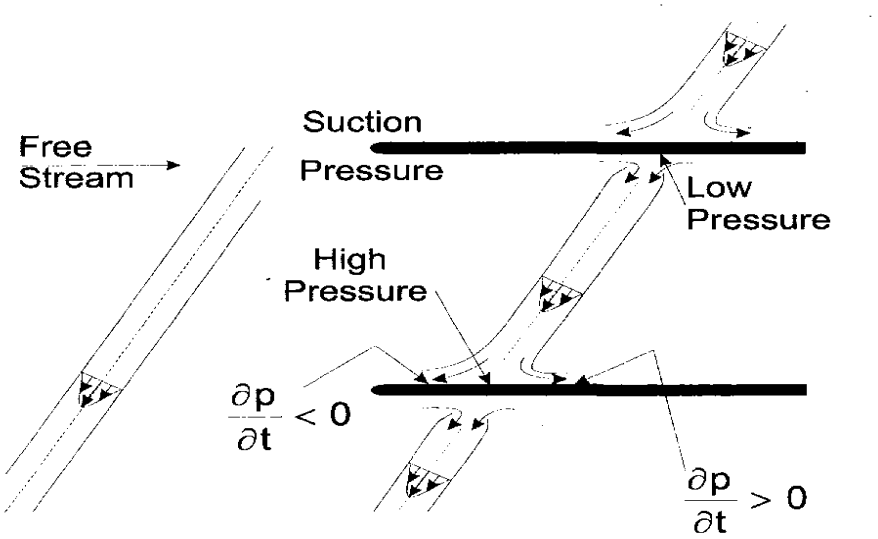

Fig. 2.10 Wake-induced jet effects from [40]

Some years later, Pfeil and Eifler [41] showed that the wake of cylindrical bars and turbine blades are nearly the same in terms of velocity profile and drag. This has led, in the case of cascade testing, to the simplification of the upstream rotors with a rotating mechanism made of cylindrical bars, mainly used nowadays in experimental investigations. Moreover, this bar system is easy to construct and cheaper compared to a real rotor, making it affordable to experimental campaigns. Usually, the choice of the bar diameter depends on the total pressure losses of the blade row to simulate and can be expressed as:

$$Y_p = \frac{c_d\, d}{g_{bar} \cos \beta_1} \tag{2.25}$$

Where c_d is the aerodynamic drag coefficient of a cylinder (function of the flow Reynolds number), g_{bar} the bar pitch at the cascade midspan and β_1 the inlet relative flow angle and d the bar diameter.

Recently, due to the increase of computer power and the improvement of measuring techniques, further insights on the wake advection into LPT cascades have been provided in the literature [10, 32, 42-45]. All these works suggested that the wakes kinematic is characterized by bowing, tilting and distortion during its convection into the cascade. Fig. 2.11, taken from Stieger and Hodson [44] shows the velocity vectors at six equally spaced time instants during the wake propagation cycle. These velocity vectors are the phase-locked perturbation velocity relative to the time-mean flow. Wake bowing can be observed in Fig.

2.11 (a)-(b) near the cascade leading edge and it is due to the different velocities in the mid-passage and near the blade walls. The cross-pressure gradient characteristic of LPT cascades induces both tilting and distortion observed in Fig. 2.11 (c)-(e). These processes lead to the formation of the jet structure concept introduced by Meyer, with a fluid accumulation in the rear part of the suction side and a consequent introduction of the turbulent finer scales carried by the incoming wakes into the boundary layer (see Fig. 2.11 (d)-(f)). This enhances the formation of a dense population of streaky structures and hence, leads to an anticipated transition mechanism of the suction side boundary layer when compared to the no wakes case. Moreover, Fig. 2.11 shows two regions of swirling flows at the wake apex labelled D and E, which appear once the wake is distorted within the cascade. They are regions of high turbulence activity and turbulence production rate, consequence of the work done by the turbulent stresses into the wake and the deformation of the main flow.

The analogy of the steady state by-pass transition and the wake-induced transition is clearly highlighted in the plot shown in Fig. 2.12, taken from Pfeil et al. [46]. Here $x_{o;tr}$ and $x_{o;Tr}$ indicate respectively the beginning and the end of by-pass transition while $x_{f;tr}$ and $x_{f;T\,r}$ are related to the wake-induced transition. The reader can easily observe the anticipated formation of turbulent spots when incoming wakes are present and the calmed region, which immediately follows the spot trailing edge. Specifically, disturbances carried by incoming wakes after an initial receptivity phase evolve rapidly into turbulent spots which promote the boundary layer transition, making this transition mechanism similar to the by-pass one observed in the steady case. Hence, the incoming wakes anticipate the transition process with a consequent increase of the turbulent wetted area over the suction side, which will lead to higher losses when compared to the steady case.

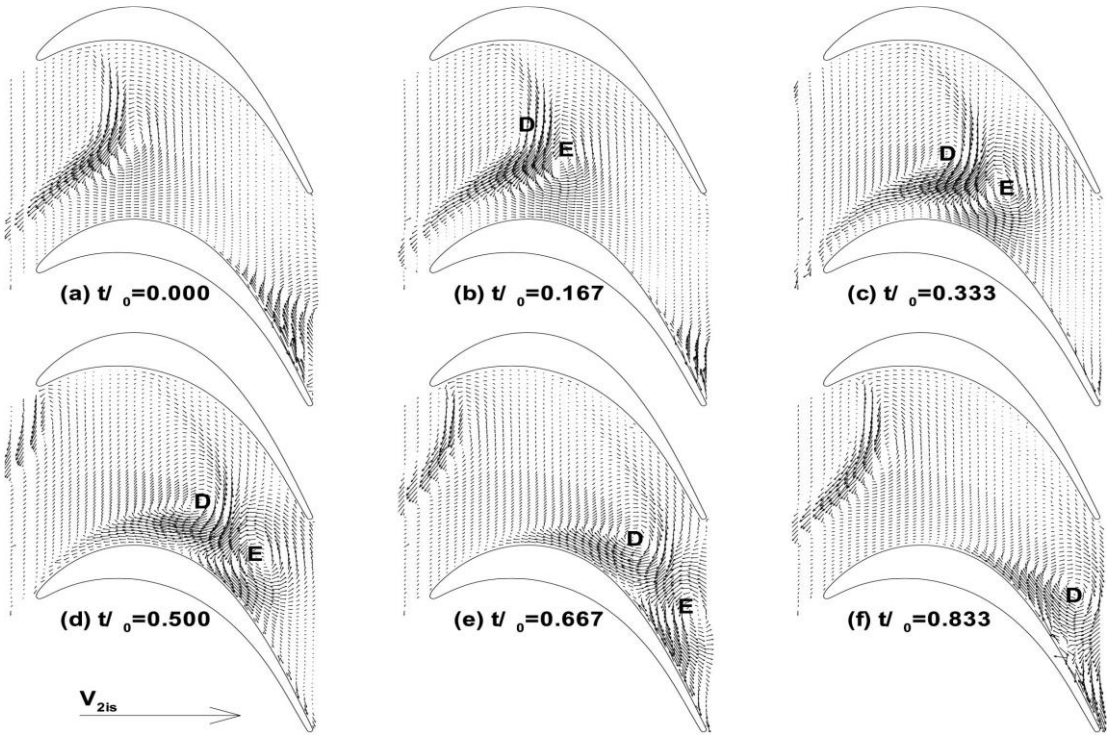

Fig. 2.11 Wake advection into an LPT cascade [44]

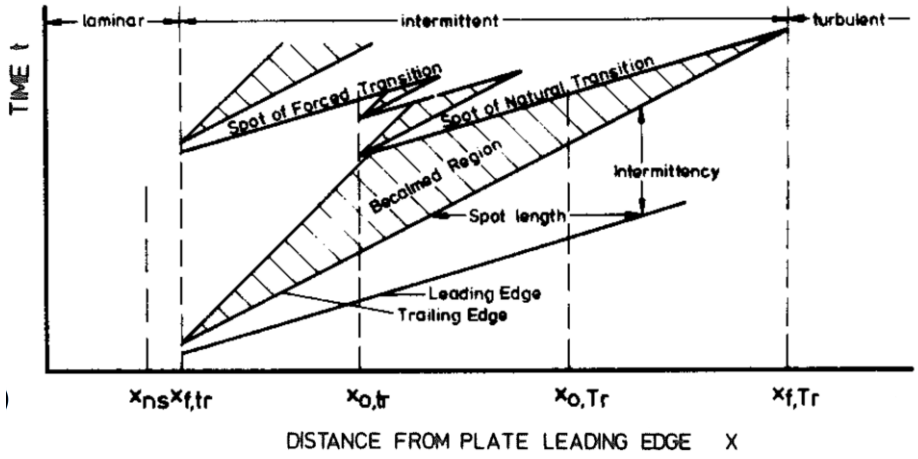

Fig. 2.12 Spatio-temporal evolution of the turbulent spots [46]

In modern LPT cascades, incoming wakes can be used as a flow control strategy, aiming to prevent laminar separation and the development of separated bubble over both blades and vanes, especially in the rear part of the suction side. Indeed, since the inherently cross-pressure gradient characteristic of LPT cascades can induce separated bubble, wakes shed from the upstream cascade are used in order to stabilize the boundary layer, and hence suppress the bubble and related effects. A better explanation of this situation is shown in Fig. 2.13, taken from [47], where the authors provided a spatio-temporal diagram of the wall shear stress over the vane suction surface for three bar passing periods, aiming to provide the wake intensity effect on the separated bubble. Four cases are shown in the figure: the first case shown in Fig. 2.13(a) identifies the steady flow condition, while the other cases refer to the unsteady inflow conditions. Specifically, Fig. 2.13(b) identifies a counterclockwise rotating bars case characterized by the lowest wake turbulence intensity value, Fig. 2.13(c) the non-rotating bar case characterized by intermediate wake turbulence intensity value and Fig. 2.13(d) the clockwise rotating bars case which has provided wakes with the higher turbulent content. The white spots in the plots denote region of wall shear stress values below zero, indicative of a flow separation. The steady inflow condition shows a bubble over the rear part of the suction from $s/S = 0.75$. As the wake turbulence increases, qualitatively the flow separation is less intense, hence the bubble-generated losses are lower. Indeed, turbulence carried by incoming wakes penetrates inside the shear layer leading to flow oscillations within it. These oscillations are amplified over the time and they grow until reaching their maximum at a point where the shear layer rollup occurs, with a consequent creation of Kelvin-Helmholtz vortices. These vortices evolve in space and time with a consequent breakdown along the inflection line of the separated shear layer, as shown in [48-49]. This leads to the formation of turbulent spots and a consequent wake-induced bubble reattachment and hence, reduced bubble generated losses. Fig. 2.13 (b) and (c) show that the wake turbulent content is not able to completely suppress the bubble, while Fig. 2.13(d) shows a configuration where the bubble is completely suppressed, and therefore the boundary layer is entirely turbulent in the rear part of the suction side. A further increase of the wake turbulent content would increase the vane portion affected by a turbulent boundary layer, as shown in the previous paragraphs. Therefore, there is an optimal wake turbulence content value which minimizes both bubble and turbulent losses. According to [44], wake-

induced transition should occur just before or very soon after the separation point onset location in order to reduce losses. Usually in turbomachinery applications, since the wakes shed from the upstream rows periodically impinge the downstream one, it is common to define a wake passing frequency which determines the number of wakes simultaneous present in the cascade. This frequency is defined through the reduced frequency parameter as:

$$f^+ = \frac{f_{bar}\, C_x}{c_x} = \frac{f_{bar}}{f_c} \tag{2.26}$$

Where f_c is associated with the fluid convection time within the cascade, C_x is the axial chord, c_x the axial flow velocity and f_{bar} is the wake shedding frequency.

It is obvious from the previous considerations that if the reduced frequency value is too high, the wake-boundary layer interaction allows a complete bubble suppression between the wake-affected events with a consequent reduction of the bubble-generated losses, but at the same time the turbulent boundary layer will cover a large portion of the blade surface leading to high turbulent loss. For lower values instead, the bubble is suppressed temporarily during a small fraction of time, leading to high bubble-generated losses. Obviously, the optimal value depends directly on the bubble extension present in the steady case. However, it should be reminded that the wakes shedding frequency is determined mainly for aerodynamic reasons which define the pitch-to-chord ratio value as a function of the upstream row aerodynamic loading.

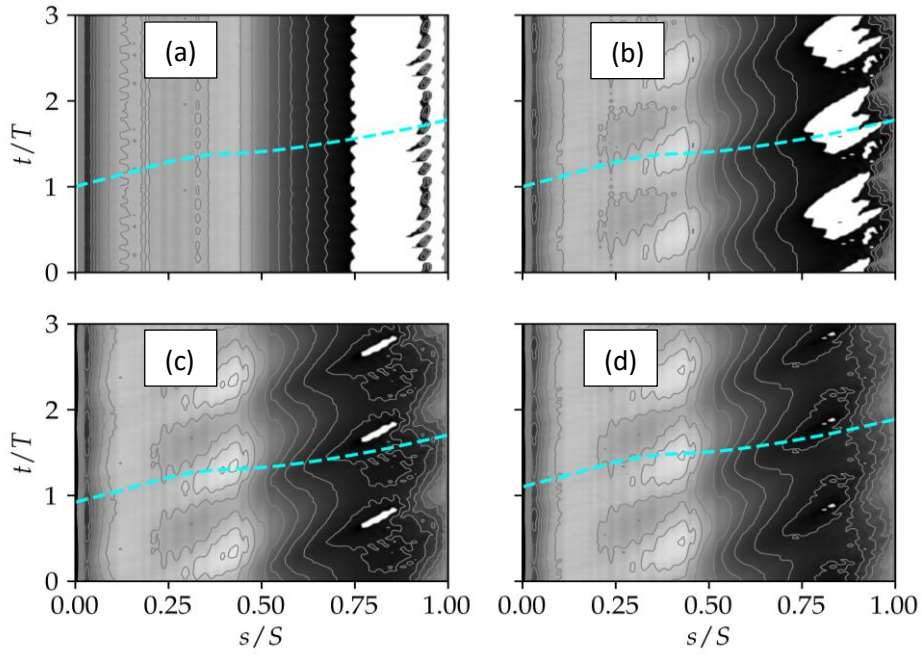

Fig. 2.13 Space-time diagram of the suction side wall shear stress along the streamwise direction for three bar passing periods under (a) steady flow conditions, unsteady flow (b) with counter-clockwise rotating bars, (c) non-rotating bar setup and (d) clockwise rotating bars. [47]

When analyzing the wake effect, an important aspect which also plays a key role on the cascade efficiency is it mixing prior to enter the downstream cascade. It succeeds through either the mixing between wakes of adjacent blades or between incoming wakes and freestream. Michelassi et al. [50] demonstrated by means of large eddy simulations (LES) on a linear LPT cascade that the wake mixing before the leading edge determined how distinct the wakes are upstream the blade leading edge plane. Specifically, more distinct wakes caused a more unsteady boundary layer, and hence leads to higher turbulent losses, whereas mixed out wakes resulted in higher losses related to the freestream turbulence advection within the cascade. Recently, Pichler et al. [51] conducted LES simulations on a linear turbine stage with two different axial gap values between upstream and downstream rows. They led to the conclusion that the smaller gap case provides stronger wakes, and therefore could be useful in preventing flow separation.

From these considerations, it is evident that the wakes shedding phenomenon has an important role in the design process of LPT cascades. Therefore, a deeper understanding of this mechanism is of paramount of importance aiming to improve the operational cost and the efficiency of the whole engine. In the present work, the fundamental parameters of the upstream bar system have been changed and their effect on losses has been quantified. Specifically, the variation of both bar diameter and bar count has allowed to simulate the wakes shed from the upstream rotor in terms of momentum defect and turbulence while the axial gap variation has allowed to modify the degree of wake mixing before the leading edge plane. Results will show good agreement with the literature confirming the potentiality of the experimental technique in capturing the flow physics within LPT cascades as well as quantifying accuracy loss values.

Although this phenomenon represents the major source of unsteadiness within a turbine and affects majorly the boundary layer transition, it cannot be analyzed alone. Therefore, a complete investigation either experimental or numerical must considered the other physical mechanisms and parameters which affect the transition phenomenon, as shown by Mayle [24] and confirmed over the years in [3], [32] and [52]. They all stated that Re, FSTI and the pressure gradient have a preponderant effect on the boundary layer evolution, especially when combined with the unsteady operation of the LPT cascade.

2.1.4 Parameter effect

a) Flow Reynolds number

It is well known that the flow Reynolds number affects the boundary layer evolution. Increasing this parameter leads to higher inertial forces with respect to the viscous ones, with a consequent reduction of the boundary layer thickness δ_{99}. As shown earlier for the Blasius solution, at a given position x along a flat plate, the boundary layer thickness decreases as a function of $Re_x^{\frac{1}{2}}$ in the case of laminar boundary layer and as $Re_x^{\frac{1}{5}}$ in the case of turbulent one. As Re_x increases, both displacement thickness and momentum thickness decrease at a fixed position on the flat plate, reducing the blockage effect and the viscous losses.

Concerning the effects of Reynolds number on the transition process, when the local Reynolds number (Re_x) reaches a threshold value, transition occurs. This value strongly depends on the geometry under consideration (e.g. flat plate, pipe). Even though Re_x is generally adopted to indicate the position corresponding to the transition onset, it is usual to use another dimensionless parameter, namely the momentum thickness Reynolds number, defined as follows:

$$Re_\theta = \frac{U_e \theta}{\nu} \tag{2.27}$$

In literature, Re_θ is usually used in order to develop empirical correlations able to predict the transition process in terms of transition onset and length. In fact, the momentum thickness at a given position is a function of the pressure gradient imposed to the flow and the boundary layer state up to that position. Hence, in case of separated flows for example, its quantification at the separation position takes into account the boundary layer evolution from the leading edge up to that position, differently from the local Reynolds number simply based on the streamwise position considered. In this specific case of separated flows, Mayle [24] proposed a correlation which provides the Reynolds number based on the distance between separation and transition onset $(Re_x)_{st}$ as a function of the momentum thickness Reynolds number at separation $(Re_{\theta,s})$

$$(Re_x)_{st} = 300 Re_{\theta,s}^{0.7} \quad \text{for short bubble} \tag{2.28}$$

$$(Re_x)_{st} = 1000 Re_{\theta,s}^{0.7} \quad \text{for long bubble} \tag{2.29}$$

Although the correlations proposed by Mayle for the prediction of the transition onset are different for short and long bubbles, the correlation proposed for the prediction of the transition length Reynolds number (Re_L) is the same for both the bubble configurations:

$$Re_L = 400 Re_{\theta,s}^{0.7} \tag{2.30}$$

Several other works carried out in the past have focused on the effects of the flow Reynolds number on the transition process development in case of both attached and separated flows. Volino [53-54] analyzed the effects of the Reynolds number on the development of laminar separation bubble over turbine blade profiles, showing that as Re increases the bubble dimension is shorter. Since the reattachment is induced by the BL transition, it follows that higher Re shifts upstream the location of transition. This consideration is also valid for attached flows, i.e., the transition onset moves upstream as the flow Reynolds number increases [55]. These findings have been also confirmed in LPT cascades where usually in addition to Re effect on transition, the authors provide the Reynolds lapse rate (see [6], [14] and [52] for example). All these studies usually vary Re in a range covering cruise and take-off conditions of typical engines, leading to the same conclusion: as Re decreases losses increase due to a major boundary layer thickening. Specifically, the boundary layer thickening induces both higher viscous effects on the vane sides and major blockage effects at the trailing edge plane. A further decrease in Re can provoke the appearance of a separated bubble, which is an additional source of losses as largely discussed in the previous paragraphs. However, upstream rows are designed in order to control this flow separation and reduced the losses associated.

b) Flow background turbulence

As previously mentioned, the freestream turbulence intensity is known to strongly affects the transition process. For low values of this parameter, the disturbances inherently present within the boundary layer are amplified in the form of 2D Tollmien-Schlichting waves. For high values (FSTI > 0.5−1%) instead, this mechanism is by-passed and transition due to streamwise streaks is observed. Freestream turbulence is responsible for the penetration of velocity fluctuations inside the boundary layer and, on the other hand, can promote the breakdown of the structures that have been amplified inside the boundary layer by means of different interaction mechanisms between the BL and the freestream region (see e.g., Jacob and Durbin [26]). Whatever the transition process is (natural, by-pass or separation induced), increasing the freestream turbulence is reflected in a higher value of the initial disturbances that will be amplified by the BL and the transition occurs more upstream.

Turbulence appears to be the most important parameter for bypass transition correlations, as shown in the work proposed by Hall and Gibbins [56] for the prediction of the transition beginning:

$$Re_{\theta s} = 163 + exp(6.91 - Tu) \tag{2.31}$$

Where $Re_{\theta s}$ is the momentum thickness Reynolds number at transition onset. Note that the higher turbulence level the lower is $Re_{\theta s}$ at transition, thus the transition onset location moves upstream. The momentum thickness Reynolds number at the end of transition ($Re_{\theta E}$) is instead related to $Re_{\theta s}$ according to:

$$Re_{\theta E} = 2.667\, Re_{\theta s} \tag{2.32}$$

which is valid for low FSTI level up to the high values typical of turbomachinery applications.

In the case of by-pass transition, Mayle proposed the following correlation for the momentum thickness Reynolds number at the transition onset:

$$Re_{\theta s} = 400\, Tu^{-\frac{5}{8}} \tag{2.33}$$

Where $Re_{\theta s}$ is again expressed as a function only of the freestream turbulence. However, to have a more reliable prediction of the transition onset, the effects of pressure gradient should be also considered (see Abu-Ghannam and Shaw [57]).

For natural and bypass transition cases with zero pressure gradient, Mayle [24] developed a simplified correlation for the spot production parameter $\hat{n}\sigma$ as a function of freestream turbulence intensity:

$$\hat{n}\sigma = 15 * 10^{-12} Tu^{\frac{7}{4}} \tag{2.34}$$

Here $\hat{n} = nv^2/U_e^3$ is the dimensionless spot production parameter, while σ is the Emmon's constant equal to 0.27. The spot production parameter $\hat{n}\sigma$ is fundamental in the transition analysis since it is directly linked to the transition length. Indeed, a function called intermittency can be defined being representative of the fraction of time during which the flow over any point P on a surface is turbulent. According to the original formulation of Emmons the intermittency function is defined as:

$$\gamma(P) = 1 - \exp[-\iiint g(P_0)\, dx_0 dz_0 dt_0] \tag{2.35}$$

where $g(P_0)$ is the production term of turbulent spots, while their propagation and growth in time are accounted for by means of the integrals over the (x, z, t) domain. When γ = 0 the flow is laminar, while when γ = 1 is turbulent. Successively, Dhawan and Narasimha [58] wrote the production term $g(P_0)$ appearing in the Emmons' equation as a function of the turbulent spot production rate n defined for unit distance in the spanwise direction z, obtaining the following formulation for the intermittency function:

$$\gamma(x) = 1 - \exp[-\frac{n\sigma}{U_e}\,(x - x_t)^2] \qquad (x \geq x_t) \tag{2.36}$$

where x_t is the transition onset location. Introducing the local Reynolds number $Re_x = Ux/\nu$, the previous equation can be rewritten as:

$$\gamma(x) = 1 - \exp[-\hat{n}\sigma\,(Re_x - Re_{xt})^2] \qquad (x \geq x_t) \tag{2.37}$$

where $\hat{n}$ is the dimensionless spot production parameter appearing in eq. 2.34. It is clear that, if the spot production parameter $\hat{n}\sigma$ increases, the gradient of the intermittency function γ becomes higher. Comparing now eqs. 2.34 and 2.37 it follows that the turbulence intensity acts reducing the transition length. Later, Suzen et al. [59] implemented a new correlation starting from the one proposed by Mayle, which is valid also in case of non-zero pressure gradient:

$$\hat{n}\sigma = F(K)\hat{n}\sigma_{zpg} \tag{2.38}$$

$$F(K) = 10^{-3227K^{0.5985}} \qquad (K > 0) \tag{2.39}$$

$$F(K) = (120 - 100Tu^{-0.5} + 850Tu^{-3})^{[1-\exp(0.75*10^6 KTu^{-0.7})]} \qquad (K < 0) \tag{2.40}$$

Where $\hat{n}\sigma_{zpg}$ refers to the spot production rate in case of zero pressure gradient and *F(K)* is a function of both turbulence and *K*, with this latter representing the acceleration parameter defined by

$$K = \frac{\nu}{U_e^2}\frac{dU_e}{dx} = \frac{\lambda_\theta}{Re_\theta^2} \tag{2.41}$$

To keep into account for the effects of turbulence intensity in case of separated flows, Suzen [59] proposed the following correlation for the transition onset:

$$(Re_x)_{st} = 874\, Re_{\theta,s}^{0.71} \exp(-0.4Tu) \tag{2.42}$$

From which it is evident that the length necessary for transition, proportional to the transition onset Reynolds number $(Re_x)_{st}$, reduces when increasing the freestream turbulence intensity.

Concerning the LPT efficiency, the effects of FSTI on LPT losses have been largely investigated in literature, mainly in combination with other design parameters like the flow Reynolds number and the rotor incoming wakes (See [52] for example). Summarizing, at low Reynolds numbers and especially in the presence of separated bubbles, high FSTI values induce lower losses as a consequence of the positive effect of the background turbulence on laminar separation bubbles. Moreover, the combination of periodically unsteady inflow conditions with high freestream turbulence can further reduce LPT losses, depending on the bubble extension. In the no separation case instead, the anticipated transition induced by freestream turbulence affects the loss production within the cascade through the extension of the region affected by a turbulent boundary layer. Therefore, FSTI effect needs to be quantified through its counteraction on both turbulent and bubble-generated losses.

c) Pressure gradient

The presence of an adverse pressure gradient is well known to strongly affect the flow development, inducing a further boundary layer thickening. In the case of turbine blades or flat plate profiles with an imposed pressure variation, this boundary layer thickening generates a remarkable increasing in momentum loss. Different correlations have been proposed aiming to predict the transition onset in case of non-zero pressure gradient for both natural and by-pass transitions. The most famous one is the correlation proposed by Abu-Ghannam and Shaw [57], which considers the streamwise pressure gradient through the dimensionless parameter λ_θ already introduced in eq. 2.41. When natural transition occurs, λ_θ is expected to play an essential role in the transition process, and the critical momentum thickness Reynolds number for which transition starts can be computed by means of the following equation derived by Abu-Ghannam and Shaw [57]:

$$Re_{\theta S} = 163 + \exp(F(\lambda_\theta) - \frac{F(\lambda_\theta)}{6.91}Tu) \tag{2.43}$$

where

$F(\lambda_\theta) = 6.91 + 12.75\lambda_\theta + 63.64{\lambda_\theta}^2$ if $\lambda_\theta < 0$ and $F(\lambda_\theta) = 6.91 + 2.48\lambda_\theta - 12.27{\lambda_\theta}^2$ if $\lambda_\theta > 0$.

Results from Eq. 2.43 are plotted in Fig. 2.14. It should be noticed that, for a given level of turbulence, the influence of the adverse pressure gradient in promoting transition is greater than the capability of a favorable pressure gradient in delaying it. Moreover, the effect of the pressure gradient is diminished as the turbulence level increases.

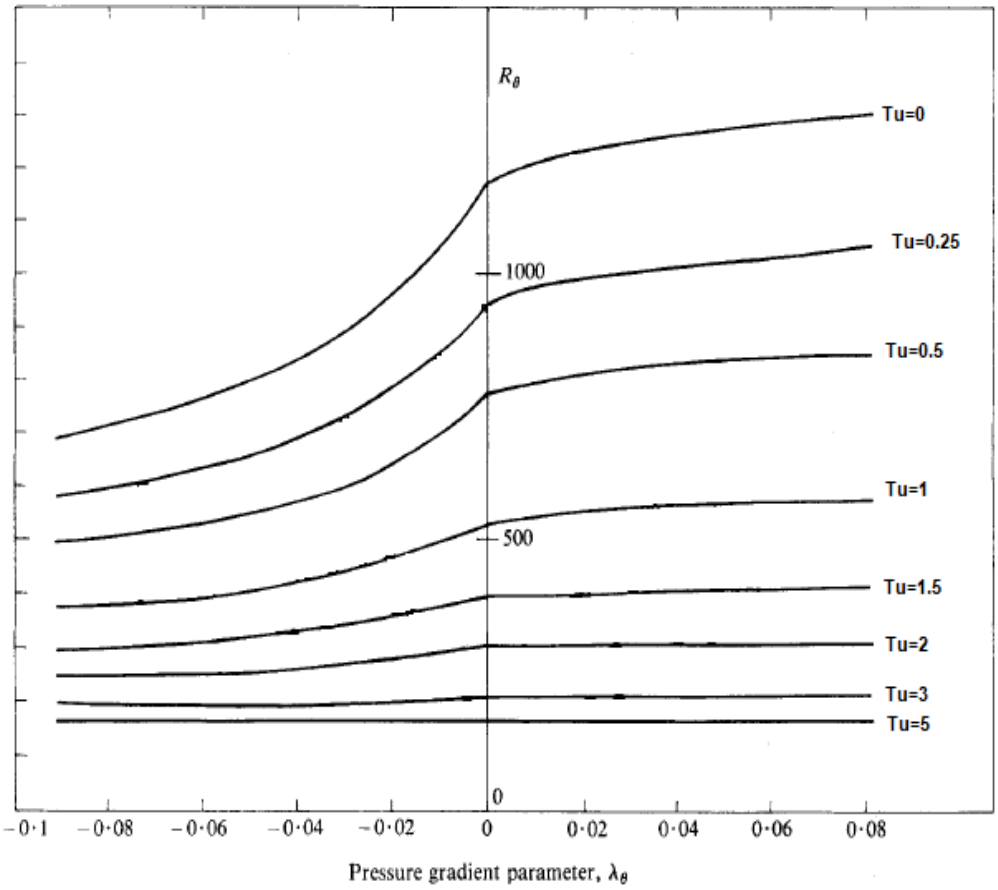

Fig. 2.14 Momentum thickness Reynolds number computed at the transition onset for different values of λ_θ and freestream turbulence [57].

Abu-Ghannam and Shaw [57] also proposed a correlation for the momentum thickness Reynolds number at the end of transition $Re_{\theta E}$ which is valid for both adverse and favorable pressure gradient:

$$Re_{\theta E} = 540 + 183.5(Re_L 10^5 - 1.5)(1 - 1.4\lambda_\theta) \tag{2.44}$$

Note that in this formulation the Reynolds number based on the transition length (Re_L) is considered. It was first defined by Dhawan and Narashima [58] based on a length L_γ, over which the intermittency (defined in equation 2.37 increases from 0.25 to 0.75; furthermore, Dunham [60] demonstrated that the total length of transition L is proportional to L_γ as $L = 3.36L_\gamma$. Once L is known the Reynolds number Re_L can be calculated, thus $Re_{\theta E}$. If the adverse pressure gradient imposed to the flow is sufficiently high, the boundary layer separates. In this context, the reference criterion for the estimation of the laminar separation position expressed in terms of the momentum thickness Reynolds number at separation is the criterion of Thwaites [61]:

$$Re_{\theta,s}^2 K \leq -0.082 \tag{2.45}$$

where *K* is the acceleration parameter defined previously in eq. 2.41. Note that eq. 2.45 implies that the momentum thickness Reynolds number at separation is automatically fixed if the distribution of *K*, i.e. the pressure gradient imposed to the flow, is known. The case of turbulent boundary layer separation was investigated with a similar approach by Buri, who proposed the following correlation for the momentum thickness Reynolds number at separation:

$$Re_{\theta,s}^{5/4} K \leq -0.005 \tag{2.46}$$

A comparison between the two equations clearly shows that turbulent boundary layer resists more to the separation due to the fact that it is able to sustains higher adverse pressure gradients, as highlighted by the different exponent of $Re_{\theta,s}$. In the case of laminar separation, the correlation that is widely adopted for the prediction of the transition onset Reynolds number is the one proposed by Suzen et al. [59] defined in eq. 2.47and reported here:

$$(Re_x)_{st} = 874\, Re_{\theta,s}^{0.71} \exp(-0.4Tu) \tag{2.47}$$

Note that, once $Re_{\theta,s}$ is computed as a function of the pressure gradient imposed to the flow by means of eq. 2.45, then $(Re_x)_{st}$ can be obtained.

Pressure gradient effect on loss generation within LPT cascades has been largely discussed in literature (see [6] and [32] for instance) since it is related to the cascade solidity, which is one of the critical parameters during the preliminary design phase. The modern tendency in LPT design in reducing the whole engine weight has diffused the use of LPT cascades characterized by low solidity values, and hence high values of cross-passage pressure gradient. This solution can provide a poor guidance to the working fluid with a consequent decrease in LPT performance. Moreover, these cascades present high adverse pressure gradient values in the rear part of the suction side, making them more subject to flow separation with related losses.

2.2 Loss correlations in physical space

The previous effects discussed by means of previous literature works, are usually synthetized through empirical correlations able to predict the loss behavior of LPT cascade operating under a variable range of the most influencing parameters.

At the preliminary design stage, the most efficient method of estimating losses of a new LPT is the adaptation of available empirical data. To this end, several correlations based on large dataset are available in the literature. In this paragraph, an example of one of the most adopted correlation is presented.

a) Ainley and Mathieson

One of the best known and complete studies of turbine performance prediction was carried out by Ainley and Mathieson [62] They presented a method based on a mean-line analysis aiming to estimate the performance of axial-flow turbines. Using experimental data on blades with maximum thickness-to-chord ratio values between 0.15 and 0.25, they provided the plots shown in Fig. 2.15 for the evaluation of profile losses for both nozzle and impulse blades.

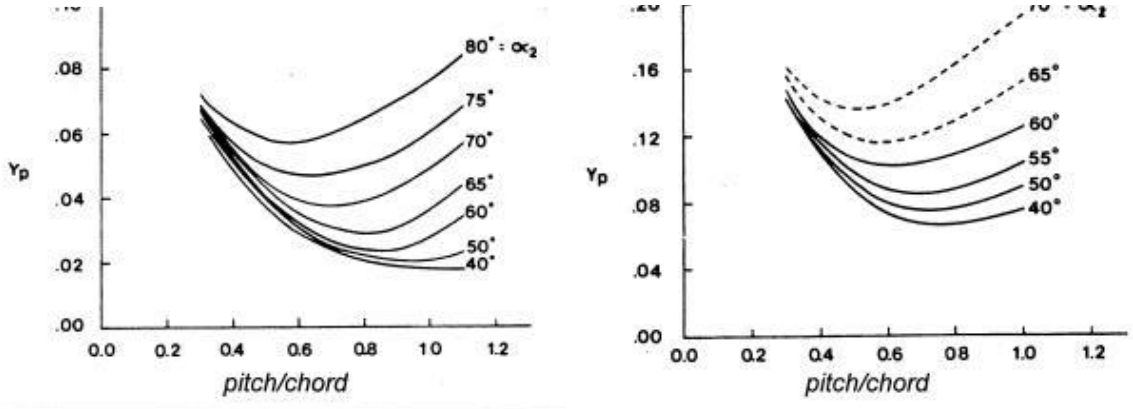

Fig. 2.15 Profile loss coefficient for (a) nozzle blades $\alpha_{in} = 0$ and (b) impulse blades $\alpha_{in} = \alpha_{out}$ [62]

For blades with different inflow and outflow angles, they provided the following expression:

$$Y_{p\,(i=0)} = \left\{ Y_{p\,(\alpha_{in}=0)} + \left(\frac{\alpha_{in}}{\alpha_{out}}\right)^2 \left[Y_{p\,(\alpha_{in}=0)} - Y_{p\,(\alpha_{in}=\alpha_{out})} \right] \right\} \left(\frac{t_{max}/c}{0.2}\right)^{\frac{\alpha_{in}}{\alpha_{out}}} \tag{2.48}$$

Where

- α_{in} and α_{out} are the inlet and outlet flow angles respectively
- t_{max}/c is the maximum thickness-to-chord ratio

Furthermore, Ainley and Mathieson provided a correction term aiming to evaluate the off-design performance through a stall incidence angle defined as the incidence at which the profile loss is twice the minimum profile loss, and it is a function of the pitch-to-chord ratio and the flow angles. Nevertheless, parameters like blade curvature, flow Mach number, surface roughness, compressibility, and heat transfer were not considered.

b) Ainley improvements

Over the years, researchers used the correlation of Ainley and Mathieson and tried to improve it by adding new features and correction terms. For instance, Craig & Cox [63] introduced correction terms for the profile loss as a function of the flow Reynolds number, the lift coefficient and the contraction ratio. These two last terms are both functions of flow angles and pitch-to-chord ratio. Then, they summarized their loss expression via carpet plots shown in Fig. 2.16. At that time, their method worked very well on either axial gas or steam turbines. Similar works have been provided over the years: Dunham & Came [64] provided another correlation accounting for the flow Reynolds number as correction term while Kacker & Okapuu [65] introduced the effect of compressibility and shock waves into their loss evaluation.

All these methods were based on experimental data acquired on old blade designs and were also unable to understand the flow physics at the origin of losses. Improvement of measuring techniques and advent of sophisticated instruments overcome this issue, and this has provided in-depth investigations of the flow physics and the main parameters affecting the loss generation. Therefore, a different philosophy in providing loss correlations has emerged, based on boundary layer theory and simplified equations of the conservation of mass, momentum and energy. Among all the correlations using these principles that can be found in literature, the best known is the Denton one [15]. He led to the conclusion that viscous effects in both boundary layer and mixing processes, shock waves and heat transfer, caused an entropy generation within the turbine. Then, focusing on the flow mixing out behind the trailing edge of the blades and implementing a control volume approach, he provided a relationship between the blade loss coefficient and the boundary layer parameters according to eq. 2.49

$$Y_P = \frac{C_{pb}}{s\cos\alpha_1} + \frac{2\theta}{s\cos\alpha_1} + \left(\frac{t+\delta^*}{s\cos\alpha_1}\right)^2 \tag{2.49}$$

Where the first term is the loss caused by the base pressure acting on the trailing edge. The second term represents the loss generated by the boundary layer evolution within the cascade and it includes loss mixing downstream of the trailing edge; it accounts typically around 90% of the total. The third term arises from the combined blockage of the trailing edge and the boundary layers.

More recently, Coull and Hodson [66] modified the Denton's formulation in order to provide a new empirical correlation to evaluate losses. Their correlation was based on experimental investigations on a flat plate by means of laser Doppler anemometry (LDA) varying the shape of the suction surface velocity distribution. Afterwards in [67], they reviewed the well-established prediction methods and provided a comparison with their own correlation on a repeating LPT stage. They concluded that Ainley, Dunham and Kacker models vary widely in their prediction in the large design space under their observation and they did not capture

the correct trend across the Smith chart. According to the authors, this is probably due to the absence of a term related to the shape of the blade surface pressure distributions in the correlations, since as shown in [13], it can be a source of non-negligible losses. The absence of unsteady incoming wake related effects on loss generation could be another possible source of inaccuracy of these correlations.

In the present work, overall losses of LPT cascades have been evaluated by means of the procedure described in chapter 4. The effects on losses of design parameters like the freestream turbulence intensity, the flow Reynolds number, the incidence flow angle, the vane solidity and the incoming wake parameters have been evaluated. Moreover, a procedure useful in reducing the number of tests within a given design space has been developed and it will be shown its efficiency in providing the same observations made during the experimental campaign: similar flow physics (freestream losses in the potential flow region, both magnitude and position of the vane wake peak, wake-boundary layer interaction) and loss trend within the whole design space. Therefore, this procedure provides guidelines for future investigations on LPT cascades especially when a large variety of design parameters need to be tested. This could be useful in formulating new empirical loss correlations as well as improving the accuracy of the currently available ones.

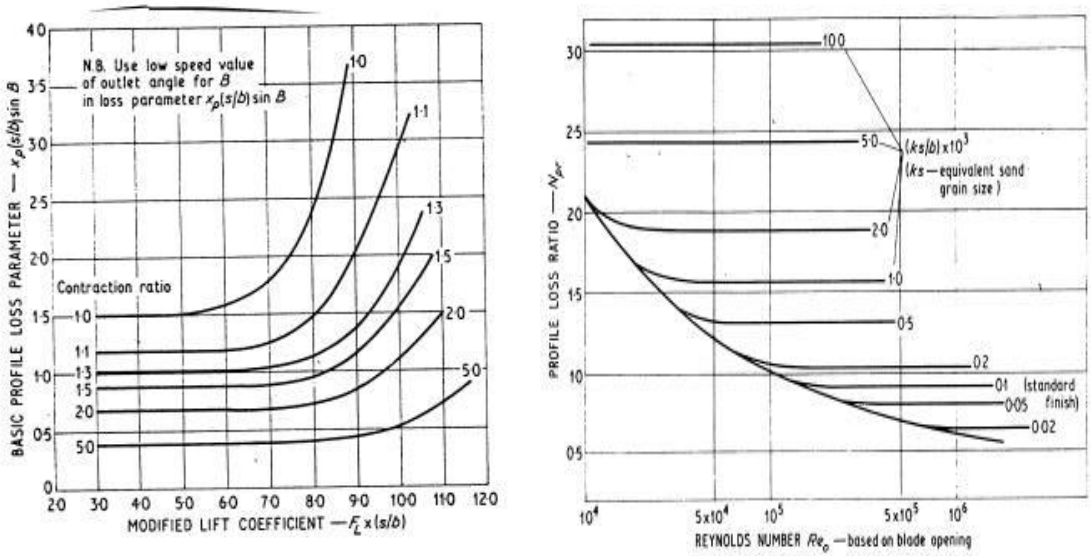

Fig. 2.16 Craig and Cox plots for profile losses evaluation [63]

.

Chapter 3 Experimental facility

The experimental investigations of the present work have been performed on three different LPT cascades installed into the wind tunnel available at the Aerodynamics and Turbomachinery Laboratory of the University of Genoa, shown in Fig.3.1.

Investigations were carried out under realistic flow environment varying the unsteady inflow conditions, the Zweifel number, the flow Reynolds number and the incidence flow angle in order to obtain an overview of LPT performance in a wide range of operating conditions. In the subsequent sections, an in-depth description of the experimental facility is provided.

Fig. 3.1 Wind tunnel installed at the laboratory of Aerodynamics and Turbomachinery of the University of Genova

3.1 Wind tunnel

The wind tunnel sketched in Fig.3.2 is a classical open low-speed facility specifically designed to perform detailed measurements on LPT cascades. Its intake section is provided with a filter aiming to avoid air impurities which can damage the measuring equipment. Air is drawn in from the laboratory by means of a centrifugal fan driven by a *200 kW* AC motor. Control of air speed is achieved by means of an inverter which acts directly on the fan rotational speed. Note that the fan has been designed in order to satisfy the right amount in terms of flow rate and air pressure at each operative condition tested.

Once sucked, air is diffused into a duct prior to enter in the settling chamber. The duct is *2594 mm* long, *7.5°* opening angle and *1:6* area ratio. These parameters have been chosen during the design phase using the Sovran and Klompf maps in order to avoid flow separation on the diffuser walls. Moreover, within the diffuser duct, there is a screen which helps to reduce the flow background turbulence and the dimension of large-scale structures. Hence, quasi laminar flow can pass through the *1412 mm* settling chamber where honeycombs and screens reduce further the remaining turbulence activity. Screens are rectangular metallic grids which break-up the large-scale vortical structures making the flow velocity profile more uniform. These grids have the drawback to deviate the flow from its designed path. This effect is completely compensated by using metallic honeycombs which are a set of cells of *10x50 mm*^{2} helpful in eliminating any wall-normal velocity component. Downstream of the settling chamber, a *1000 mm* convergent duct of about *10:1* area ratio is installed. The convergent duct imposes a strong acceleration to the flow reducing the boundary layer thickness on its walls. At its outlet section, the flow is uniform and aligned with the tunnel principal axis, with a boundary layer thickness negligible and a very low level of FSTI (about 0.19%). The flow in these conditions is then discharged into the test section where measurements have been carried out.

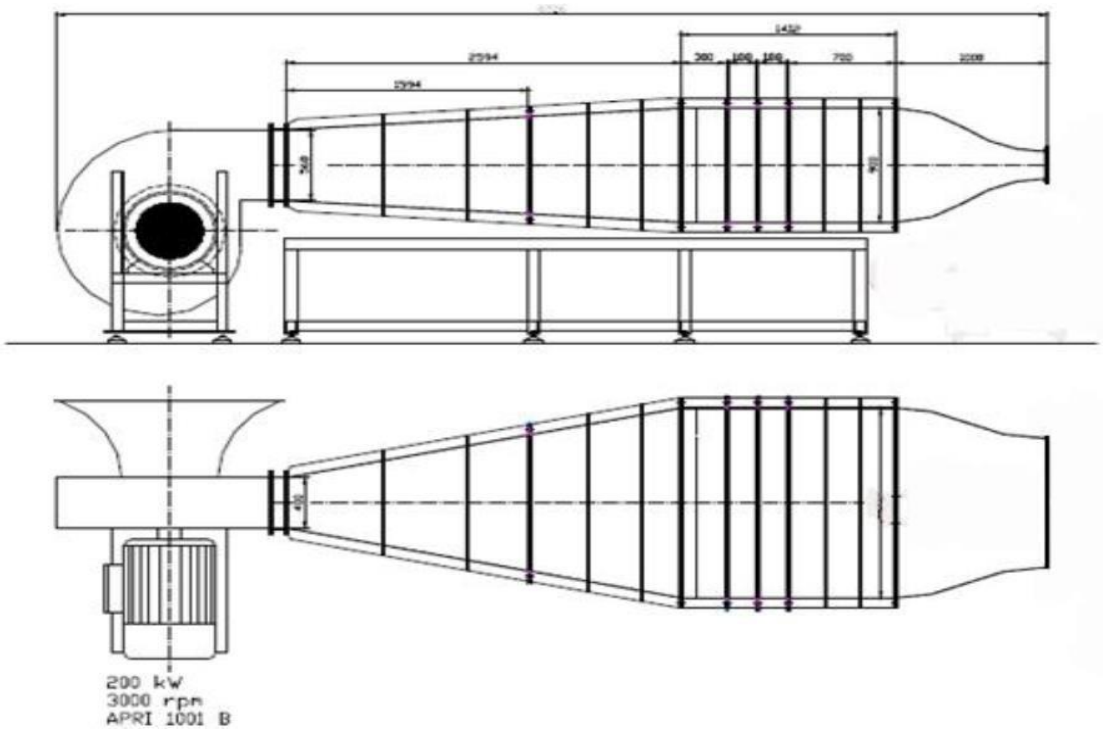

Fig. 3.2 Top and side views of the wind tunnel used in the present work for investigations

3.2 Test section

The test section is located downstream of the convergent duct and it is equipped with a series of slots, gaps and holes helpful in performing detailed measurements on LPT cascades under

real engine operative conditions. It is shown in Fig. 3.3 where the reader can see a cascade installed within it as well as the bleeds and tailboards, whose goal will be presented further.

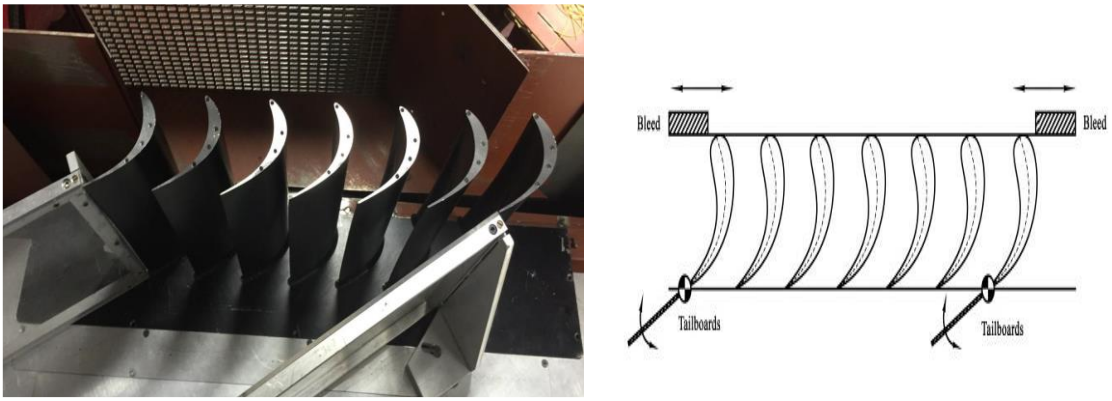

Fig. 3.3 Picture (left) and sketch (right) of a cascade installed within the test section with the relative bleeds and tailboards

The test section lower part is made of aluminum and it presents a slot for the moving bar system for incoming wake simulation (which will be discussed later). At about *30 mm* from the trailing edge plane, a series of pressure taps are present, and they provide the static pressure distribution downstream of the cascades, useful to compute the loss coefficient.

The upper part is instead made of plexiglass in order to guarantee a visual inspection during the tests and to provide an optical access for both PIV and LDV measurements. Moreover, the plexiglass presents two tangential slots aiming to allow the movement of the pneumatic probes and hot-wire anemometer used in the present investigations; the first slot is placed at an axial distance of 60 mm from the trailing edge plane location while the second is between the bars and the vanes leading edge plane. Once installed in theses slots, probes can be moved by means of a two-axis traversing system driven by a stepper motor which in turn is controlled through a NI controller linked to a PC computer. This system guaranties the probe translation in both pitchwise and spanwise directions, with minimum steps of $8\ \mu m$.

Moreover, since the tests were carried out on linear cascades with a finite number of vanes (7), in order to restore the flow periodicity, condition inherently present in real engines, on the sides of the external vanes bleeds and tailboards are placed and can be adjustable as shown in the right plot of Fig. 3.3. Both have the purpose to simulate the potential effects of the adjacent vanes. The bleeds are placed laterally to the leading edge and act on the flow incidence angle while the tailboards are plexiglass walls fixed at the trailing edges of the cascade external vanes with a prevalent effect on the exit flow angle.

Finally, experimental surveys have been carried out in order to provide LPT performance under realistic operation, covering on and off-design conditions. Specifically, the wind tunnel used in the present work allows us to perform tests:

- **at fixed value of FSTI**: useful to reproduce the flow background turbulence at the cascade inlet, typically around 4-5% in real engines; it has been obtained by means of a turbulence generating grid.

- **flow Reynolds number** within the range 70000 < Re <350000 in order to evaluate the cascade performances in a range covering typical cruise and take-off conditions
- **under periodic unsteady inflow conditions:** useful to reproduce the wakes advection within the cascade. This has been done through a moving bar system for the generation of upstream wakes.
- **flow incidence angle** within the range -9 ° < i <+ 9 °, in order to evaluate the cascade performances also in off-design conditions. This has been done by a system which allows the test section rotation with respect to the rest of the wind tunnel.

A detailed description of the systems used to set all these quantities is provided in the following.

a) Turbulence grid

The grid for turbulence generation useful to reproduce a realistic flow background turbulence is sketched in Fig. 3.4. It has been constructed by means of laser cut with a consequent milling for refining finishes. Moreover, it is located into a duct of constant area located between the test section and the convergent duct.

During the investigations, there is a need to reproduce the typical values of flow background turbulence at the LPT entrance (about 4- 5%) since as already stated, it has a non-negligible effect on the boundary layer evolution over the vanes, and hence influence the losses.

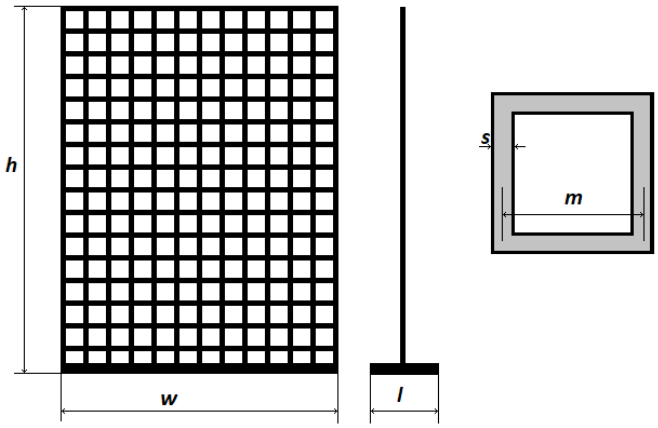

Fig. 3.4 Sketch of the grid for turbulence generation

From the grid geometrical parameters, it is possible to derive an expression for the expected *FSTI* level:

$$FSTI = C\left(\frac{d}{x_{turb}}\right)^{-5/7} \tag{3.1}$$

Where *FSTI* is the freestream turbulence intensity, *C* is a geometric parameter which depends mainly on the grid mesh, *d* is the bar diameter and x_{turb} is the axial distance from the cascade.

Based on eq. 3.1, it has been decided to make a square grid of *5x5 mm²* with cylindrical bars of *5 mm* diameter aiming to obtain the desired FSTI value (about 4%). A similar rectangular grid of *4 mm* bar diameter has been used in order to provide the FSTI effect on LPT losses. This ultimate generates a turbulence value of about 5.2%.

Measurements of turbulence quantities using hot-wire techniques have been performed aiming to evaluate the turbulence decay law within the tunnel and to provide the relationship between the turbulence generated and the flow Reynolds number. Results that will be shown in chapter 6 have permitted to place the grid more than five chord upstream of the blade leading edge. This aims to ensure the same level of turbulence with a tolerance of ± *0.5%* for all the tested conditions. Moreover, the grid has been locked in such a way that excessive vibrations are inhibited prohibiting any significative fluctuation of the turbulence level generated during ongoing investigations.

b) Moving bar system

The wakes shed from upstream rows in turbomachines can be simulated by means of a moving bar system in order to provide useful information on the stator-rotor interaction phenomenon. Indeed, as demonstrated firstly by Pfeil and Eifler [40] the structure of the far wake region of cylindrical bars is representative of blade wakes.

The system consists of a wheel of bars which rotates in a plane parallel to the leading edge one (Fig. 3.5). Usually, the bar diameter is set in order to generate a wake characterized by losses typical of a real upstream LPT row. This has been made possible through eq. 2.24 once fixed the total pressure drop through the bar system, ensuring the correct momentum defect upstream of the testing cascade.

Fig. 3.5 Bar-passing mechanism

Moreover, realistic stator-rotor interactions must consider real operative conditions in terms of flow coefficient and reduced frequency. The flow coefficient defined in eq. 3.2 is useful to reproduce the flow velocity triangle at the cascade inlet where c_x is the axial component of the flow velocity and *u* the bar peripheral velocity, while the reduced frequency defined

in eq. 2.26 ensures to reproduce the correct ratio between convective time scale and wake time scale.

$$\varphi = \frac{c_x}{u} \tag{3.2}$$

From eqs. 2.25, 2.26 and 3.2, it is possible to determine both bar pitch and bar diameter as well as the bar peripheral velocity, once fixed the desired flow coefficient, reduced frequency and momentum defect.

In the present work, the flow coefficient has been kept constant to 0.675, which is a typical value of aeroengine stages. Both bar diameter and bar pitch have been varied in order to change the wake momentum defect and the turbulence intensity associated with the wake shedding phenomenon. Moreover, the axial gap between the bar system and the cascade leading edge plane has been also changed from 33 mm to 52 mm to simulate different axial extension of the whole LPT stage.

Note that the moving bar system, due to its velocity defect, reduces the flow angle at the cascade inlet and hence, this needs to be compensated by a pre-rotation of the test section. The pre-rotation angle value is obtained by applying a control volume approach through the bar system, in the relative frame of reference, as sketched in Fig. 3.6 taken from Simoni et al. [9].

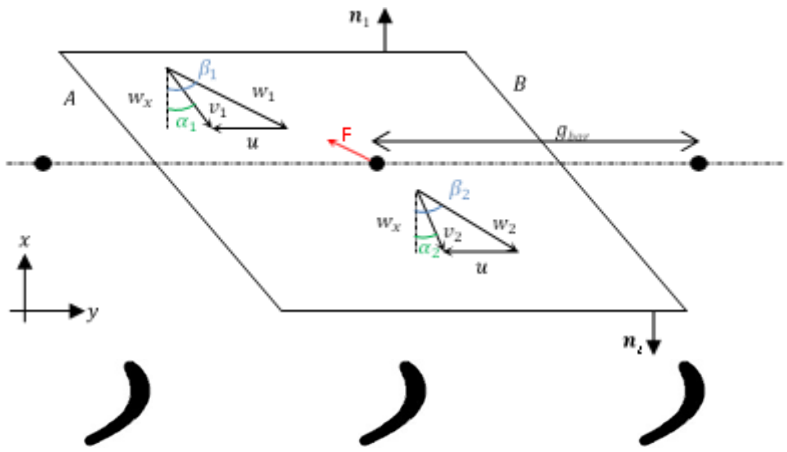

Fig. 3.6 Control volume of the flow through the bar-passing system [9]

Under the assumptions of a 2D, steady and incompressible flow, and considering that on surfaces A and B periodic conditions are applied, it is possible to write the momentum conservation through the bars as:

$$\boldsymbol{F} = \dot{m}(\boldsymbol{w_1} - \boldsymbol{w_2}) + (p_1\boldsymbol{n_1} - p_2\boldsymbol{n_2})g_{bar}b \tag{3.3}$$

Furthermore, the drag force F representing the force produced by the bars on the fluid can be expressed as

$$\boldsymbol{F} \cong \frac{1}{2}\rho \boldsymbol{w_1}^2 C_D b d \tag{3.4}$$

Both components of the drag force can be therefore written as

$$F_x = (p_1 - p_2) g_{bar} b \tag{3.5}$$

$$F_y = \dot{m}(w_{y1} - w_{y2}) = \rho w_x g_{bar} b (w_{y1} - w_{y2}) \tag{3.6}$$

Since in axial turbines $\Delta w_y = \Delta v_y$, F_y can be rewritten as

$$F_y = \rho w_x g_{bar} b (v_{y1} - v_{y2}) = \rho g_{bar} b {w_x}^2 (\tan \alpha_1 - \tan \alpha_2) \tag{3.7}$$

Matching this last equation with the projection of the force F into the tangential direction leads to:

$$\frac{1}{2}\rho {w_1}^2 C_D b d \sin \beta_1 = \rho g_{bar} b {w_x}^2 (\tan \alpha_1 - \tan \alpha_2) \tag{3.8}$$

It is therefore possible to derive a relationship for the absolute flow angle downstream of the bar system

$$\tan \alpha_2 = \tan \alpha_1 - \frac{1}{2} \frac{C_D \, d \tan \beta_1}{g_{bar} \cos \beta_1} \tag{3.9}$$

From eq. 3.9, it has been possible to find out the value of approximately 3° of pre-rotation of the test section to compensate the flow deflection at the cascade inlet introduced by the rotor wakes. More details on the bar cascade and its characterization in the most critical tested conditions can be found in [9].

c) System for variation of the incidence angle

In order to analyze the cascade performance in off-design conditions, the wind tunnel is equipped with a mechanical system which allows the rotation of the test section with respect to the remaining part of the tunnel. This system, shown in Fig. 3.7, is a large bearing with the axis passing through the leading edge of the central vane of the cascade. It allows the test

section rotation up to ± 9 ° with respect to the nominal incidence angle i = 0 °, corresponding to an inlet flow angle of 40 °.

This solution allows the test section and the moving bar system to rotate rigidly, leading to a correct evaluation of loss distribution under steady and unsteady incoming flows while varying the incidence angle.

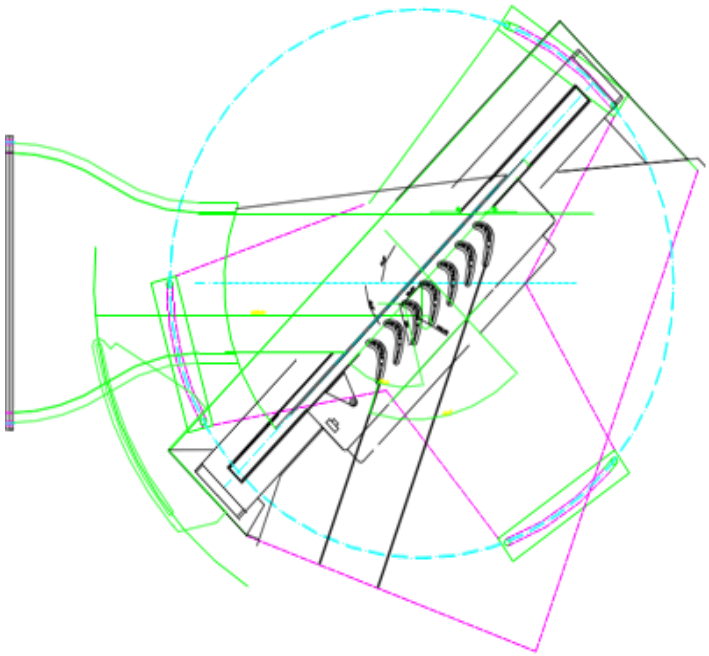

Fig. 3.7 Top view of the incidence angle system

3.3 LPT cascades

In the present work, investigations have been conducted on a series of linear cascades characterized by different pitch-to-chord ratios, hence different static pressure distribution over the vane surfaces. The cascade series tested during these years of research are constituted of 7 vanes and derived from an optimal cascade obtained from the previous work shown in [14]. This optimal cascade was found out after a parametric experimental investigation on the velocity distribution over the suction side aiming to identify the best solution in terms of lower aerodynamic losses under unsteady inflow conditions. Specifically in [14], the velocity peak position over the suction side was varied in order to ensure minimal frictional losses and to allow a smooth acceleration up to the throat, while avoiding at the same time excessive diffusion in the uncovered part of suction side. To this aim, three configurations were tested: forward loaded, mid-loaded and aft loaded. Moreover, the pressure side was designed in order to avoid excessive diffusion near the leading edge and to ensure an optimal acceleration toward the trailing edge. This work led to a first LPT cascade characterized by an aft-loaded velocity distribution, whose static pressure distribution at midspan is shown in black in Fig. 3.8. From this cascade, it has been first increased the pitch cascade by 12 % (blue curve in Fig. 3.8), and then to 20% (red curve in Fig. 3.8), while the other cascade parameters have been kept constant leading to a slight

redesign of the midspan profile in order to maintain the same flow angles. The aim of this pitch variation is the reduction of the engine weight keeping the aerodynamic losses as lower as possible once the cascade is installed in a real engine. From Fig. 3.8, the reader can note that all the cascades investigated have the peak in the same position along the axial direction and a quasi-similar pressure side profile. The main difference occurs on the vane suction side, making the flow path within each cascade different. Specifically, as the pitch-to-chord ratio increases the acceleration in the fore part of the vane suction side is higher as well as the deceleration in its rear part. Therefore, cascade 3 is more prone to flow separation. Furthermore, it can be noted also a difference in the area extension (aerodynamic load) of each cascade, making cascade 3 the one which once installed in a real engine with few vanes, will exchange the same work with the fluid. This counterbalancing effect between weight reduction and losses is a classical argument in LPT applications and it will be explored in the chapter dedicated to the results.

The main parameters of the cascades under investigation in this work are summarized in Tab. 3.1.

Note that for all the cascades under investigation, the vane chord value at both endwalls has been chosen to be 120 mm, in order to provide a good accuracy and a high spatial resolution during measurements, even at low speeds characterized by higher fluctuations.

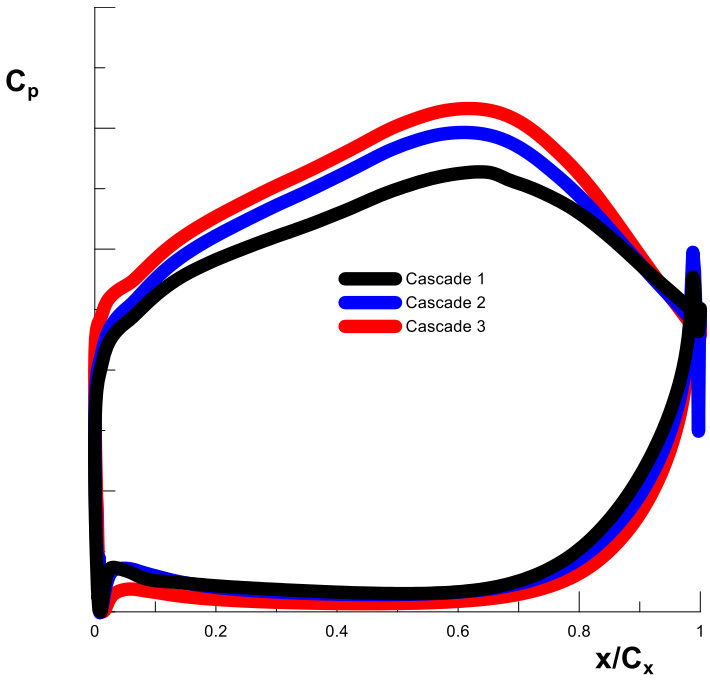

Fig. 3.8 CFD aerodynamic loads at midspan of the cascades under investigation

	Cascade 1	Cascade 2	Cascade 3
Vane count	**7**	**7**	**7**
Vane chord	**120 mm**	**120 mm**	**120 mm**
AR	**2.5**	**2.5**	**2.5**
Velocity peak position	**0.6 C_X**	**0.6 C_X**	**0.6 C_X**
Deflection angle	**100 deg**	**100 deg**	**100 deg**
Zw	**1.1**	**1.232**	**1.32**
DRss	**0.5**	**0.64**	**0.7**

Tab. 3.1 Main parameters of the cascade under investigation

Chapter 4 Measuring techniques

Detailed experimental analysis has been conducted in order to provide a deeper understanding of the phenomena at the source of loss generation in LPT cascades and to quantify the aerodynamic losses. To this aim, different instrumentation and measuring techniques have been used:

- Pressure taps
- Kiel probes
- Hot wire anemometer (HWA)

Pressure taps on vane walls have allowed us to measure the static pressure distribution at midspan along both suction and pressure sides, hence, to evaluate the vane aerodynamic loading at each tested condition.

Kiel probes have been used for total pressure measurements aiming to evaluate the loss coefficient distribution, and therefore the cascade overall loss at each tested condition. Its insensitivity to the flow incidence angle within a range of ± 30° makes this probe particularly suitable for measurements downstream of LPT cascades where velocity defects and flow angle distortions are inherently present.

Hot wire anemometer (HWA) has been instead used for characterization of unsteady phenomena; thanks to its high frequency response, it has allowed us to characterize wakes shed from the upstream rotor in terms of velocity defect and turbulence content.

An in-depth description of these instruments as well as the acquisition system is provided in the following.

4.1 Static pressure taps

Static pressure has been acquired by means of taps installed at midspan along both pressure and suction sides. These taps are small holes of *0.6* mm diameter drilled normally to the vane surface and connected to a pneumatic Scanivalve by means of steel tubes and then to SETRA differential pressure transducers. It is well-known that static pressure measurements are possible through the acquisition of the pressure fluid in a small hole which axis is orthogonal to the flow. If the hole diameter is too large, part of the dynamic pressure will go to stagnation and therefore the static pressure value will be not correct.

Fig. 4.1 shows an example of an LPT vane used in the present work, which has been instrumented for static pressure surveys; it can be noted the tubes made of steel which connect the holes to the Scanivalve.

For all the cascades under investigation, the holes are equally spaced over the vane sides along the streamwise direction in order to guarantee a high spatial resolution during measurements. Measurements have been performed only on the three central vanes of each cascade in order to verify the periodicity flow condition, which is achieved through an appropriate regulation of tailboards and inlet bleeds shown in Fig. 3.3. This flow condition

makes the experimental investigation on linear cascades similar to investigations on annular ones by simulating the potential flow field of each vane. Each vane has been instrumented at midspan with a total of *28* pressure taps, *14* on each vane side. Moreover, for each measuring point, *10000* samples have been collected at a sampling frequency of *1* kHz. The maximum deviation between the loading distributions has been set to *±2%*.

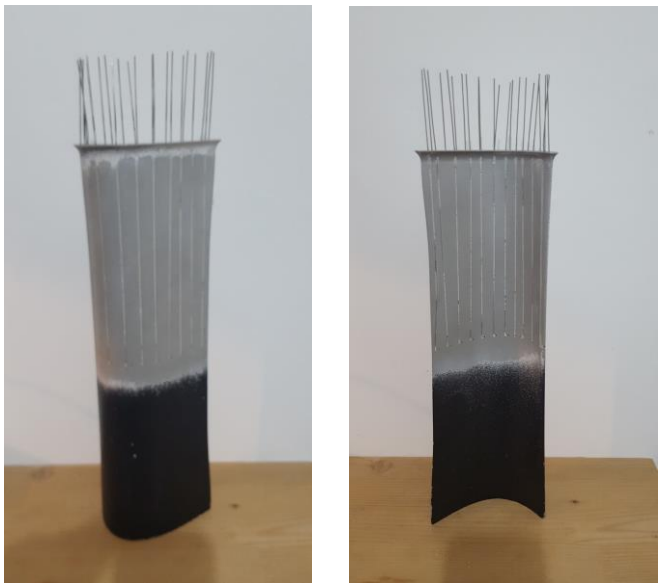

Fig. 4.1 Static pressure taps on an LPT vane

4.2 Kiel probe

Kiel probes are characterized by high precision over a wide range of flow angles, making them accurate in measuring total pressure in the wake region. Indeed, unlike Pitot probes, Kiel probe shroud (shown in Fig. 4.2) acts in order to straighten the incoming flow and remove errors associated with the variation of flow angles during measurements. Moreover, Kiel probes do not require any aerodynamic calibration and are relatively easy to use. During the present investigations, they have been connected to pressure transducers and hence, to a PC which allows to manage the acquisition parameters.

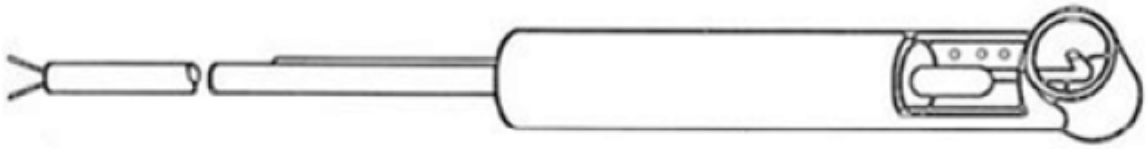

Fig. 4.2 Sketch of a Kiel probe

Two Kiel probes have been used simultaneously in the present work in order to sample the flow in the upstream and downstream sections for three entire pitches. The measuring points

have covered the traverses with variable steps of *3* mm within the wake region and *5* mm in the freestream flow. For each measurement point, *10,000* samples have been acquired with a sampling frequency of *1* kHz. This work has been done in order to quantify the losses of the three central vanes providing a further verification on the periodicity flow condition as well as more data for statistical analysis. The probes have been installed at midway between the leading-edge plane of the cascades and the moving bar system (the former probe) and at *0,33* C_x downstream of the trailing edge (see Fig. 4.3). The simultaneous acquisition minimizes the temporal drifting of the wind tunnel, thus increasing the accuracy in the total pressure comparison between upstream and downstream observations. The relative tangential positions of the two probes avoid aerodynamic interferences since the upstream probe wake leaves the cascade in the adjacent passage with respect to that sampled at the same time by the downstream probe. Moreover, as it will be shown later, this procedure gives the possibility to discuss about loss production due to both wake advection and background turbulence transport as well as the viscous losses into the vane wake region.

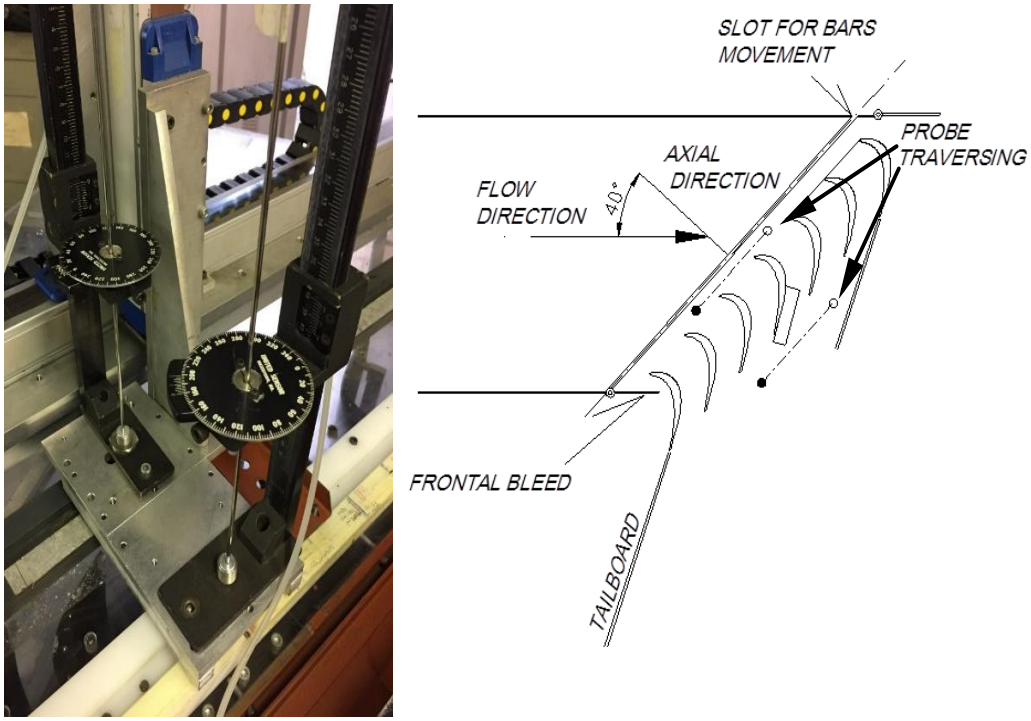

Fig. 4.3 Test section with the probes installed for measurement

Once acquired the total pressure distributions upstream and downstream of the cascades, the loss coefficient can be calculated according to eq. 4.1.

$$\omega = \frac{\overline{p_{t,in}} - \overline{p_{t,ex}}}{\overline{p_{t,in}} - p_{ex}} \tag{4.1}$$

Where the overbar stands for an area-averaged operation.

This procedure differs from the classical one by an area-averaged operation of the acquired data instead of the mass-averaged one. However, at low speeds typical of LPT, the two definitions practically coincide with a deviation of *±0.5%,* as it will be shown in chapter 6.

4.3 Hot wire anemometer

Hot wire anemometer is a well-known device used in turbomachinery applications in order to acquire velocity in periodic or random flows. Its sensing element consists of a thin wire usually made of tungsten, making this probe ideal for velocity measurements in single points. HWA is characterized by a high frequency response (higher than 100 kHz), making it able to resolve high-frequency turbulent phenomena. However, the drawbacks to pay using this instrument are:

- its intrusiveness, which could disturb the flow field under investigation avoiding at the same time acquisition in the near-wall region
- its lower accuracy, about 2% of the measuring velocity
- its fragility due to the wire small diameter which may provoke a risk of breakup during large acquisitions over time

More specifically, a hot wire anemometer consists of:

- a **probe** composed of two antennas supporting a wire (about 1mm long with a diameter of a few micrometers). The wire is made commonly of tungsten since high operating temperatures are required to achieve a good sensitivity during measurements. However, the temperature upper limit is 300 °C in order to avoid its degradation. The small dimensions are instead necessary to reduce as much as possible the probe thermal inertia leading to an optimal frequency response;
- an electronic system such as Wheatstone bridge and operational amplifiers which either maintains the sensing element at a constant temperature **CTA mode** or keeps constant the electric current passing through the wire **CCA mode.** HWA operating in CCA mode although being easy to construct, are characterized by a lower frequency response. Hence, they are less used to characterize high frequency phenomena.

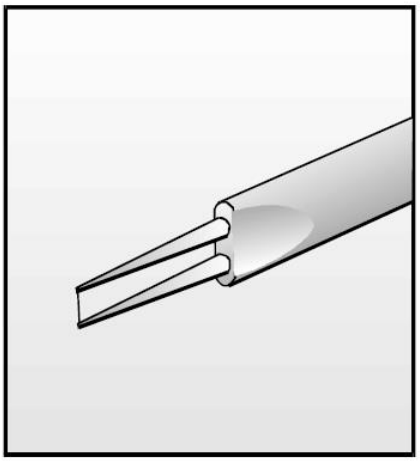

Fig. 4.4 HWA with a single wire

HWA can also be equipped with two or three wires aiming to investigate 2D or 3D flow, respectively.

- **HWA operating principle, features of the HWA used in the present work**

The discussion presented below refers to single wire HWA operating in CTA mode for simplicity and it can be easily extended for two/three wires HWA.

HWA uses the principle of heat transfer from high to low temperature. Its sensing element is a very thin and conductive filament made of tungsten (1 mm long and 5 μm diameter). It is well-known that when an electric current flows in a conductive wire, thermal power dissipates due to Joule effect according to eq. 4.2

$$P_p = RI^2 \tag{4.2}$$

If the wire is immerged in a fluid at rest, the heat is dissipated by natural convection while in a fluid in motion, it is removed by forced convection. The thermal power P_t is expressed as

$$P_t = h(T_w - T_f)\pi dL \tag{4.3}$$

Where T_w is the wire temperature, T_f the fluid temperature, h the convective heat coefficient while d, L are geometric characteristics of the wire.

The wire temperature influences its electric resistance R_w according to eq. 4.4

$$R_w = R_w(20^\circ C) + \alpha_t R_w(20^\circ C)(R_w - 20^\circ C) \tag{4.4}$$

With α_t the temperature coefficient of sensitivity. Note that the fluid nature, its temperature, velocity and pressure are all factors which influence the amount of heat exchanged between the wire and the surrounding fluid. Usually, the wire is inserted in a Wheatstone bridge as an active resistor (Fig. 4.5) and the flow velocity measurement aims to balance the bridge, i.e., $P_t = P_p$

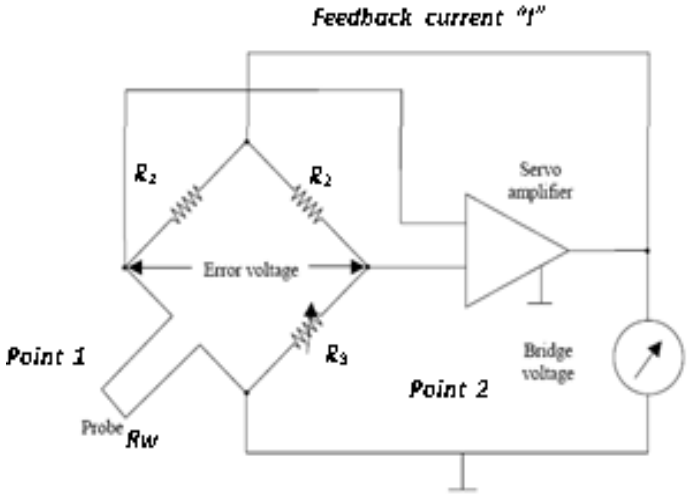

Fig. 4.5 CTA circuit diagram

If the bridge is balanced, the servo amplifier, which acts on the power supply, is in an equilibrium condition and no signal is sent to the generator. When the flow velocity changes, the heat removed by forced convection varies and therefore also the wire temperature as well as its electrical resistance. Thus, the servo amplifier detects an imbalance of the Wheatstone bridge and activates the power supply in order to modify the circuit voltage leading to a variation of the power dissipated by Joule effect until it reaches the thermal power removed from the wire by convection. In this way, the wire is working at a constant temperature, allowing the bridge to stay in an equilibrium configuration when the flow kinematic varies. Therefore, the device works at constant temperature providing the voltage temporal variation of the circuit as an output signal.

All this can be analyzed analytically by writing the heat balance applied on the wire (eq. 4.5) neglecting conduction and radiation

$$R_w I^2 = h(T_w - T_f)\pi dL \tag{4.5}$$

Since $R_w = \frac{E}{I}$ and $h = a + bQ^n$

Therefore, $\frac{E^2}{R_w} = a(T_w - T_f)\pi dL + bQ^n(T_w - T_f)\pi dL$ (4.6)

The exponent *n* assumes the value 0.5 when the wire is infinitely long. All the quantities in eq. 4.6 can be determined directly except the Nusselt number, which is of paramount importance in evaluating the wire cooling velocity. An alternative is the use of the calibration curves; in the case of HWA, calibration curve is known as the King's law (eq. 4.7)

$$E^2 - E_0^2 = BQ^n \tag{4.7}$$

Where:

E_0 = voltage when the fluid has no motion (linked to the natural convection)

Q = cooling rate

B, n = empirical coefficients (B is a function of the wire geometry and the temperature *gradient* while n is about 0.5)

E = actual voltage.

From a practical point of view, the calibration is performed by immerging the probe sensing element within a free jet facility. The sensor is located at the exit facility with its axis orthogonal to the flow direction. The calibration procedure consists in measuring the voltage output while varying the flow velocity, making possible the evaluation of coefficients B and n by a Least-Squares method. Hence, it is possible during the measurement phase to derive the flow velocity once known the voltage output.

Fig. 4.6 shows a clear picture of the hot wire used in the present work. It is a Dantec single-sensor miniature C-type boundary layer hot-wire probe (type 55P13) employed downstream of the moving bar system aiming to characterize incoming wakes in terms of velocity defect and turbulence intensity. The device has provided a minimization of the flow-wire incidence angle variation effects during the incoming wake period. The system operates in the CTA mode, with an over-heat ratio, i.e., the ratio between the wire resistance at operating temperature and that at ambient temperature set to *0.8*. Measurements have been carried out at midspan in the front of the central blade of the cascade, at an axial distance of *0.15* C_x from the blade leading edge. A NI-DAQ analogic to digital converter has been used to sample the output voltage. Each incoming wake period has been solved with 100 measuring points, and phase-locked quantities have been averaged on *1000* shaft revolutions.

Fig. 4.6 HWA installed for incoming wakes characterization

4.4 Data logging

Static pressure taps and Kiel probes exposed in the previous sections have been connected to SETRA differential pressure transducers. They are characterized by a high accuracy with

uncertainty of ±*0.023%* of full-scale range (±*620* Pa) and a high sensitivity. Moreover, they are connected via BNC cables to a NI-DAQ analogic to digital converter which output is a voltage related to the quantity under measurement. The whole acquisition system is controlled by a PC running LabVIEW software which allows the control of parameters acquisition: number of measuring points, their position, sampling frequency, among others.

During static pressure measurements, a pneumatic Scanivalve were used aiming to avoid the use of a ‘’giant’’ number of pressure transducers. It is an interface between the static pressure taps and the pressure transducers and is made of 5 channels, each one having *12* inputs and *1* output allowing up to *60* simultaneous pressure measurements.

Chapter 5 Data analysis

The present chapter deals with the mathematical equations underlying the post-processing techniques used in the present thesis. An emphasis is put on the POD procedure since it is the cornerstone of the present work.

5.1 Statistical data processing

During the present experimental investigations, measurements of each parameter under observation have been conducted several times in order to provide accurate values and reduce the variation inherently related to data acquisition. Therefore, it is possible to calculate both statistical first and second order moments which provide the most probable value and the deviation from it, respectively. Furthermore, in the case of aerodynamic measurements the second moment is an indicative of the turbulence level.

In the following, a brief recall on these moments is provided as well as how to evaluate uncertainty during measurements.

- **First and second order moments: mean and variance**

Given N observations of a generic quantity v, i.e., N measurements of v carried out in different instants of time, the average value of this quantity can be calculated through the following expression:

$$\overline{v} = \frac{1}{N}\sum_{i=1}^{N} v(i) \tag{5.1}$$

It is worth noting from eq. 5.1 that a large number of samples provides the true mean value and an optimal statistical reconstruction of the signal. It is also possible to define the oscillating component of the quantity under observation according to

$$v'(i) = v(i) - \overline{v} \tag{5.2}$$

This signal fluctuation around the average value can be interpreted as the deviation from it. It is possible to calculate an effective fluctuation with respect to the average value through the evaluation of the standard deviation according to the following expression:

$$\sigma = \sqrt{\frac{1}{N-1}\sum_{i=1}^{N}(v(i) - \overline{v})^2} \tag{5.3}$$

The second-order statistical moment assumes always positive or zero values being representative of the data dispersion around the average value. This dispersion depends mainly on the nature of the phenomenon under observation but also on casual errors during measurements.

- **Uncertainty**

In statistical analysis, the rms contributes to the definition of the relative uncertainty on average according to:

$$I = \pm \frac{z\sigma}{\bar{v}\sqrt{N}} \tag{5.4}$$

where:

z is a factor that depends on the confidence level (see Tab. 5.1)

N is the number of samples

σ is the standard deviation, i.e. the rms of the measured quantity

Confidence level	90%	95%	99%
Z	1.645	1.96	2.58

Table 5.1 Reliability according to the level of confidence

5.2 Phase-average

Phase averaging is widely used in fluid mechanics in order to determine statistical moments of quasi- periodic flows since they contain both deterministic and random fluctuations.

Periodic fluctuations in each flow can be resolved by averaging over N periods (cycles) of the phenomena acquired at a phase *j* of each period according to eq. 5.5

$$\langle v_j \rangle = \frac{1}{N} \sum_{i=1}^{N} v_{j,i} \tag{5.5}$$

The procedure can then be repeated for all the different phases of interest leading to a phase evolution in time. Once the phase-average has been calculated, it is also possible to evaluate the deviation from the phase-averaged value associated to a cycle *i*:

$$\Delta v_{j,i} = \left(v_{j,i} - \langle v_j \rangle \right) \tag{5.6}$$

It is therefore possible to calculate the standard deviation:

$$\sigma_j = \sqrt{\frac{1}{N-1}\sum_{i=1}^{N}\left(v_{j,i} - \langle v_j \rangle\right)^2} \tag{5.7}$$

Eq. 5.7 allows to observe the average value of a fluctuating random signal, with respect to its phase-averaged value, and therefore allows to quantify periodic turbulent flow like the wake shed from the moving bar system.

In the present work, phased-locked quantities have been used in order to survey both velocity defect and turbulence intensity downstream of the rotor simulating upstream wake while varying its fundamental parameters. This aims to provide further insights on the loss process due to wake advection into the downstream cascade. The acquisition start for phase-locking has been triggered by means of one pulse per rotor revolution obtained from a shaft encoder (shown in Fig.5.1), aiming to determine the beginning of each rotor revolution.

Fig. 5.1 Encoder on the rotor shaft

5.3 Proper Orthogonal Decomposition (POD)

Proper Orthogonal decomposition (POD) is a mathematical procedure which provides a modal decomposition of a dataset. Usually, applied to data ensemble obtained during experiments or numerical simulations, POD provides a compact basis on which the data ensemble projection is maximized in the sense that it contains the main behavior of the original dataset. This *"robust"* representation property has suggested POD as an optimal technique widely used in various applications like image processing, data compression, fluid mechanics, just to cite a few examples.

In the fluid dynamics community, POD was first introduced in its classical formulation by Lumley [68] for the analysis of turbulent flows. A few years later, Sirovich [69] formulated the snapshot POD useful in recognizing coherent structures within turbulent flows reducing the computational efforts. At that time, the author applied POD to spatio-temporal data and extracted the most energetic structures embedded into the flow. In fact, the modal

decomposition provided by POD separates spatial from temporal information and orders the modes by their energy content. Similar works on bounded flows and turbulent jets can be found in the literature aiming mainly to provide statistical information on the most energetic structures and a deeper understanding of the flow physics (see [70] for example). Recently, the POD capability in identifying coherent structures has been used by Lengani et al. [71] in order to separately account for both coherent and stochastic contribution to the overall energy of the velocity fluctuations in separated flows. Indeed, once isolated the group of POD modes related to large scale coherent structures, the authors were able to compute their partial shear stress, their kinetic energy and their contribution to turbulence production by combining the spatial distributions of the modes of the two velocity components with the shear strain of the mean velocity field. A similar work has been done in [72-74] in order to split the loss generating mechanisms within LPT cascades and to provide the contribution to the overall losses due to different mechanism. Specifically, the authors applied POD to LES data and by means of the analysis of the Fourier transform of the POD temporal coefficients, they were able to associate each mode (or group of modes) to a particular flow physics (like boundary layer separation, or incoming wake related effects). Hence, it has been possible to quantify the contribution to the loss generation of the wake migration into an LPT cascade and its interaction with the suction side boundary layer. Computation of partial shear stress and kinetic energy of the coherent structures by means of POD has been recently used in [75] where the authors have provided a new definition of the energy transfer term between the two scales involved in the transport equations of Laminar Kinetic Energy (LKE) codes. Indeed, using the POD scale separation and the Hussain and Reynolds flow decomposition theoretical framework [76], they were able to rewrite the main quantities involved in LKE codes, like the laminar and turbulent production terms and the energy transfer rate between the two scales.

POD has also been widely used in order to provide temporal reconstruction of non-time-resolved data aiming to describe in detail the dynamics of structures embedded within flows. To this aim, Graftieaux et al. [77] and successively Van Oudheusden et al. [78] showed that the phase relation of two POD temporal coefficients can be used to identify the phase of each flow realization within a periodic phenomenon. Moreover, Legrand et al. [79] proved that for pseudo-periodic convective flows the temporal coefficients of the first two POD modes can be adopted to define a “temporal sorting coefficient” that may be used as a trigger to phase-average operations. Based on these works, Lengani et al. [71] were able to associate each PIV flow field to a specific phase within the vortex shedding cycle in order to provide further insights on the dynamics of the Kelvin-Helmholtz instabilities over a flat plate under separated flow conditions and to characterize the evolution of structures (streaky structures and eddies) within the suction side boundary layer of an LPT cascade under the influence of incoming wakes [80-81].

The challenging task in resolving NS equations while reducing the computational cost has involved over the years the POD technique in order to build low-order dynamic models. In this case, NS equations are projected onto POD basis leading to a system of ordinary differential equations (ODEs) for the time dependent coefficients. It is therefore possible to truncate the number of ODEs provided by the POD technique leading to a computational effort reduction [82-83].

Less commonly, POD is applied to design space like in the present thesis. In this case, it has been mainly used in combination with some interpolation techniques (like the spline interpolation for example) in order to reconstruct full flow fields around airfoils using partial

data and also to perform airfoil design optimization by describing flow fields around new airfoil geometries, using the information about the flow over few selected geometries (see [84] and [85] for instance). This is the same logic used in the present work where POD has been used with Least-Square Methods LSM in order to predict total pressure loss within a design space acquiring only a few number of conditions.

Now, let's consider an ensemble of observations $U = U(x_i, t_j)$ which are a function of both space and time (U can denote for example the fluctuating velocity of a given field in a given time interval). From a mathematical point of view, applying POD to U is nothing else than diagonalizing its correlation matrix $U^T U$ (or UU^T depending on the information needed for the post-analysis) into the classical form $\boldsymbol{\phi\lambda\chi}$, where $\boldsymbol{\lambda}$ is a diagonal matrix, while $\boldsymbol{\phi}$ and $\boldsymbol{\chi}$ are respectively orthogonal and orthonormal matrices (or vice versa). The idea behind this diagonalization is that it is possible to find out an optimal basis $\boldsymbol{\chi}$ (or $\boldsymbol{\phi}$) in which the correlation matrix can be written in order to remove all the redundant information (off-diagonal elements of $\boldsymbol{\lambda}$) and to re-order the largest variances of the information under observation, i.e., the diagonal elements of $\boldsymbol{\lambda}$ are arranged in a decreasing way. Indeed, since $U^T U$ is a self-adjoint matrix (square and symmetric), linear algebra allows to write:

$$U^T U = \boldsymbol{\chi\lambda\chi^{-1}} \tag{5.8}$$

Where $\boldsymbol{\chi}$ is the matrix made of eigenvectors of $U^T U$ and $\boldsymbol{\lambda}$ is a diagonalized matrix which contains the eigenvalues of $U^T U$. Furthermore, since $U^T U$ is symmetric, $\boldsymbol{\chi}$ is orthogonal and hence, it can be written as a unitary matrix $\boldsymbol{(\chi^{-1} = \chi^T)}$. Thanks to the orthonormality of $\boldsymbol{\chi}$, it is possible to project the original data on the basis spanned by $\boldsymbol{\chi}$ according to

$$\boldsymbol{\phi = U\chi} \tag{5.9}$$

In this new basis, the covariance matrix is $\boldsymbol{\phi^T\phi} = \boldsymbol{(U\chi)^T U\chi = \chi^T U^T U\chi = \chi^T\chi\lambda\chi^{-1}\chi =}$ $\boldsymbol{\lambda}$, which does not contain any more off-diagonal elements, hence redundant information has been removed in this basis. For more details on the analogy between POD and matrix diagonalization, the reader can refer to [86].

A fundamental aspect when dealing with POD is the possibility to neglect the lower values of the eigenvalue's matrix $\boldsymbol{\lambda}$. Doing so, the new basis spanned by $\boldsymbol{\chi}$ results more compact and the projection $\boldsymbol{\phi}$ of the original dataset becomes a lower dimensional dataset which contains the main information of $\boldsymbol{\phi}$. Therefore, the use of $\boldsymbol{\phi}$ instead of $\boldsymbol{U}$ as a surrogate will produce less computational effort during data post-processing. From another point of view, this dimension reduction also identifies the rank of the problem at hand. As it will be shown later, when applying POD to a given design space, determining the problem rank means to find out the number of tested conditions independent within the design space, useful in saving time during experimental testing.

From now until the end of the chapter, let us focus on the equations underlying the POD procedure. In the original approach of Lumley [68], the POD looks for the function Φ that maximizes the normalized square projection of a given dataset in a mean sense, i.e.:

$$\max_{\|\Phi\|=1} \frac{\langle |(U,\Phi)|^2 \rangle}{\|\Phi\|^2} \tag{5.10}$$

Here $\langle . \rangle$ denotes the ensemble average, while (,) and $\|.\|$ indicate the L^2 inner product and norm, given as:

$$(U(x,t_i),\Phi(x)) := \int U(x,t_i).\Phi^*(x)dx \qquad \|\Phi(x)\| := \sqrt{(\Phi(x),\Phi(x))} \tag{5.11}$$

where * denotes the conjugate complex. Using the calculus of variations, the function $\Phi(x)$ can be shown to provide a solution for the following Fredholm's equation:

$$\int_\Omega R(x,x').\Phi^*(x')\,dx' = \lambda\Phi(x) \tag{5.12}$$

where Ω is the spatial domain of interest, λ is the Lagrange multiplier, and $R(x,x')$ is the ensemble averaged two-points spatial correlation tensor, defined as:

$$R(x,x') := \langle U(x,t_i) \otimes U(x',t_i) \rangle \tag{5.13}$$

where $\otimes$ is the dyadic product. In the classical approach of Lumley [68], the eigenfunctions $\Phi(x)$ of the correlation tensor $R(x,x')$ constitute the POD spatial modes, while the related temporal coefficients are obtained by projection. Note that, since $R(x,x')$ is a self-adjoint and non-negative operator, the POD modes $\Phi(x)$ are implicitly orthogonal, which is a suitable feature for reduced order models construction.

The successive snapshot POD was introduced by Sirovich [69] to reduce the computational requirements of the classical POD calculations. Starting from the formulation of Lumley, Sirovich derived a discrete eigenvalue problem for the correlation matrix C defined as:

$$C^{ij} := \frac{1}{N_t}\big(U(x,t_i),U(x,t_j)\big) \tag{5.14}$$

where N_t is the number of observations. From the procedure point of view, data collected for a given condition have been ordered in a snapshot matrix *U*, whose columns contain all the instantaneous acquisitions, that is, the matrix U size is $N_p \times N_t$, where N_p is the number of spatial positions considered. In this way, eq. 5.14 can therefore be rewritten in a matrix form as:

$$C := \frac{1}{N_t} U^T U \tag{5.15}$$

Note that since *C* is a real symmetric positive-definite matrix, its eigenvalues are real and nonnegative and are sorted according to $\lambda_1 \geq \lambda_2 \geq \ldots \geq \lambda_m$. Each eigenvalue is representative of the energy associated to the corresponding mode. The related eigenvectors $\chi_m = [\chi_m{}^1, \ldots, \chi_m{}^{N_t}]$ provide a complete orthogonal basis and are obtained from the following eigenvalue problem:

$$C\chi_m = \lambda_m \chi_m \tag{5.16}$$

Where $m = 1, \ldots, N_t$.

In the snapshot POD the temporal coefficients are therefore obtained from the eigenvectors of the correlation matrix *C*, and the POD modes are computed as a linear combination of the observations:

$$\Phi_m(x) = \frac{1}{\sqrt{N_t}} \sum_{i=1}^{N_t} \chi_m{}^i \, U(x, t_i) \tag{5.17}$$

The POD modes $\Phi_m(x)$ obtained from eq. 5.17 also provide a complete orthogonal basis and they still satisfy eq. 5.12.

5.3.1 POD applied to design space

In the present work, data constituted of total pressure loss distributions have been arranged according to eq. 5.18 aiming to construct the snapshot matrix *U*

$$U = \begin{pmatrix} C'_{pt\_1}(y_1) & \ldots\ldots & C'_{pt\_N}(y_1) \\ \vdots & \ddots & \vdots \\ C'_{pt\_1}(y_{N_y}) & \ldots\ldots & C'_{pt\_N}(y_{N_y}) \end{pmatrix} \tag{5.18}$$

Where each column is formed by the difference between the total pressure loss coefficient distribution measured with a datum combination of the parameters and a reference distribution (in this work considered as the total pressure loss coefficient distribution measured in the steady case), i.e.,

$$C'_{pt\_i}(y_j) = C_{pt\_i}(y_j) - C_{pt\_reference}(y_j) \tag{5.19}$$

With $i = 1, \ldots, N$ the number of tested conditions and $j = 1, \ldots, N_y$ the number of measuring points.

Hence, the cross-correlation matrix can be evaluated with the relative POD modes, POD design coefficients and eigenvalues according to eqs. 5.15-5.17. Thus, based on the property of the POD it is easy to show that:

$$C_{pt}(y) = C_{pt\_reference}(y) + \sum_{i=1}^{N} \sqrt{\lambda^{(i)}} \chi^{(i)}(design\ space) \phi^{(i)}(y) \quad (5.20)$$

The engineering interpretation of the decomposition is directly provided by eq. 5.20. The eigenvalues λ provide the amplitude of each POD mode, thus the indication of the number of modes requested to reconstruct the whole loss coefficient (its deviatoric part with respect to the reference distribution), the POD modes ϕ give the spatial distribution of the basis function describing losses in the *y (pitchwise)* direction, while the eigenvectors χ are the only quantity dependent on the combination of the design parameters, thus they provide the weighting term empathizing the role played by each parameter. In other words, the eigenvalues identify the number of modes requested to well describe the loss distribution (i.e. the rank of the problem), the POD modes highlight the spatial region where the loss coefficient is high, and finally the eigenvectors give the amplification factor to be applied to the modes for each different combination of the design parameters. As a consequence of this interpretation, the comparison of the weighting term χ for the different conditions tested clearly identifies the parameter most influencing the loss produced into the cascade.

Chapter 6 Results and discussion

Experimental investigations have been carried out in order to evaluate the aerodynamic performances of LPT cascades and to identify the most innovative solutions for the future generation of aero engines.

The cascades under investigation, as already described in detail in chapter 3, consist of seven vanes and present the common characteristics of aspect ratio 2.5 and flow deflection angle 100 °, but differ by their pitch-to-chord ratio and hence, their aerodynamic loadings. Therefore, a comparison between the cascade performance will provide useful information on the loss dependency from the solidity, providing a framework for optimized pitch-to-chord ratios for LPT cascades.

In order to obtain a complete overview of the cascade behavior under the different operating conditions characteristic of a real engine environment, the tests have been carried out under the following conditions:

- Flow coefficient 0.675
- Freestream turbulence intensity: 4 % and 5.2 %
- Steady and unsteady inflow conditions
- Flow Reynolds number from 70000 to 300000
- Incidence flow angle from -9° to +9°

Combination of the previously mentioned parameters have provided an in-depth investigation of each cascade evaluating the following objective functions:

- Aerodynamic loading
- Profile losses

The aerodynamic vane loading has been measured by means of pressure taps located at midspan of the three central vanes of each cascade, connected to a Scanivalve and hence, to pressure transducers as described in chapter 3. It will be shown in the form of adimensionalized static pressure coefficient C_p as a function of the axial coordinate x made dimensionless by the axial chord C_x.

The profile losses have been instead measured by means of two Kiel total pressure probes described in chapter 4, placed on a two-dimensional electronically controlled handler that allows their translation in the measuring planes. Hence, it has been possible to acquire both upstream and downstream total pressure fields for the three central vanes of the cascades at each tested condition, and through an area-averaged operation evaluate the profile losses.

Note that for all the operating conditions investigated, tests have been carried out in a periodic flow condition. As said previously in chapter 4, this condition is reached when the vane aerodynamic loading and total pressure distributions of the three central vanes are superimposed. Therefore, only results related to the central vane will be shown since the remaining vanes will provide no further information.

The results obtained for the reference cascade (cascade1) are reported in the following sections, in order to show the potentiality of the measuring methods in capturing the main flow physics within LPT cascades, as well as to provide an overview of the results achieved

under the variation of design parameters. The measurements on the other two cascades have been performed under the same conditions and with similar experimental investigation methods. Their results will be not shown since they provide no further information on the loss dependency from the design space parameters investigated in the present work. Nevertheless, some results will be presented aiming to provide the vane loading effect on loss distribution.

Experimental results will show that loss distributions are dispersed in the physical space and affected by every design space parameter. Therefore, it has been necessary to find out a surrogate space able to describe the loss process while being more compact. To this aim, POD has been applied to loss distributions. This aims to find out an optimal compact space able to describe the overall loss process with a low rank representation (LRR). Furthermore, a smooth kernel has been defined by means of LSM within the POD subspace aiming to extrapolate data. The procedure has been generalized by applying it to larger datasets obtained from data acquisition on two cascades characterized by different geometrical parameters.

Prior to show the results, the flow characterization within the wind tunnel under both steady and unsteady flow conditions is discussed.

6.1 Turbulence grid characterization

Characterization of the flow downstream of the turbulence grid made of bars of *5 mm* diameter arranged in order to form a *5x5 mm*^{2} square, has been conducted in order to ensure the right value of FSTI at the LPT cascade entrance, and hence provide cascade testing under realistic flow conditions. To this end, hot wire measurements have been carried out varying both Re and the distance from the turbulence grid. Dependence of FSTI from the distance with Re as parameter is shown in Fig. 6.1. Note that the measuring point is *10 mm* from the cascade entrance. A quasi-linear turbulence decay along the wind tunnel axial direction can be seen for both Re as the probe moves away from the grid. This trend is due to the absence of any external force able to sustain the turbulence as the flow convects downstream. Furthermore, the Re = 70000 case shows higher turbulence values at each position. From this analysis, it has been decided to put the turbulence grid at about *570 mm* from the cascade inlet, which is more than five chords upstream of the blade leading edge. This allows a FSTI value of approximately 4 %.

The Fourier transform of the velocity signals has allowed a further flow characterization downstream of the turbulence grid: spectra relative to each Re tested in the present work are reported in Fig. 6.2. The figure presents a typical trend of isotropic and homogenous turbulence, confirming the possibility of using a turbulence grid to provide a uniform and controlled turbulence field at the cascade entrance. Furthermore, as Re increases the velocity spectra undergoes an upwards translation, making higher Re values characterized by high energy content than lower Re ones in both high and low-frequency ranges. The reader can also note a slight difference in the inertial sub-range (note the slope of each curve at intermediate frequency values) due to a different transfer between large-scale structures and lower ones.

A final verification on the flow uniformity in the pitchwise direction at the cascade entrance has been done by means of HWA and Kiel probe in order to check if inflow conditions vary in the pitchwise direction, and hence guarantee the same inlet conditions for the three vanes of interest. Total pressure results for the case Re= 300000 with incidence angle as parameter are shown in Fig. 6.3. They cover four entire pitches and the reader can see an almost uniform inlet flow. Note that variation observed has been found within 0.5 %.

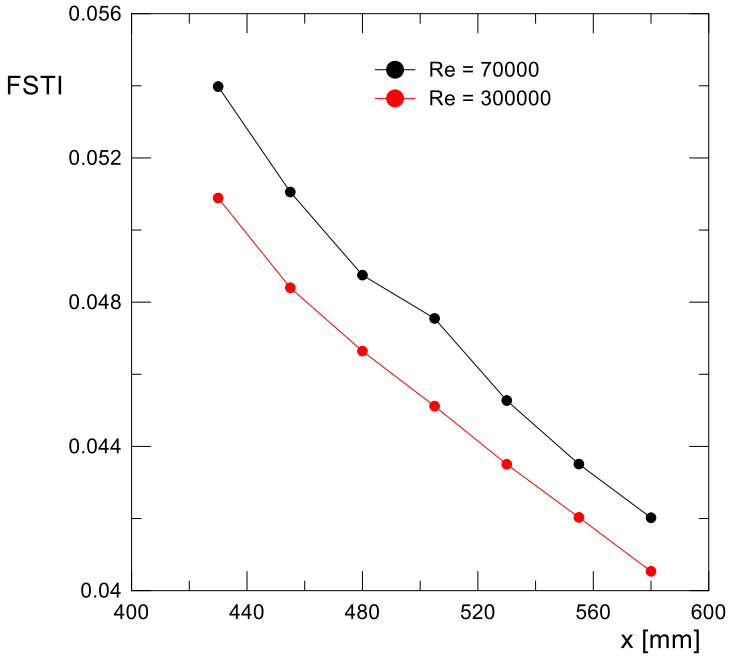

Fig. 6.1 Effect of the distance from the grid on turbulence intensity

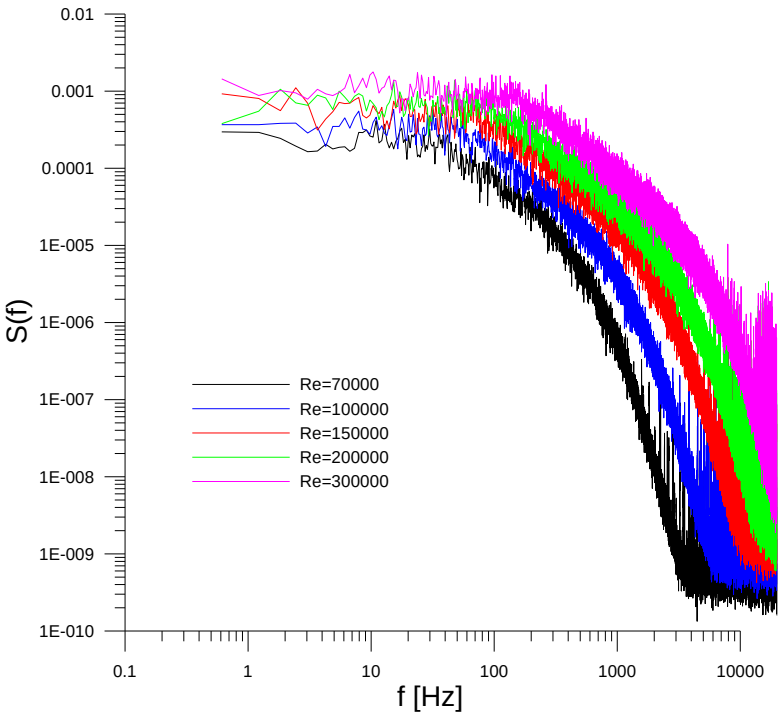

Fig. 6.2 Freestream velocity spectra for different Reynolds numbers

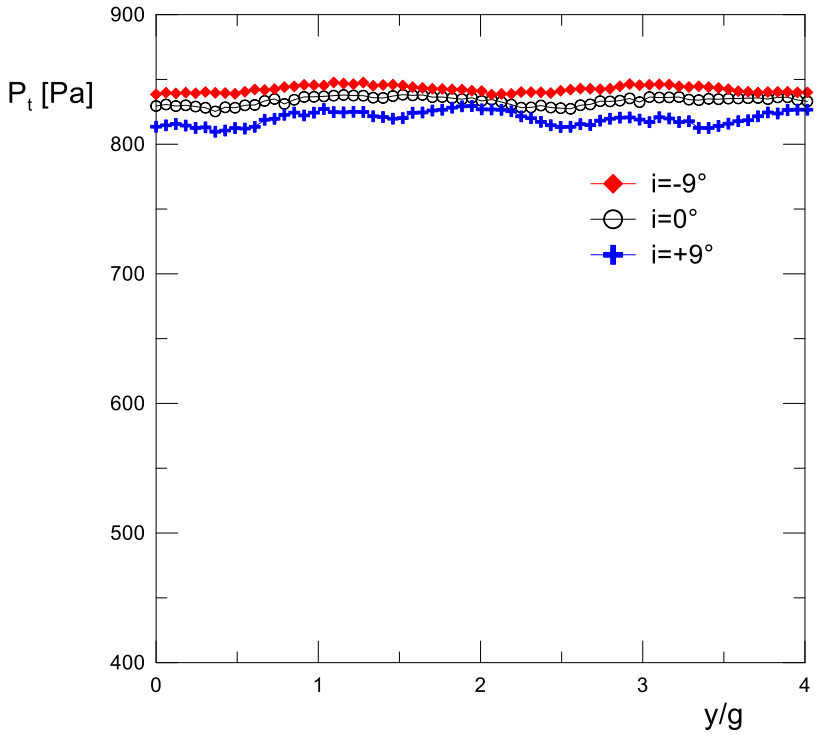

Fig. 6.3 Total pressure distribution in the pitchwise direction at the cascade inlet

6.2 Incoming wakes characterization

The fundamental parameters of the moving bar system which simulates the upstream rotor have been changed in order to evaluate the cascade performance under different flow incoming conditions. Specifically, the bar diameter and pitch have been varied to change the incoming wake momentum defect, the turbulence intensity peak into the wake and the reduced frequency. Three different bar pitches have been tested, corresponding to the reduced frequencies f^+ = 0.46, 0.575 and 0.69. For each reduced frequency three different bar diameters have been considered D=2.5 mm, 3 mm and 3.5 mm, for two different extensions of the axial gap between the bars centerline and the cascade leading edge plane. The low gap case (LG) refers to a distance of 0.33 C_x between bars and the leading edge, while the high gap case (HG) refers to a distance of 0.52 C_x. Overall, 18 different combinations of the wake parameters have been tested, spanning a large variation of the design space.

For each condition, an in-depth characterization of the unsteady incoming wake entering the downstream cascade has been done by means of phase-locked hot-wire measurements. Note that inlet flow angle has been set to the nominal one. In Figs. 6.4, the phase-locked velocity and turbulence intensity distributions measured at the highest and the lowest reduced frequencies (the nominal one is not shown to improve the plot readability) and for the largest and smallest bar diameters (again the central condition is not shown) are reported. These data refer to the low axial gap condition, while those referring to the high axial gap are reported in Figs. 6.5.

At fixed bar diameter, the momentum defect and the turbulence intensity peak into the incoming wake are practically kept the same. The reduced frequency variation mainly alters the distance between adjacent wakes. Conversely, the larger the bar diameter the higher the turbulence intensity peak and the momentum deficit at the wake centerline. The wakes also appear evidently wider. These strong modifications of the wake structure due to the bar diameter are expected to significantly modify the bowing, tilting and dilation processes that will occur during migration of the wake across the downstream cascade, thus altering the loss expectation, as described in [50]. Conversely, the reduced frequency variation is expected to drive mainly the frequency at which losses due to bowing, tilting and dilatation occurs. Strong effects are also due to the variation of the axial gap. Fig. 6.5 makes evident that, for both diameter and reduced frequency, the larger the distance of the bar system from the cascade leading edge plane the more diffused the incoming wake, as expected. The phase-locked velocity does not show the local peak observable at low gap, thus the inflow to the downstream cascade is even more uniform at this high gap condition. The velocity defect entering the downstream cascade is significantly modified, thus again affecting the loss generation during migration of the upstream wake in the downstream cascade, and their interaction with the blade boundary layers. Moreover, the turbulence intensity peak reduces significantly, with maximum values that does not exceed 0.3 for the largest diameter conditions. This is expected to alter the wake - suction side unsteady transition phenomena.

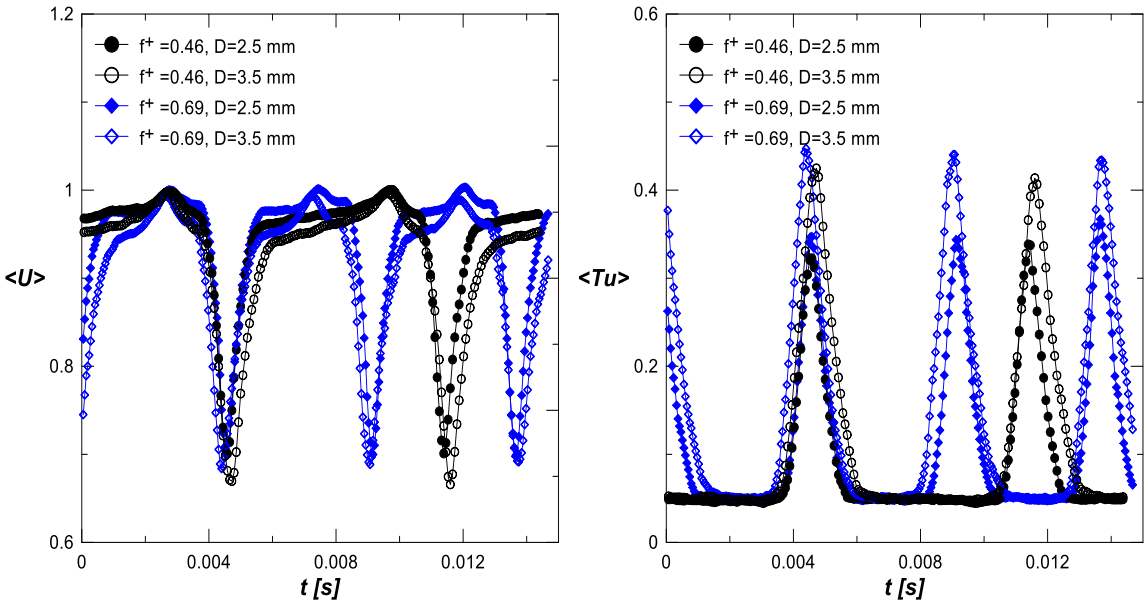

Fig. 6.4 Phase-locked (left) velocity distributions and (right) turbulence intensity at low axial gap

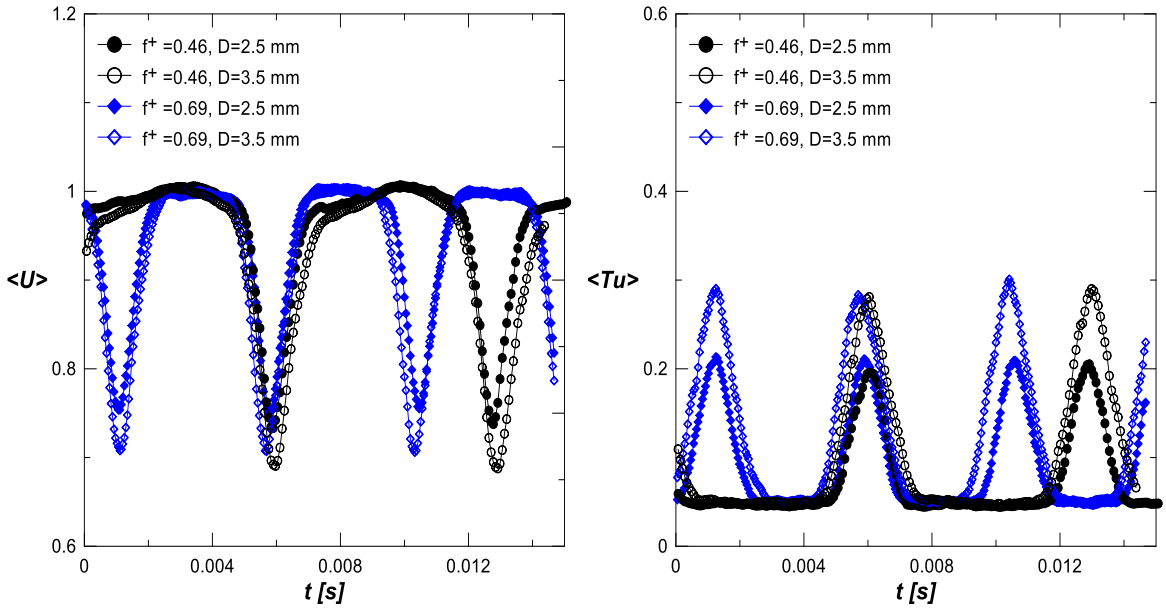

Fig. 6.5 Phase-locked (left) velocity distributions and (right) turbulence intensity at high axial gap

6.3 Losses in physical space

6.3.1 Accuracy of the experimental procedure

In the present work, the experimental procedure exposed in chapter 4 has been used in order to evaluate losses within the LPT cascades. As shown in chapter 4, it differs from the classical procedure by a simultaneous acquisition of the total pressure upstream and downstream of the cascades, allowing the loss evaluation through an area averaged operation instead of the well diffused mass-averaged one.

The efficiency of this procedure is shown in Fig. 6.6, where a comparison of losses evaluated by means of the two techniques are shown for the reference cascade while varying Re under unsteady inflow conditions. The data have been made dimensionless by the loss value obtained from the present procedure at Re = 70000. The reader can note that both techniques show a similar trend, viz. as Re increases they both provide lower losses since viscous effects are less important, in accordance with works in the literature [6, 14]. Furthermore, at higher Re the curves are practically superimposed while at lower Re, there is an offset between the curves, which is maximum at Re = 100000. However, this offset induces a relative variation of approximately 4% which can be attributed to the systematic error inherently present during measurements.

Although the results are similar, the present experimental technique makes use of Kiel probes, which are less influenced by the flow angle variation than the 5-hole probe used during the classical procedure. Moreover, Kiel probes are relatively easy to use and as it will be shown later, the present technique gives the possibility to discuss about the loss production due to migration of both homogeneous and wake transported turbulence while varying the design parameters. This aims to provide further insights on the loss process within the LPT cascades through an understanding of the flow physics governing the LPT cascade operation for the different values of the design parameters.

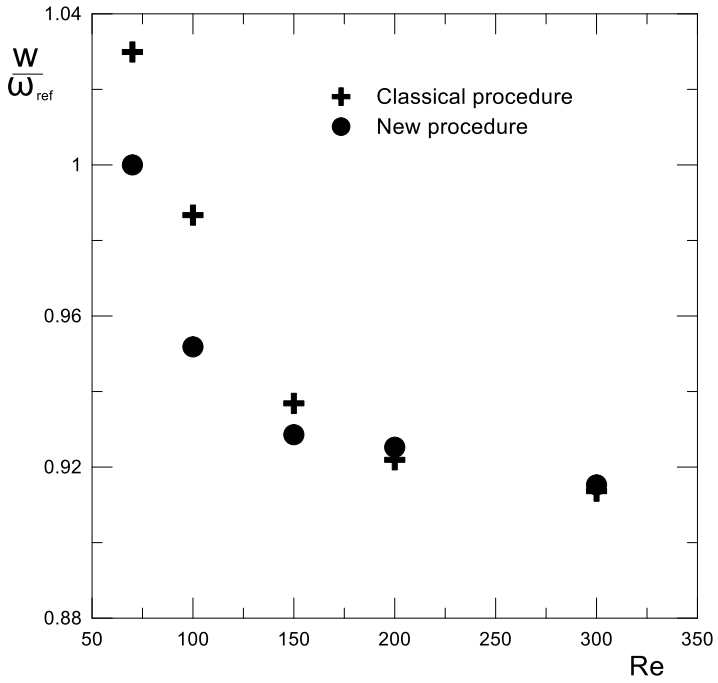

Fig. 6.6 Comparison between losses obtained from the two experimental procedures

6.3.2 Freestream turbulence effects

In the present work, two values of FSTI (4% and 5.2%) have been tested in order to provide the effects of the freestream turbulence intensity on LPT losses. Measurements have been acquired under steady and unsteady inflow conditions, varying Re in the range [70000 - 300000].

a) Steady inflow conditions

The effects of FSTI on the vane loading distribution under steady inflow conditions are reported in Fig. 6.7 for different Re numbers. The reader can note that the differences between the curves in each plot occur over the vane suction side, mainly at lower Re conditions. Specifically, the curves in Fig. 6.7(a) show the presence of a separation bubble over the rear part of the suction side, evidenced by an abrupt slope change. Moreover, the lower FSTI shows a large bubble which does not reattach at the vane trailing edge and introduces blockage effects in the trailing edge plane, as make evident by the higher Cp value in the last measuring point. This leads to the modification of the flow path along the suction side with a consequent slight reduction of the aerodynamic loading also in the frontal part of the suction side.

As largely explained in literature and in chapter 2, freestream turbulence amplifies velocity fluctuations along the inflection line of the separated shear layer. This leads to the shear layer roll-up associated with the Kelvin-Helmholtz instability, and a consequent release of large-scale vortices, which breakdown induces transition. A momentum transfer towards the wall, which enhances the bubble reattachment, always follows the large-scales breakdown. In the lowest FSTI case shown in Fig. 6.7(a), the momentum transfer to the wall is not intense enough to induce the boundary layer reattachment. As FSTI increases, the momentum

transfer increases leading to the bubble reattachment at the trailing edge. This is expected to produce lower losses at high FSTI for this Re number tested.

As Re increases, the bubble becomes shorter and discrepancy between the two curves slightly diminishes (see Fig. 6.7(b)). Once again, the FSTI acts only over the vane suction side. A further increase in Re suppresses entirely the bubble and, as it can be seen in Figs. 6.7(c), (d) and (e), FSTI variation has no more effect on the front part of the vane loading distribution. However, a slight deviation between the curves is visible from the velocity peak on the suction side towards the trailing edge, which is extended of about 18% of the axial chord. This may be attributed to a different boundary layer excitation by FSTI and measurement error.

Overall losses obtained under steady inflow conditions are reported in Fig. 6.8. Results have been made dimensionless by the loss value at low FSTI and Re = 70000. The figure summarizes what has been anticipated in the previous paragraph. Indeed, at lower Re values, the higher FSTI provides lower losses, due to the shorter extension of the bubble over the rear part of the suction side. As Re increases, high FSTI values still provide lower losses and the FSTI effect diminishes until it becomes almost negligible at Re = 300000, where losses for both cases are similar. Indeed, Fig. 6.8 shows that high FSTI is less influenced by the Re variation. As it can be seen from the figure, the lower FSTI case presents a loss variation of about 60% while the higher one presents a 50% variation from the highest to the lowest Re number tested.

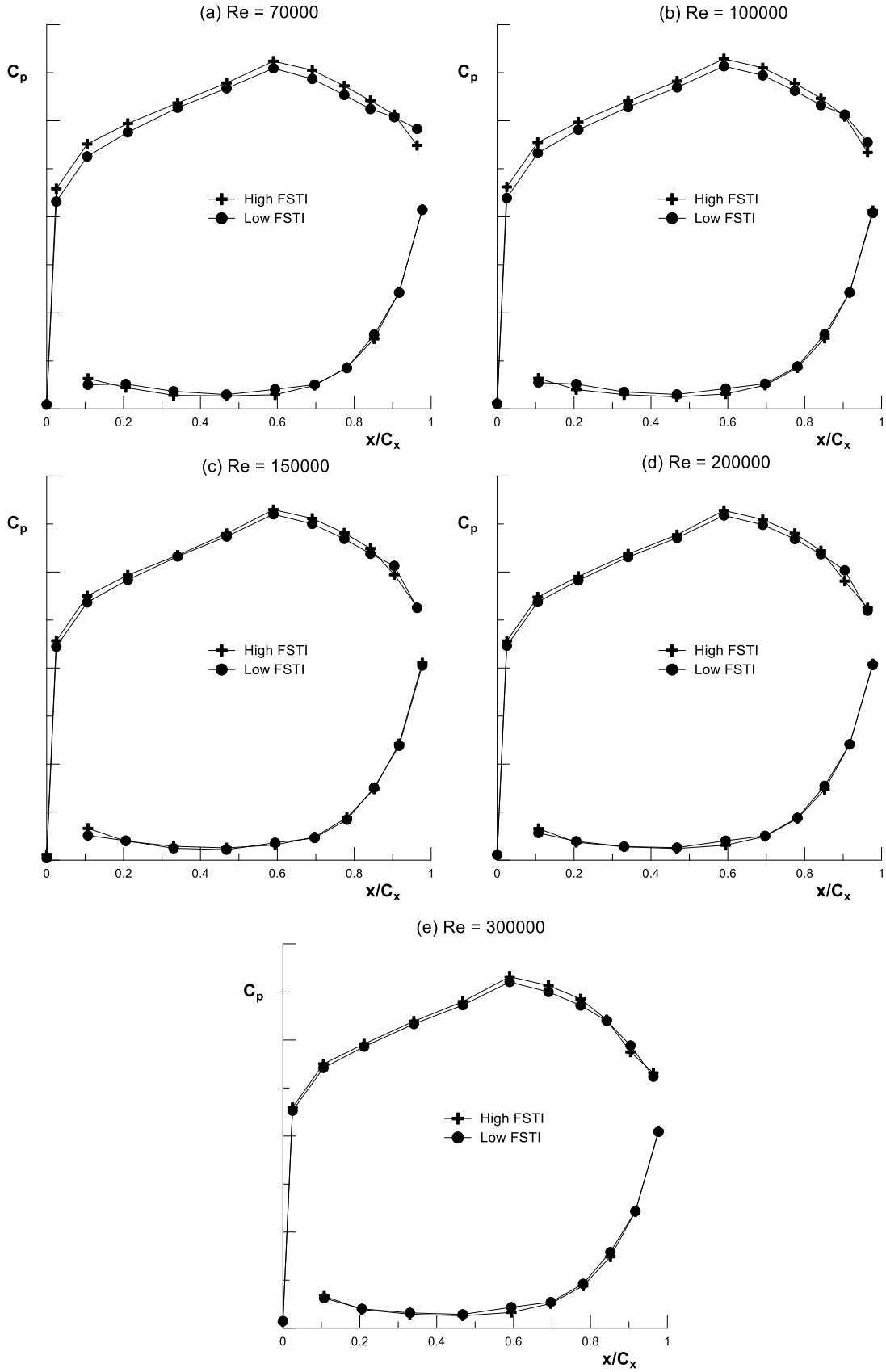

Fig. 6.7 Aerodynamic loading distribution in the steady inflow conditions of the reference cascade for different FSTI values

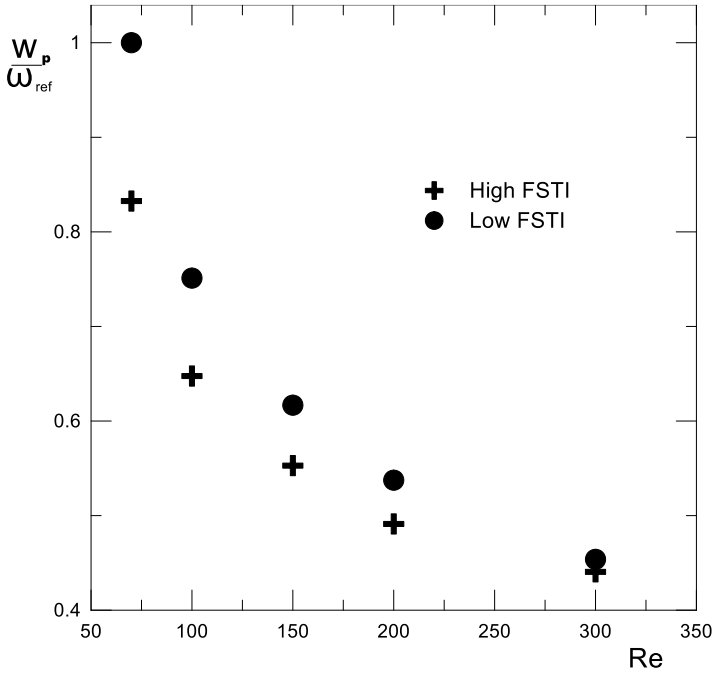

Fig. 6.8 Reynolds lapse rate for the two values of FSTI tested under steady inflow conditions

b) Unsteady inflow conditions

The incoming wakes introduced within the cascade completely suppress the bubble shown for the steady case in Fig. 6.7. Indeed, in this case, the disturbances introduced within the separated shear layer have excited the boundary layer enhancing its reattachment. Therefore, no separated bubble has been observed on the vane rear part. Hence, the vane aerodynamic loadings for both FSTI values at each Re number are practically superimposed, as shown in Fig. 6.9.

A quantitative analysis of the effects of FSTI on losses under unsteady inflow conditions is summarized in Fig. 6.10, where the plotted loss values have been adimensionalized by the condition at low FSTI and Re = 70000. In this figure, the reader can clearly note an almost superposition between the two curves making the loss independent from FSTI in the unsteady case, since they are mainly driven by the wake advection into the cascade passage. Additionally, the sensitivity to Re number variation is evidently smaller than the steady case plotted in Fig. 6.8. Indeed, both curves present a variation of about 10% in the whole Re range investigated.

Results reported in the following subsections and sections are related to the FSTI case equal to 4 %.

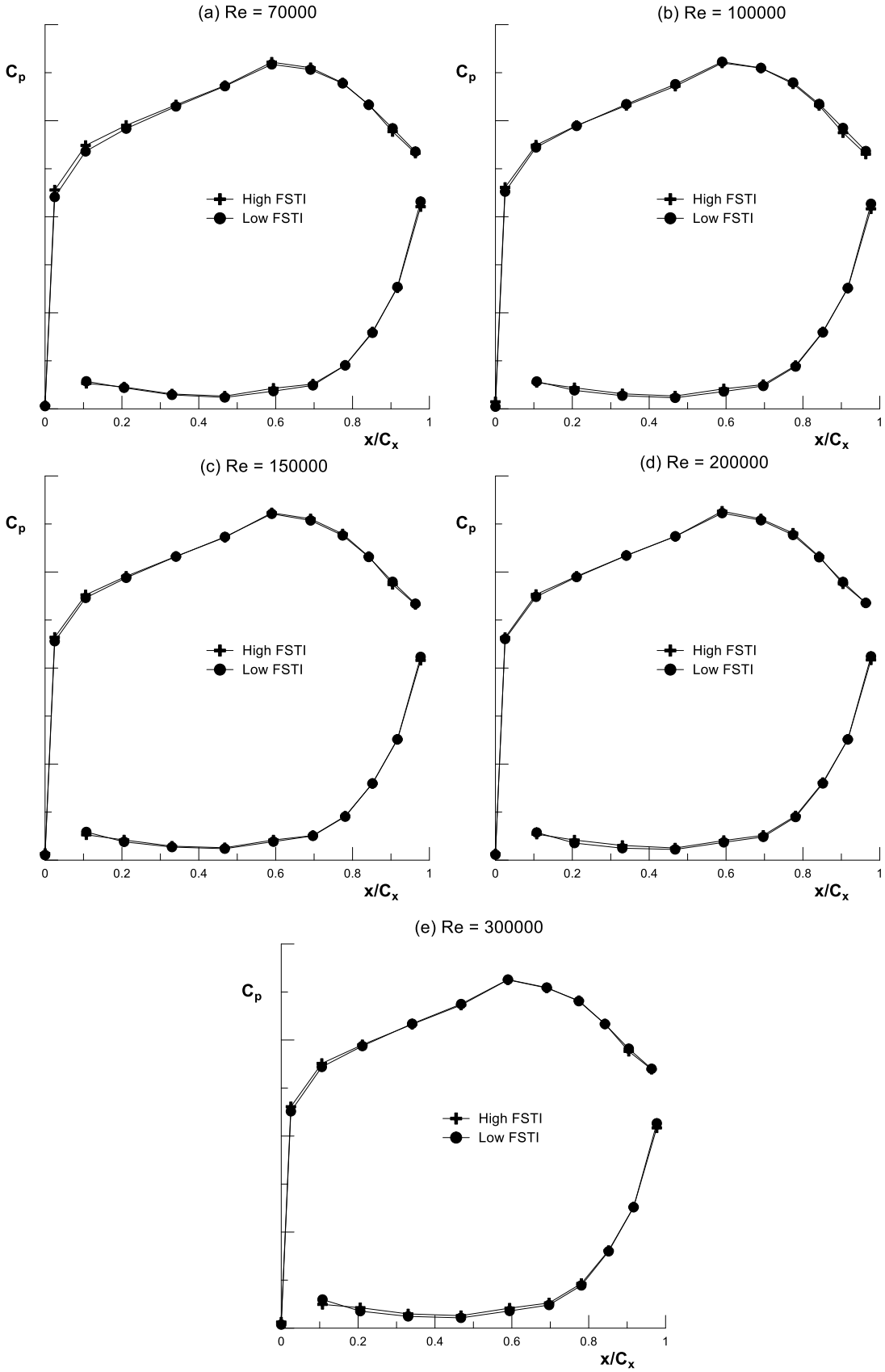

Fig. 6.9 Aerodynamic loading distribution in the unsteady inflow conditions of the reference cascade for different FSTI values

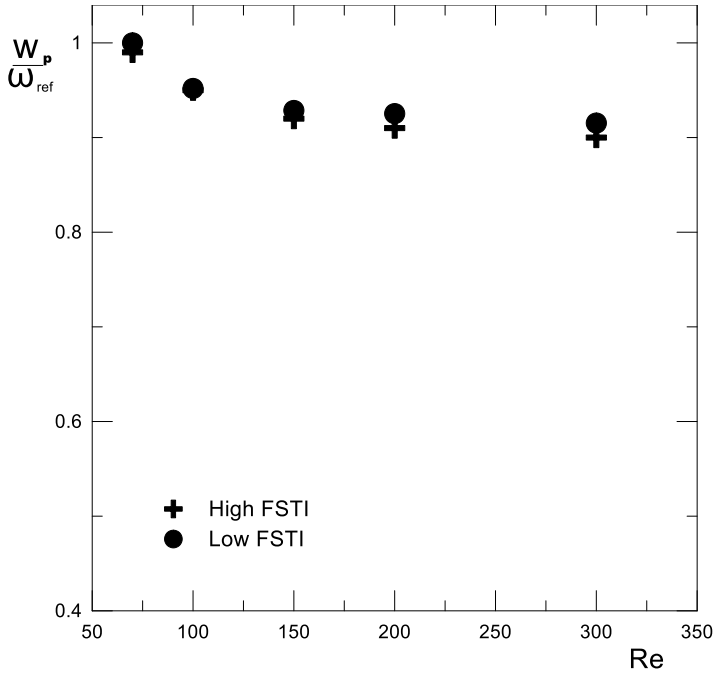

Fig. 6.10 Reynolds lapse rate for the two values of FSTI tested in the unsteady inflow conditions

6.3.3 Reynolds effect

a) Vane loading

To better appreciate the effects due to the Reynolds number variation at fixed FSTI level, the vane loading distributions of the reference cascade (cascade 1) at the nominal incidence flow angle are plotted in Fig. 6.11 for both steady and unsteady inflow conditions. Fig. 6.11(a) shows the loading distribution varying Re in the steady case while Fig. 6.11(b) shows the static pressure distribution for both steady and unsteady cases for the extreme values of the flow Reynolds number investigated in the present work (70000 and 30000). It should be emphasized that the similar incidence flow angle in both steady and unsteady conditions has been obtained through a pre-rotation of the test section of about 3 ° in the unsteady case. In fact, as already explained in detail in chapter 3, the use of a bar wheel in order to simulate the wake shedding phenomenon introduces a reduction of the incidence flow angle upstream of the cascade due to the low velocities characterizing the incoming wake. This effect is not present in a real engine and it needs to be compensated in order to obtain the right flow angle value upstream of the cascade. This has been done through the pre-rotation of the test section of an angle obtained from eq. 3.9.

From Fig. 6.11(a), it can be observed a separated bubble on the diffusive part of the suction side for the lowest Re investigated, which persists until Re reaches 100000 and then disappears completely. Indeed, as Re increases, the shear layer thickness diminishes with a consequent alteration of the boundary layer evolution and its stability properties, as shown experimentally by [87]. Interestingly, for the lowest Reynolds numbers, i.e., 70000 and 100000, the inflow condition does not allow a complete flow reattachment at the vane trailing edge. For the unsteady case the disturbances introduced by upstream wake are sufficient to avoid the boundary layer separation also for the smallest Re number tested, as make evident by the almost complete superposition of the vane loading in the unsteady case

with the case measured at Re equal to 300000 in the steady, unseparated condition (see Fig. 6.11(b)).

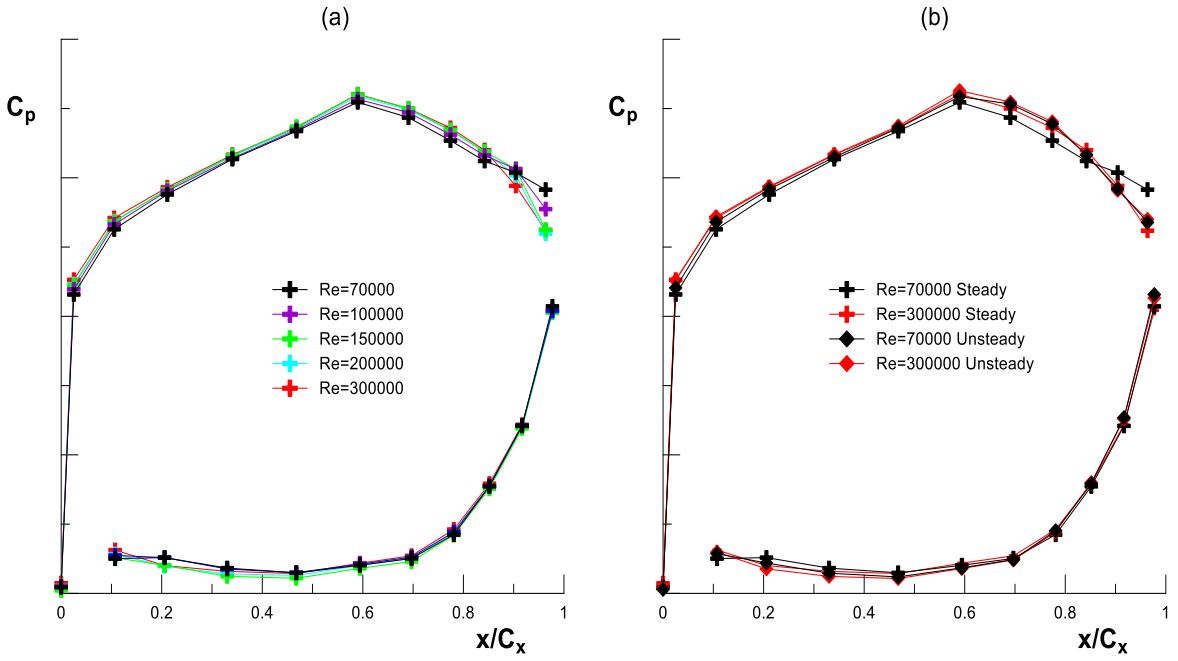

Fig. 6.11 Aerodynamic loading of the reference cascade at i = 0 ° (a) under steady inflow conditions and (b) under both steady and unsteady inflow conditions at Re = 70000 and Re = 300000

b) Downstream total pressure field

The distributions of the total pressure distribution coefficient obtained by means of Kiel probes under both steady and unsteady inflow conditions are reported in Fig. 6.12. The abscissa reports the non-dimensional pitchwise direction. The left branch of the plot corresponds to the pressure side of the vane wake, while the suction side is on the right with respect to the loss peak. This plot organization has been used in the whole chapter to present downstream total pressure distributions.

The steady case shown in Fig. 6.12(a) presents curves superimposed in the potential flow region represented by the asymptotic value outside the bell-like shaped part of the wake. Indeed, losses associated with the advection of the homogeneous turbulence across the vane passage depends marginally on Re and in this case, induce around 0.2-0.3 % of losses (only for the lowest Re case higher contribution to losses can be observed in the Cpt distribution in the potential flow region). Furthermore, the case Re = 300000 presents a symmetrical behavior with respect to its wake peak loss position due to the high mixing between the background turbulence and the main flow prior to the downstream measuring traverse. As Re decreases an increase of both width and peak losses as well as a peak shift towards the suction side region is observed due to both the separated bubble observed in Fig. 6.11(a) and an intense viscous effect on the vane sides which induce a boundary layer thickening. Note that this boundary layer thickening is greater on the suction side confirming that the flow evolution on both sides of the vane is different.

Under the unsteady inflow conditions, the vane wake has a strongly asymmetrical trend with a much greater extension of the region associated to the vane suction side. Indeed, the

unstable low-momentum region of the wakes shed from the upstream moving bar system tends to be distorted and transported by the cross-pressure gradient once entering the vane passage, inducing the well-known negative jet structure introduced in chapter 2. This jet is pushed toward the suction side with a consequent wake-boundary layer interaction process, while on the pressure side, this effect is not present. This induces the asymmetry of the total pressure distribution observed in Fig. 6.12(b).

For each Re, comparison between both plots (a) and (b) of Fig. 6.12 shows that the unsteady case presents vane wake thicker and larger, which is expected to provide higher losses. As shown in subsection 2.1.3, it is a consequence of the vane boundary layer excitation by the turbulence contained within the incoming wakes which leads to an anticipated boundary layer transition and hence, a more extended turbulent region over the suction side of the vane. However, the reader can note that the wake width increase between the steady and the unsteady conditions is greater for high Re values than for lower ones. In fact, at lower Re values the suction side experiences the presence of separation bubble in the steady case (see Fig. 6.11), thus the incoming wakes introduce beneficial effects on the cascade aerodynamics since they reduce the losses associated to the bubble. ~~On the other hand, as it can be seen, incoming wakes tend to rise the losses due to an increase of turbulent wetted surface with respect to the steady inflow condition.~~

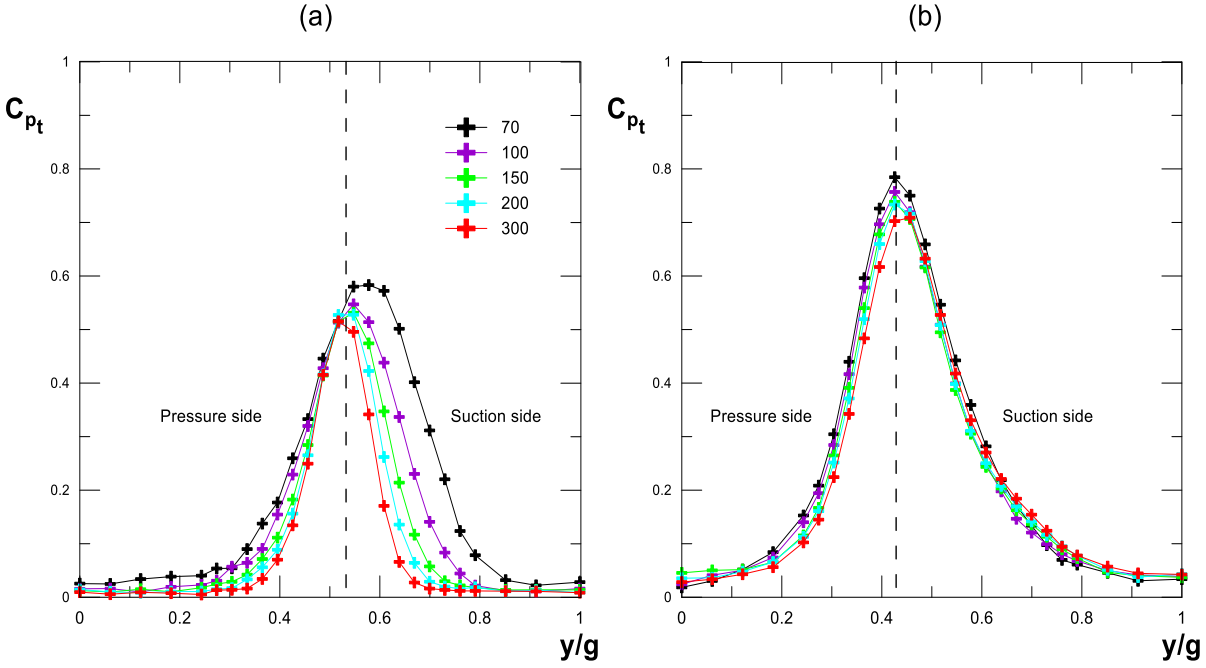

Fig. 6.12 Downstream total pressure distribution under (a) steady inflow conditions and (b) unsteady inflow conditions

A quantitative analysis of the Reynolds lapse rate under both steady and unsteady inflows is provided in the following by analyzing the overall loss coefficient ω_p, defined in eq. 4.1.

c) Overall losses

The overall loss coefficient made dimensionless by the loss coefficient in the unsteady case at Re = 70000 is shown as a function of Re in Fig. 6.13, for both steady and unsteady inflow

conditions to better emphasize the effects due to upstream unsteadiness. The fact that unsteady conditions present higher losses than the steady ones is confirmed, as a consequence of an early intermittent transition induced by the turbulence carried by the upstream wakes leading to a net increase of the vane region wetted by the turbulent boundary layer.

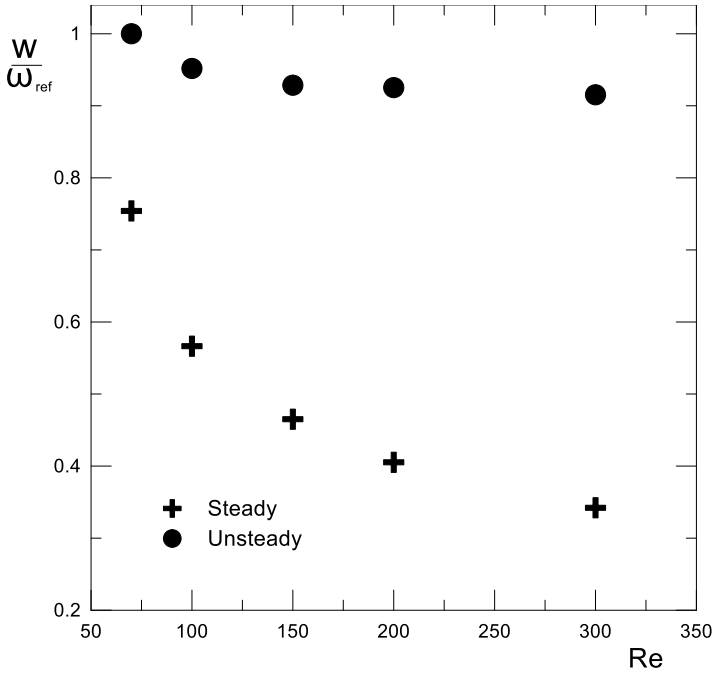

Fig. 6.13 Overall losses for both Steady and unsteady inflow conditions

As it can be seen, the loss coefficient increases as Re decreases for both steady and unsteady conditions, due to a boundary layer thickening and consequent major viscous losses and high blockage effects. However, the steady case is more affected by Re variation than the unsteady one as it can be confirmed by the different slopes of the two curves. Indeed, in the range of Re values investigated, the loss coefficient under steady inflow conditions shows a variation of about 50% while under unsteady inflow conditions, it shows a variation of about 8%.

6.3.4 Incidence flow angle effect

a) Vane loading

The incidence flow angle effect on vane loading for the unsteady case is shown in Fig. 6.14, where the static pressure coefficient at Re = 70000 and Re = 300000 is provided. For both plots, as the incidence flow angle increases the vane loading increases due to the higher deflection angle that the vane should apply on the flow. It can be observed how the main effect of the flow angle variation is confined in the front part of the suction side, from the leading edge up the velocity peak position.

It is well known that as the incidence increases, the stagnation point migrates from the suction side to the pressure one in the leading-edge region. Hence, a larger portion of the leading edge becomes a part of the suction surface. This results in highly curved streamlines in the leading-edge region with overspeed, followed by a short length of strong adverse pressure gradient and possibly the presence of separation bubbles. This situation is clearly

visible for the highest values of incidence ($i = 9°$ and $i = 6°$), and in this case the streamlines are no longer able to follow the leading edge designed for the nominal flow conditions.

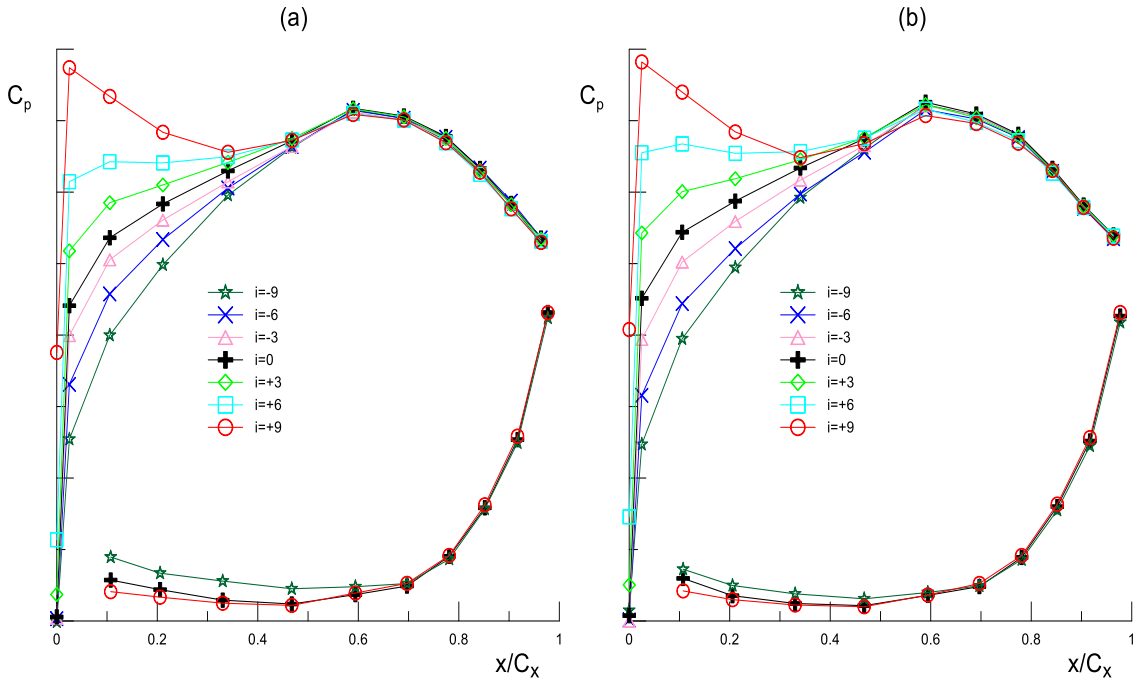

Fig. 6.14: Aerodynamic loadings in off-design conditions for (a) Re = 70000 and (b) Re = 300000

On the pressure side characterized by lower velocities, the curves are practically superimposed making the static pressure distribution on this side unreceptive to the flow incidence variation. However, a more pronounced (spatially extended) increase of Cp values in the pressure side at the maximum negative incidence condition, that may suggest a pressure side separation.

b) Downstream total pressure field

The downstream total pressure field measured varying the incidence flow angle is shown in Fig. 6.15 for the lowest (on the left) and the highest (on the right) Reynolds number tested. Curves are essentially superimposed in both the potential and the pressure side regions for both Reynolds number, making the losses unaltered and not influenced by the incidence angle variation in these regions.

The main difference between each plot of the figure is on the suction side region, where occurs the interaction between the wakes shed from the upstream rotor and the vane boundary layer. It can be observed that increasing the incidence angle leads to an increase of both width and peak wake as well as a peak shift toward the vane suction side. This can be attributed to the fact that higher incidence angle leads to higher cross-pressure gradient as shown previously in Fig. 6.14, and hence, to major viscous effects on the vane sides. Furthermore, for negative angles the wake width slightly decreases while for positive values, the increase is more consistent.

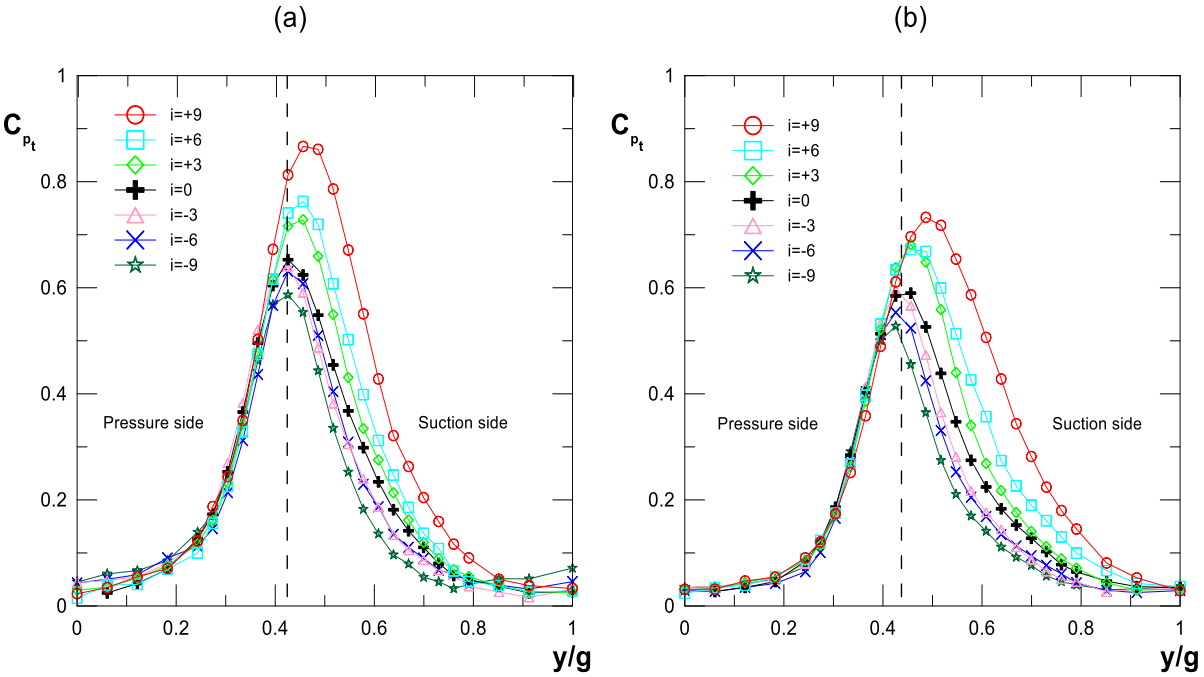

Fig. 6.15: Downstream total pressure for (a) Re = 70000 and (b) Re = 300000

c) Overall losses

Also in this case, the incidence angle effect on losses have been quantified through the loss coefficient ω_p adimensionalized by the same reference value used in the previous section. Results are summarized in Fig. 6.16 where the loss coefficient is shown as a function of the incidence angle, with Re as parameter. The reader can note that the Re curves have the same tendency, i.e., for both Re loss increases with the incidence angle. This is just a confirmation of what observed earlier viz. as the incidence angle increases wake width becomes larger due to an intense wake-boundary layer interaction, which leads to higher turbulent losses. The reader can further observe an offset between the Re curves which depends on the incidence angle. Indeed, it tends to diminish as the incidence angle increases, making the loss coefficient less influenced by the incidence angle at lower Re.

The effects on losses of both Reynolds number and incidence flow angle shown earlier for the cascade 1 have been also found for the other two cascades investigated in the present work. Therefore, there is no interest in presenting those results since they provide no additional information. Nevertheless, in the following subsection, partial results of these cascades are shown in order to provide the effects due to solidity variation on losses under both steady and unsteady inflow conditions while varying Re.

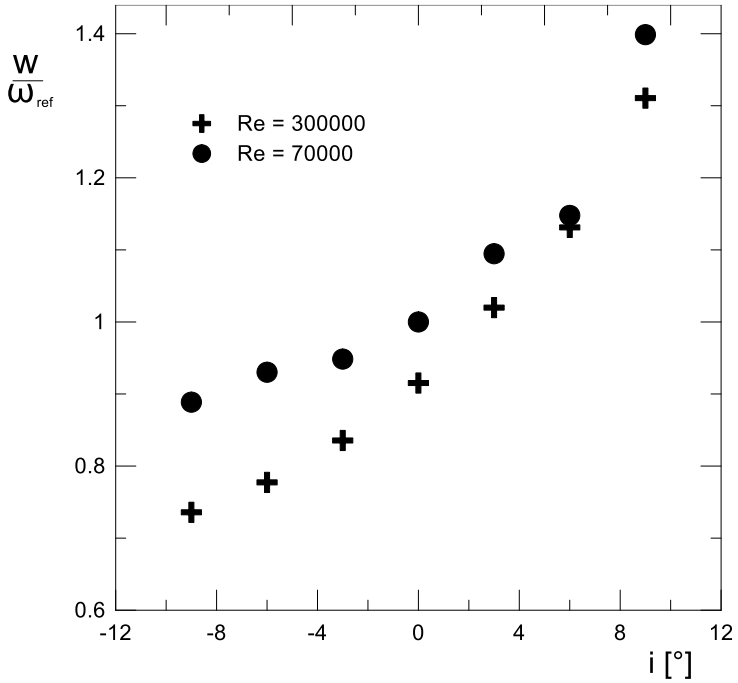

Fig. 6.16: Off-design overall losses

6.3.5 Solidity effect

a) Steady inflow conditions

The vane loadings of the three cascades investigated in the present work are shown in Fig. 6.17 under steady inflow conditions at Re = 70000 in plot (a) and Re=300000 in plot (b). They both evidence how a decrease of vane solidity (increase of the pitch-to-chord ratio) while maintaining the remaining design parameters leads to higher aerodynamic loads. The cascade loadings have practically the same form and the same peak velocity position, at about 60% of the axial chord. Fig. 6.17(a) shows for all the cascades a separated flow in the rear part of the suction side due to the low Re number under observation. Furthermore, as the vane loading increases, the bubble covers a more extended region over the suction side as a consequence of the strongest diffusion in this region, as well documented in literature [6]. Moreover, both cascades 2 and 3 present a bubble reattachment at the blade trailing edge (see the plateau in the pressure distribution, followed by a quick recovery of the loading toward the blade trailing edge), while cascade 1 presents an open bubble as previously discussed. On the pressure side, the curves are practically superimposed.

As Re increases only the rear part of the vane suction side is affected. Indeed, Re significantly influences the separation bubble leading to the bubble suppression under certain circumstances. Fig. 6.17(b) confirms the capability of higher Re to entirely suppress the bubble (the plateau in the pressure distribution are no more visible) also at low solidity.

Downstream total pressure fields of the cases previously shown are summarized in Fig. 6.18. It can be noted how the curves are practically superimposed in the potential flow region outside the wake for both Re, making the losses due to the flow turbulence advection independent from both vane solidity and flow Reynolds number. However, only for cascade 1 at the lowest Re case (Fig. 6.18(a)) higher contribution to losses can be observed in the potential flow region, probably due to the large bubble shown in Fig. 6.17(a) which

introduces blockage effects at the trailing edge plane and therefore, influences the flow evolution outside the wake region.

At Re = 70000, as cascade solidity increases wake peak magnitude decreases while a clear tendency of the solidity effect on wake width cannot be easily deduced probably due to a different and chaotic mixing between the vane wake and the freestream prior to the downstream measuring traverse (see Fig. 6.18(a)). Increasing Re cascade 2 presents the highest wake peak (see Fig. 6.18(b)) and vane width seems to not change with the solidity variation.

Fig. 6.19 summarizes the Reynolds lapse rate under steady inflow conditions of the three cascades under investigation. The reader can note that cascades 1 and 3 present a constant offset within the whole Re range investigated, with cascade 3 that presents higher losses when compared to cascade 1: at low Re it is due to the larger bubble shown earlier in Fig. 6.17 while at high Re, it is a consequence of the boundary thickening introduced by the increase of the pitch-to-chord ratio.

The benefit of cascade 2 depends on Re; indeed, at Re = 70000 it shows the lowest losses. The situation begins to change from Re = 100 000 where both cascades 2 and 3 present the same loss trend, probably due to the fact that streamlines are not able to follow their designed path within the cascade, leading to a major turbulent wetted area over the vane sides. This is the first evidence that the relationship between loss and pitch-to-chord ratio (solidity) is not monotonous. Furthermore, cascade 2 presents losses which are less influenced by the Reynolds number variation than the other cascades.

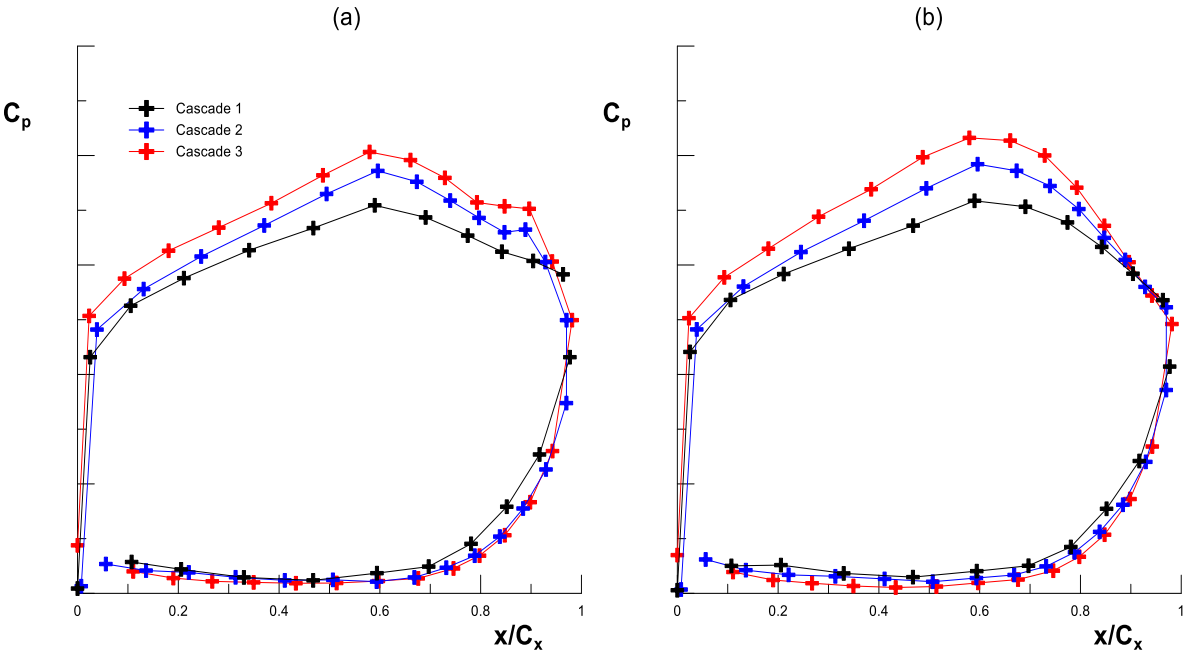

Fig. 6.17 Cascade loadings for the steady case (a) Re =70000 and (b) Re=300000

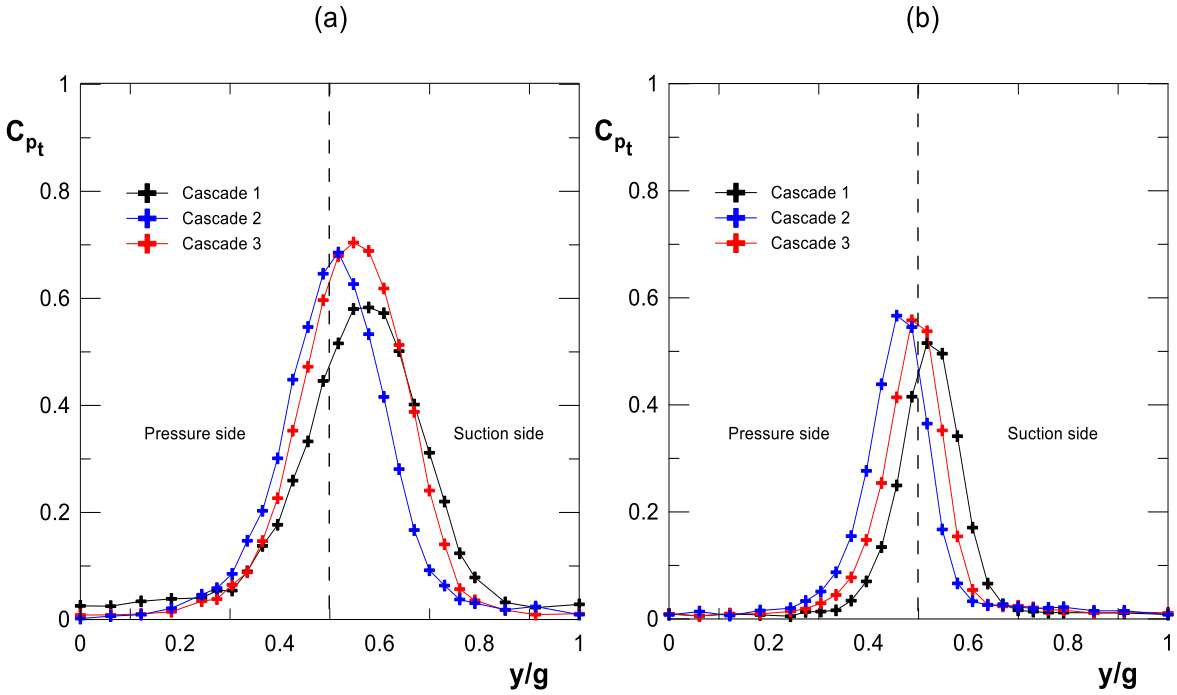

Fig. 6.18 Total pressure distributions for the steady case (a) Re =70000 and (b) Re=300000

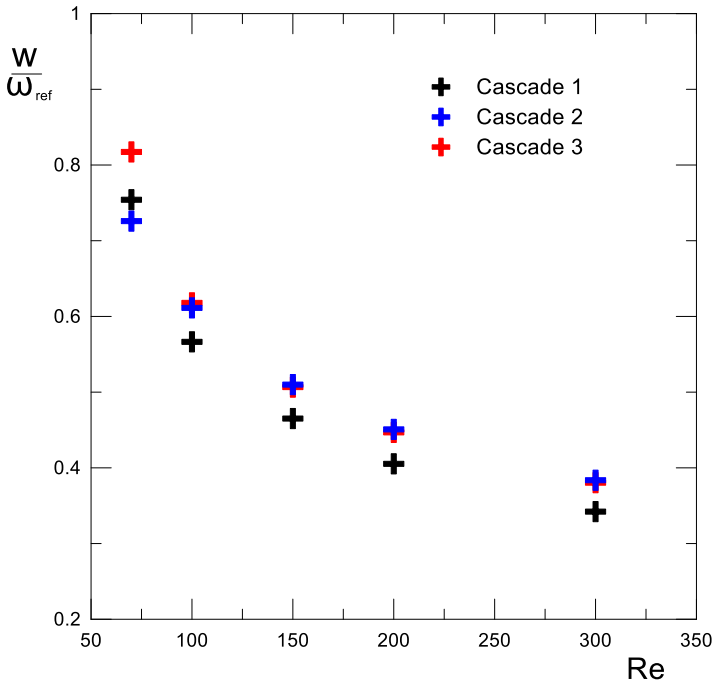

Fig. 6.19 Overall losses for the steady case

b) Unsteady inflow conditions

Fig. 6.20(a) confirms results largely exposed in literature, i.e., wakes shed from the upstream rotor with an opportune frequency can entirely suppress the bubble visible in the steady case. In fact, as exposed previously in chapter 2, the turbulence carried by the wake interacts with

the boundary layer in the aft portion of the suction side enhancing the formation of the streaky structures with consequent excitation of the boundary layer leading to the bubble suppression. This situation is observed for both cascades 1 and 2. Cascade 3 instead still presents a slight curve deviation, indicative of a non-complete bubble suppression since in the steady case, a larger bubble characterized this cascade. Therefore, the reduced frequency value tested ($f^+ = 0.69$) is not able to completely suppress this bubble. As Re increases, no cascade shows the separation phenomenon even at the higher load (see Fig. 6.20(b)). Once again, the static pressure distributions on the vane pressure side are not influenced by the variation of both solidity and Re number.

Concerning the downstream total pressure field shown in Fig. 6.21, it can be seen how for both Re tested losses in the potential flow region outside the wake do not depend on the cascade solidity variation. Discrepancy shown by cascade 2 in Fig. 6.21(a) may be attributed to measurement uncertainty. Moreover, for both Re cascade 2 presents the highest wake peak while the vane wake width seems to be marginally influenced by the solidity variation.

In order to quantify the pitch-to-chord ratio effect under unsteady incoming flows, overall losses are reported in Fig. 6.22. Also in this unsteady case, there is a constant offset between both cascades 1 and 3. Fig. 6.22 shows that cascade 2 presents the lower losses for each Re investigated. This is a consequence of the optimal flow guidance within this cascade which leads to a minor turbulent wetted area over the vane sides, avoiding in the meanwhile flow separation. Indeed, as the cascade pitch decreases the flow guidance within the cascade improves and at the same time there are more friction losses between the flow and the vane surfaces. On the other hand, higher values of cascade pitch provide a poor flow guidance and small losses, even if these cascades are characterized sometimes by a flow separation over their suction side. Thus, it exists an intermediate cascade pitch value which optimizes the flow guidance and the losses due to eventual separation (cascade 2 in the present case). However, at the lowest Re value both cascades 1 and 2 present similar losses.

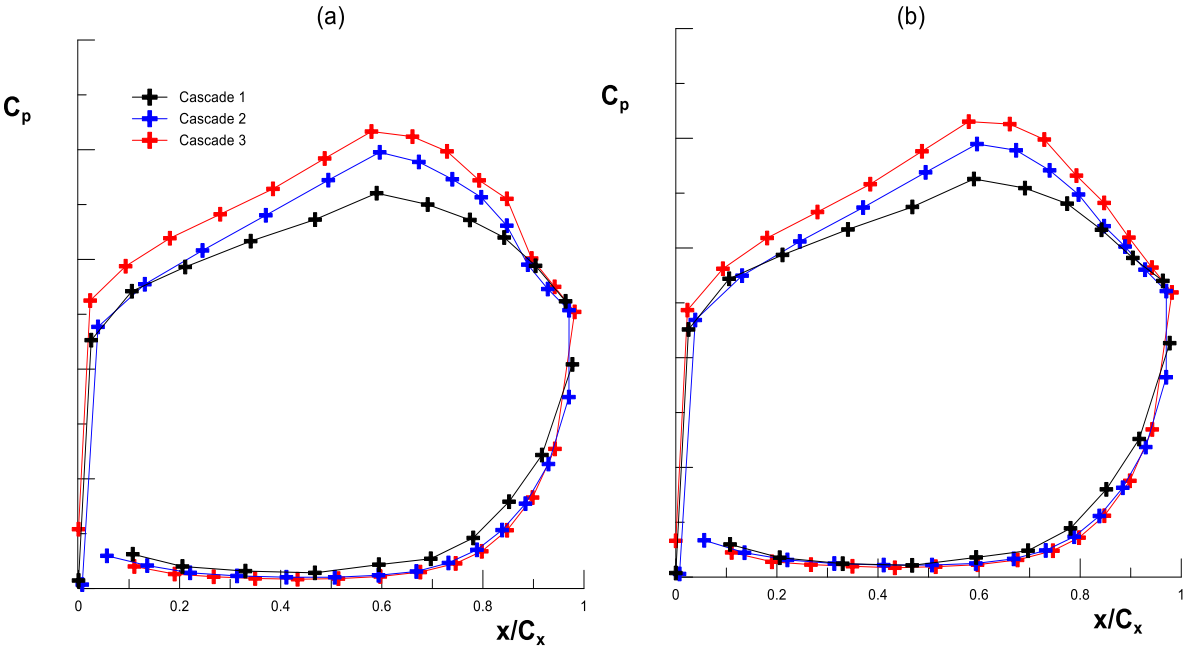

Fig. 6.20 Cascade loadings for the unsteady case at $f^+ = 0.69$ (a) Re =70000 and (b) Re=300000

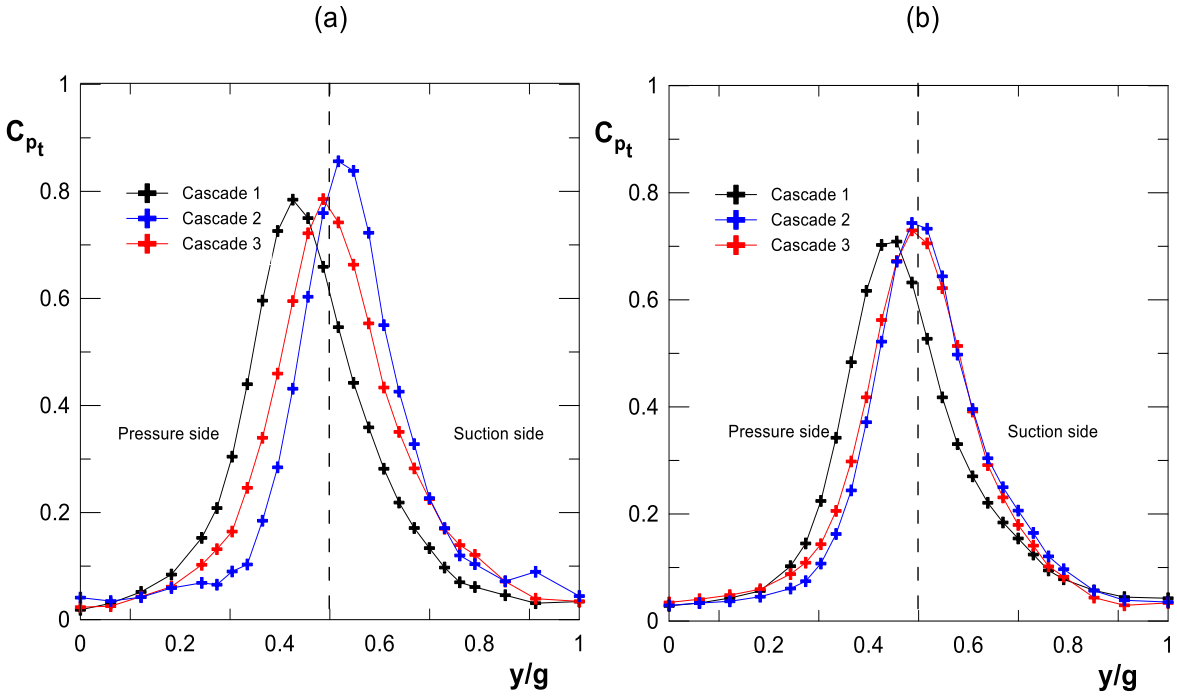

Fig. 6.21 Total pressure distributions for the unsteady case at $f^+ = 0.69$ (a) Re =70000 and (b) Re=300000

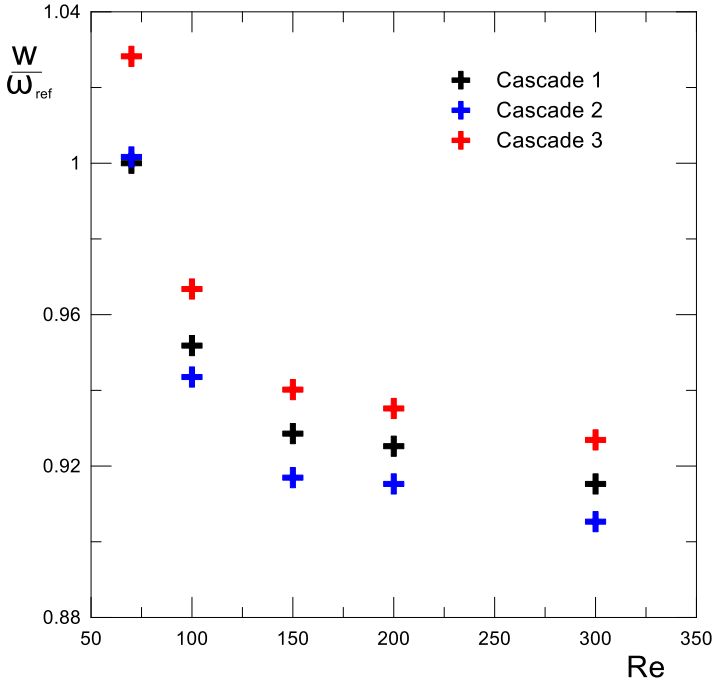

Fig. 6.22 Overall losses for the unsteady case at $f^+ = 0.69$

A more realistic investigation has been further conducted in order to check if cascade 2 would still provide lower losses once installed in a real engine with typical bar to cascade

pitch ratio values (about 1.5). In this case, bar count of the moving bar system has been changed prior to acquire data on each cascade. Specifically, for cascade 1 a moving bar system of 30 bars has been used while for cascade 3, 25 bars have been employed. Concerning cascade 2, a decimal number of bars (26.27) has been found during calculations in order to obtain the desired bar to cascade pitch ratio value. Therefore, data for this cascade have been acquired for 30 and 25 bars and a further interpolation has been done. Results are summarized in Fig. 2.23 where once again, cascade 2 provides lower losses in the whole Re range investigated, except for Re = 70000 where it provides the same loss as cascade1.

This analysis confirms how an increase in vane loadings of 12% leads to lower losses especially at Reynolds numbers characteristic of take-off phases, avoiding over losses at Low Reynolds number typical of the cruise condition. This leads to a substantial cost saving through a reduction in the number of parts required for the LPT module and in the engine weight can be achieved.

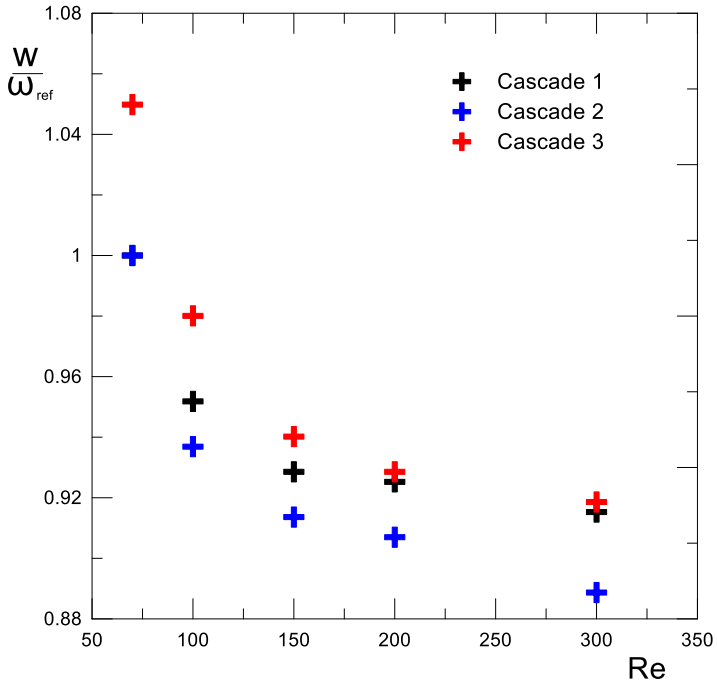

Fig. 6.23 Overall losses under unsteady case

6.3.6 Incoming wake related effects

Once characterized the unsteady incoming flow entering the cascade (see section 6.2), the losses generated by the wake migration and by its interaction with the vane suction side have been estimated for each condition tested. In Fig. 6.24(a) the total pressure loss coefficient distributions measured at the highest and the lowest reduced frequencies, for the largest and smallest bar diameters, are reported for the low axial gap condition. Both reduced frequency and bar diameter alter significantly the loss distribution observed downstream of the cascade. The main differences between the plots of Fig. 6.24(a) are observed on the suction side of the wake, since in this flow region losses are due to the incoming wake-suction side boundary layer interaction process, as well documented in the literature [6]. The pressure side of the

wake is instead practically unaffected by the parameter variation. Interestingly, a sensitivity to the parameter variation is also observable in the loss level due to wake migration into the potential flow region (see [72] for instance). Specifically, black curves exhibit a smaller level of losses outside the profile wake region, with a level slightly dependent on the bar diameter. The blue curves are instead characterized by higher values, even though also in this case the bar diameter seems to play a minor role. Thus, Fig. 6.24(a) shows that interaction between suction side boundary layer and incoming wakes is significantly affected by both bar diameter and reduced frequency, while losses in the potential flow region appear more sensitive to the reduced frequency, even though also the bar diameter play a role. Data characterizing the higher axial gap case are shown in Fig. 6.24(b). Generally, these plots present the same tendency of the loss distribution to the reduced frequency and bar diameter variation: both bar diameter and reduced frequency affect the loss generated as a consequence of the suction side boundary layer – incoming wake interaction, while losses in the potential flow region are mostly affected by the reduced frequency.

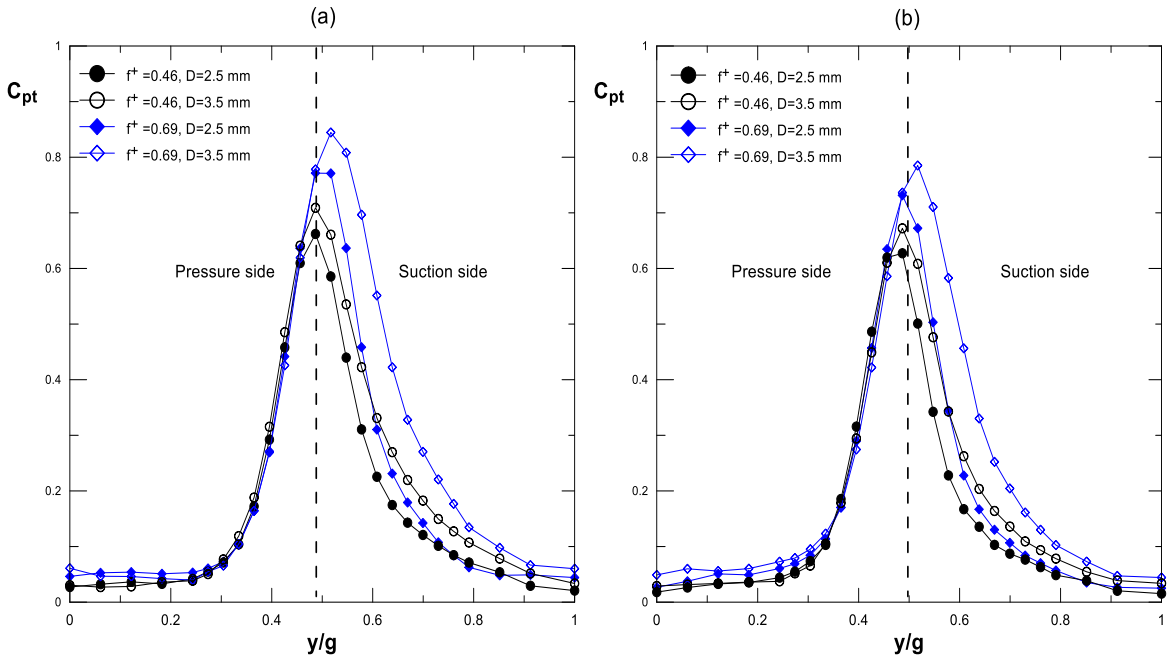

Fig. 6.24 Total pressure loss coefficient distributions for (a) the lower axial gap and (b) the higher axial gap

In order to give a quantitative analysis of the losses due to parameter variations, Figs. 6.25(a) reports the overall profile losses ω_p as a function of the incoming wake reduced frequency, for the three different bar diameters tested at low axial gap. The corresponding distributions for the high gap condition are reported in Fig. 6.25(b). Data of both plots have been made dimensionless by the condition at f^+=0.575, D=3 mm at low axial gap.

Data reported in these plots confirm what was anticipated from total pressure loss coefficient distributions. Basically, losses increase for both gaps when either bar diameter and/or reduced frequency increase. This is mainly due to the major disturbances introduced by incoming wakes into the suction side boundary layer, even though also losses into the potential flow region have been found to be not negligible, and variation due to reduced

frequency is larger than 15% for the smallest bar diameter tested, and it becomes of the order of 30% for the largest diameter (red curves). The effects due to the diameter variation at fixed f^+ is always greater than 15%, with the largest effects at high f^+ condition. Comparison of data at high and low gap makes evident that at fixed design space condition, high gap losses are smaller than low gap ones (of more than 10%) since incoming wakes are more diffused prior to enter in the downstream cascade, thus reducing the overall amount of unsteady losses during interaction with the downstream cascade. Interestingly, the sensitivity to loss variation due to reduced frequency (the inclination of the curves into the diagram) is poorly affected by the bar diameters for both axial gap condition.

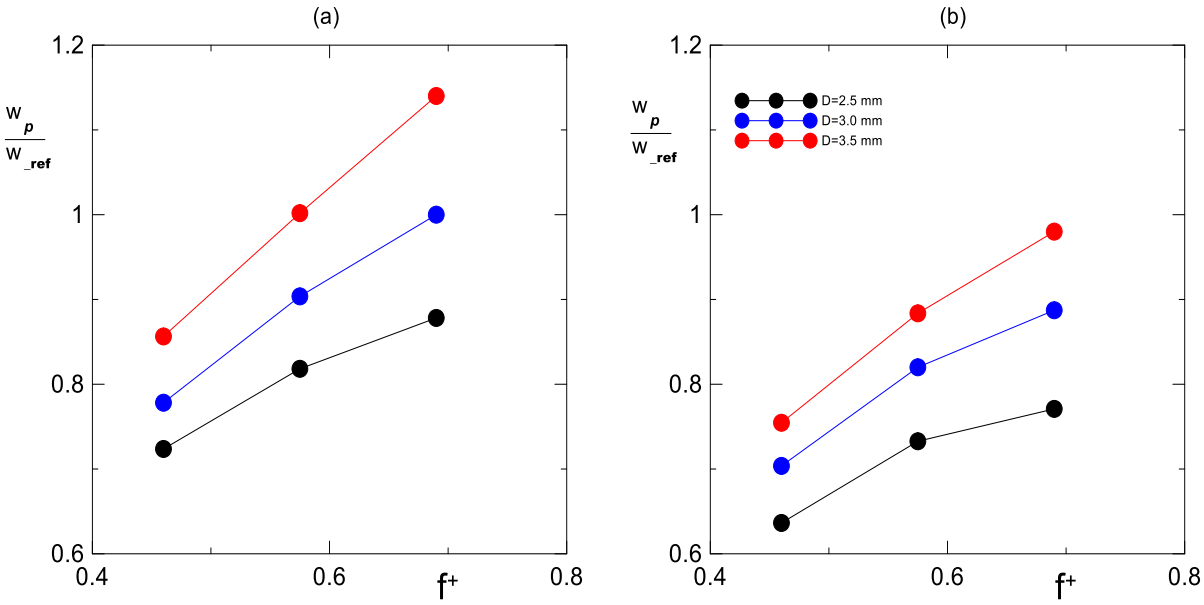

Fig. 6.25 Effects of reduced frequency and bar diameters on losses at (a) low axial gap and (b) high axial gap.

The loss maps shown in this section give an overall view to LPT designers of the expected loss sensitivity to the most influencing parameters governing the operation of a turbine cascade. Their trends appear extremely dispersed in physical space since losses are affected by each parameter tested. Thus, it seems necessary to find another space aiming to analyze acquired data from another perspective and to find a way to reduce the problem dimension.

6.4 Losses in POD space

The total pressure distributions deriving from the previous results obtained during the incoming wake characterization (see subsection 6.3.6) have been arranged according to eq. 5.18 in order to construct the snapshot matrix and apply POD. In this specific case, the loss distribution for the steady case has been used as the reference loss distribution of eq. 5.18. As already stated, once applied POD to a dataset made of total pressure loss distributions, a triplet of information is obtained through eqs. 5.15 -5.17. The eigenvalues λ provide the amplitude of each POD mode, and hence are useful to identify the number of modes

requested to well describe the loss distribution. The POD modes ϕ give the spatial distribution of the basis function describing the losses in the pitchwise direction, highlighting the spatial region where the loss coefficient is high. The eigenvectors χ instead are the only quantity case dependent and show the role played by each parameter in determining the overall losses; specifically, they give the amplification factor to be applied to the modes for each different combination of the design parameters (i.e., different combination of bar count, bar diameter and axial gap)

To make the concept clearer, in Fig. 6.26 the eigenvalues λ are reported: there are 18 independent real eigenvalues, being the cross-correlation matrix a real square symmetric matrix of dimension 18x18. The first mode contains more than 98% of the information, and the amplitude of the modes above the fourth becomes rapidly negligible (lower than 0.1%). This distribution suggests that only the first four modes can be used to represent the deviatoric part of the loss distribution, with an extremely compact representation as it will be further discussed in the following looking at the reduced order models of different ranks.

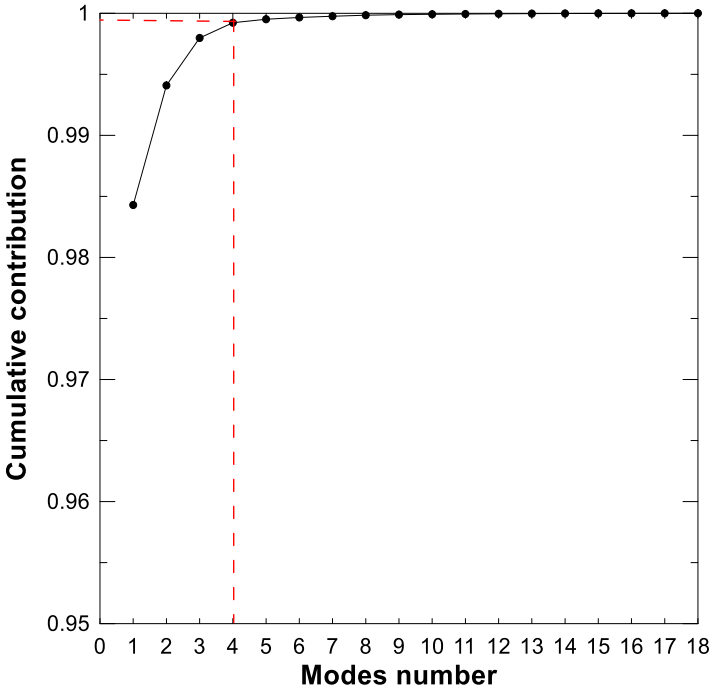

Fig. 6.26 Eigenvalues of POD modes

The pitchwise distributions of the first four POD modes ϕ(*y*) are shown in Fig. 6.27. The distribution of the first mode makes evident that the main variations of losses with respect to the reference steady case are in the potential flow region (the asymptotic value is far from being on the zero level), and in the vane wake suction side. This is nothing more than what observed in the previous figures but deduced looking only to a single plot. Mode 2 is significantly smaller than mode 1, and it represents a second order effect on the pressure side. The other modes are even smaller and do not significantly contribute to the overall behavior.

The POD eigenvectors χ reported in Fig. 6.28 describe the sensitivity of the loss coefficient to the parameter variation. According to eq. 5.20, they act as case dependent amplification factors of the POD modes just observed. Data in Fig. 6.28 can be also considered as the

response surface to the parameter variation. It is evident that the larger weight corresponds to the high reduced frequency with the larger diameter, at low gap. Moreover, the two-response surfaces refer to the high and low gap respectively, and since they are basically offset, this indicates that loss sensitivity to both reduced frequency and bar diameter is not dependent on the axial gap, as previously observed referring to Fig. 6.25. Hence, the POD space provides the same loss trend of the physical one and it can be compacted by a filtering operation on the number of POD modes in order to construct ROMs. In this specific case, four modes can be used to provide an optimal subspace since as shown in Fig. 6.23 they contain more than 99% of the information. Moreover, the surface response provided by the POD design coefficients shown in Fig. 6.28 appears extremely flat, thus allowing for a tuning of low order polynomial fitting function in the POD subspace. This makes the POD space attractive to educate models with only few tested conditions.

In the following, LSM will be adopted in the POD subspace to tune a smooth kernel aiming to describe the loss response to parameter variation with a limited number of tested conditions. The capability of the kernel in reproducing the loss trend will also provide evidence for the limited number of conditions that should be tested during measurements. However, prior to the model education, it is important to find out the number of independent tested conditions to be used. It is achieved through an inspection of the eigenvalues. Previously, it has been shown that four modes contain more than 99% of the information of the dataset under observation. Hence, four tested conditions are sufficient to reconstruct the whole dataset.

In order to better emphasize the ability of this POD procedure, the reconstruction of the original total pressure distribution has been computed using the following equation

$$C_{pt}{}^{k-order}(y) = C_{pt\_reference}(y) + \sum_{i=1}^{k} \sqrt{\lambda^{(i)}}\chi^{(i)}\phi^{(i)}(y) \qquad (6.1)$$

Fig. 6.29 describes reduced order models of different ranks (i.e., different k-values in the previous equation) compared to both the steady condition, and the full rank (i.e. not decomposed with POD, or equivalently with k=max) loss coefficient distributions for the conditions exhibiting highest and lowest overall loss (i.e. the cases D=3.5mm, f^{+}=0.69 at low gap, and D=2.5mm, f^{+}=0.46 at high gap, respectively). Data in Fig. 6.28 further strengthens the possibility to use four POD modes instead of eighteen. Indeed, for both conditions shown, the loss distribution into the wake region is really well captured by the first mode, while the contribution due to modes 2 - 4 is limited to the loss due to upstream wake migration into the potential flow region on the vane pressure side. The contributions due to higher order modes are not significant, since the fourth order reduced model is practically superposed to the full rank loss coefficient distribution. Thus, the rank of the problem at hand is 4 and from an engineering point of view, this means that within the whole dataset, only four conditions are really independent and the remaining ones do not add any further useful information. Therefore, a model can be educated by means of standard LSM within the POD subspace provided by four conditions to construct a smooth kernel aiming to predict the remaining tested conditions (that in reality should not be acquired in future perspective tests).

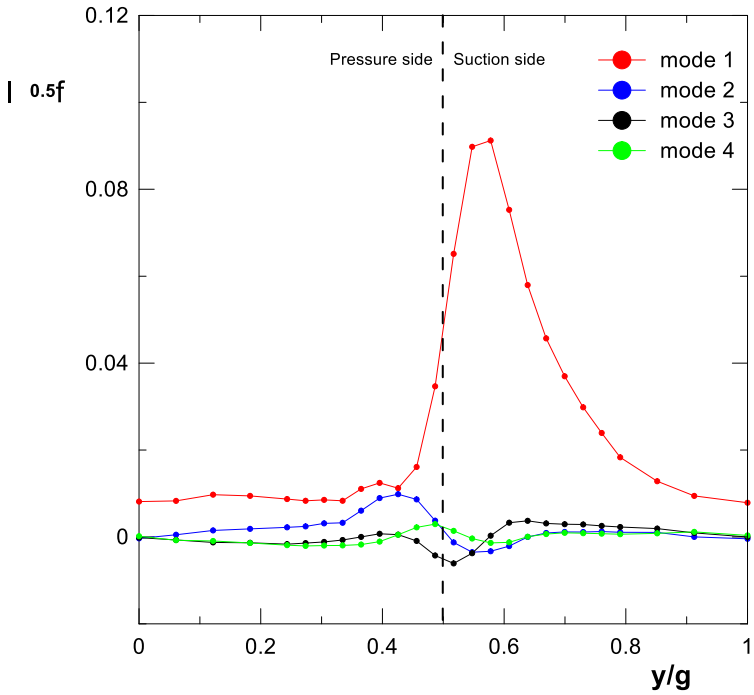

Fig. 6.27 Pitchwise distributions of the four first POD modes

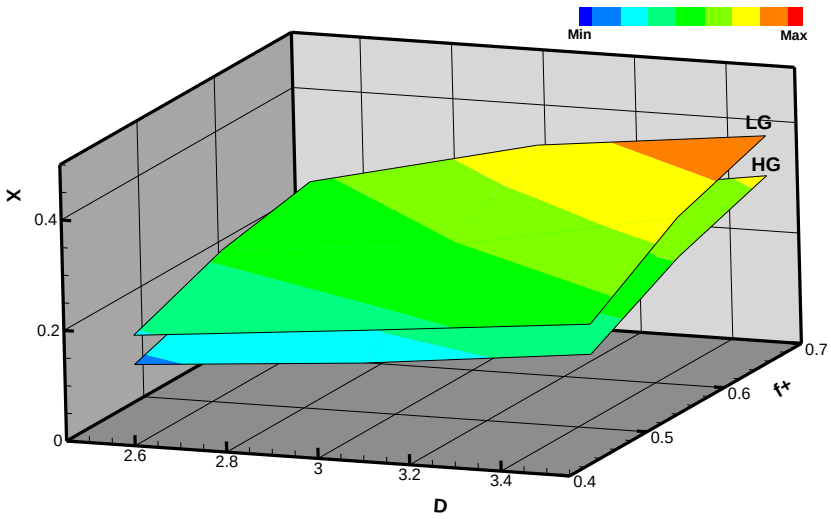

Fig. 6.28 POD eigenvectors (design space weight)

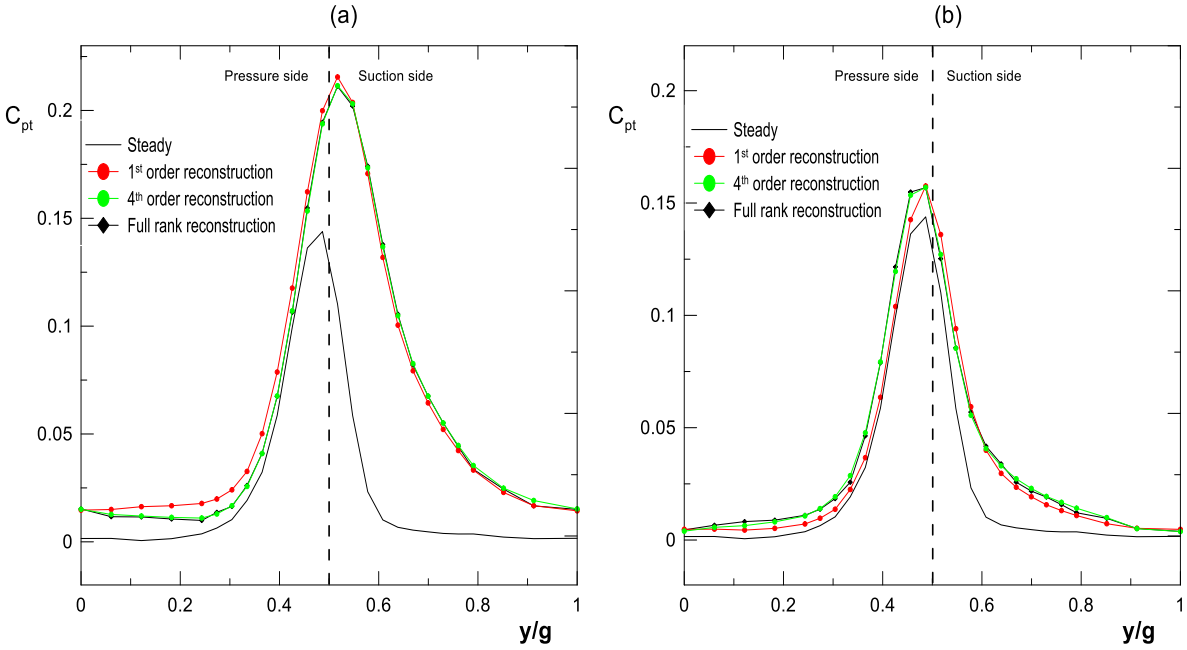

Fig. 6.29 Reduced order model representation of the loss coefficient (a) at low axial gap, D=3.5 mm and f^+=0.69 and (b) at high axial gap, D=2.5 mm and f^+=0.46

6.5 Smooth kernel

According to the previous observations, when applying POD to total loss distributions obtained in subsection 6.3.6, the reconstruction of the loss coefficient can be educated with only four tested conditions. Since the design space is a cube, the natural choice for the selection of the 4 points falls on the vertices of the cube. A random selection of the 4 points has been done and as it will be shown later, it does not influence the accuracy of the method. With these 4 tested conditions, a reduced data matrix has been used to define the POD design coefficients of the reduced model, thus for the education of the smooth kernel χ_{red} according to

$$\chi_{red} = \beta \boldsymbol{X} \tag{6.2}$$

Where χ_{red} is the compressed POD design coefficient matrix and $\boldsymbol{X}$ is a matrix of $m \times 4$ elements ($m < 4$) with each column corresponding to a different combination of design space parameters while its rows provide the basis functions for the LSM. These basis functions have been chosen by means of physical assumptions and looking at the POD eigenvector distributions. For example, the eigenvector distribution in Fig. 6.28 shows planar curves for each axial gap and hence, gives the possibility to consider predictor functions as low order polynomials. Several relations based on physical knowledge and POD eigenvectors visualization have been tested and the ones which gave the best results in terms of error minimization between the measured data and the modelled ones have been chosen. The best predictor (or basis) functions are D, D × f^+, gap × D × f^+ and a constant. Then, from eq. 6.2,

the coefficient matrix β can be obtained by the pseudoinverse of $\mathbf{X}$ applied to ϕ_{red}. Therefore, the loss distributions in every point of the design space not participating to the education, can be estimated according to eq. 6.3:

$$C_{pt}(y) = C_{pt\_reference}(y) + \beta \boldsymbol{X} \phi_{red} \tag{6.3}$$

6.6 Prediction results

6.6.1 Incoming wakes related effects

Once tuned the smooth kernel, total pressure coefficients can be reconstructed in every point of the design space according to eq. 6.3. Results are reported in Fig. 6.30 where measured data are shown with dots for comparison. Measurement uncertainty evaluated by means of a Bayesian method for a confidence region of 3σ is reported in the plots as hatched areas [88]. Fig. 6.30(a) corresponds to the case D=2.5 mm and f^+=0.46 at low gap. As it can be seen, the model adequately reproduces the measured data in both pressure and suction side regions, as well as in the potential flow region. The incoming wake reduced frequency is varied from 0.46 to 0.575 on the top left corner (Fig. 6. 30(b)). In this case, the procedure reproduces very well the measured data. All the physical effects are well estimated: the increase of the wake peak magnitude and its position along the pitchwise direction due to wake-boundary layer interaction. Freestream losses due to wake migration are also well captured. Varying the bar diameter (Fig. 6. 30(c)) or the axial gap (Fig. 6.30(d)) do not have again significant impact on the model performance. Also in these cases, measured data are well reproduced and physical phenomena are well captured by the model. There is only a slight deviation between the peaks of the curves in Fig. 6.30(d). However, prediction remains within the measurement uncertainty. From these considerations, it can be concluded that the effects of design space parameter variation on total pressure distributions are well captured in the POD subspace (4 tested conditions) as in the original physical space constituted by 18 conditions. This reinforces the motivation of using the POD subspace as a basis to predict data in every point of the design space.

A quantitative comparison of losses predicted by the model can be done evaluating overall profile losses ω_p and comparing it to the measured data. Fig. 6.31 reports ω_p as a function of the bar diameter for the different values of incoming wake reduced frequency at the low axial gap (Fig. 6.31 (a)), and at the high axial gap (Fig. 6.31(b)). Data have been made dimensionless by the loss value at low gap for D=3.5 mm and f^+=0.575. The four conditions used for the model education are shown in black diamonds. These plots confirm the main findings deduced from the total pressure loss distributions. The model is able to reproduce the reduced frequency effect on losses measured for the different bar diameter and axial gap conditions. Note that the model provides linear results since the predictors are 4 (3 variables and a constant).

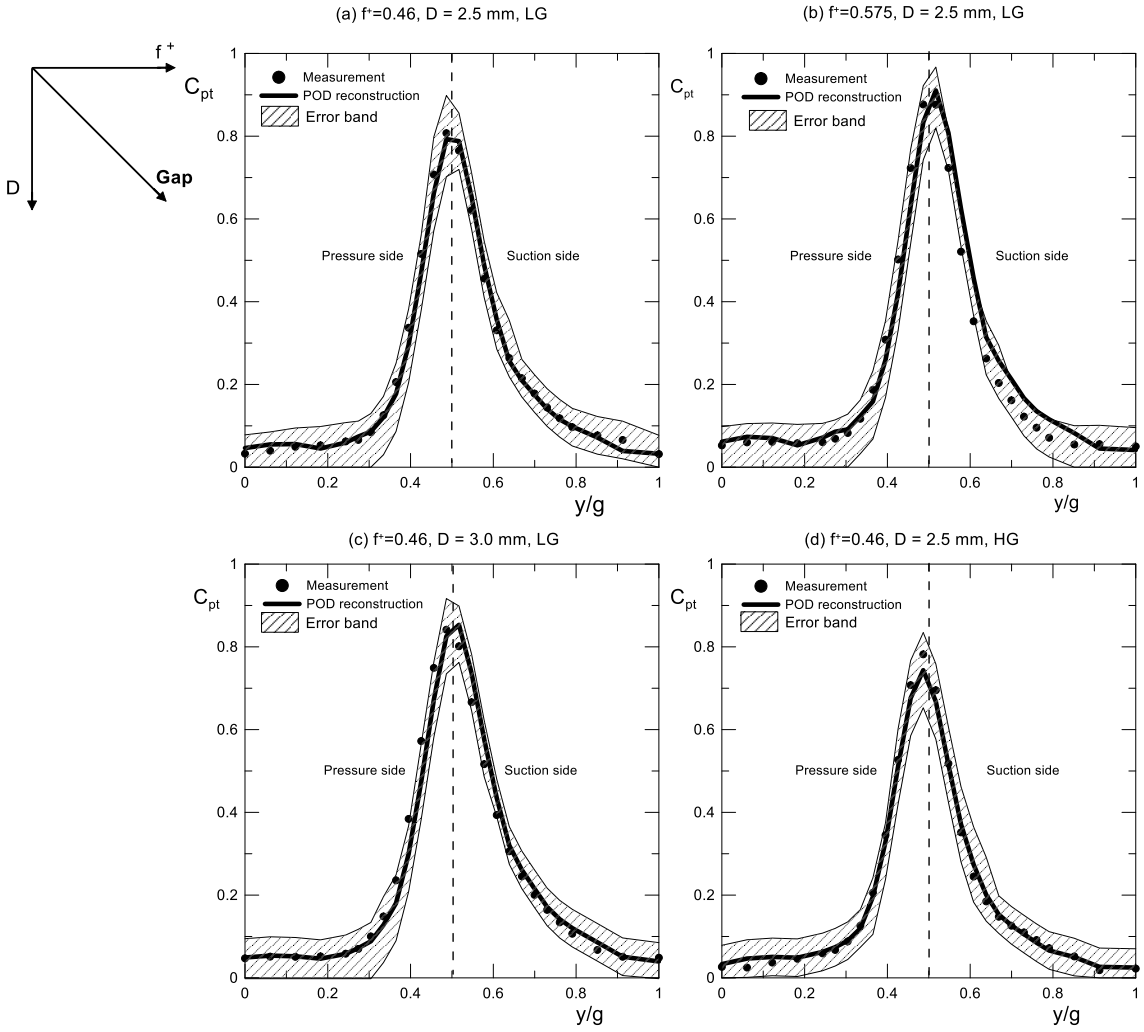

Fig. 6.30 Comparison between measured and predicted C_{pt}

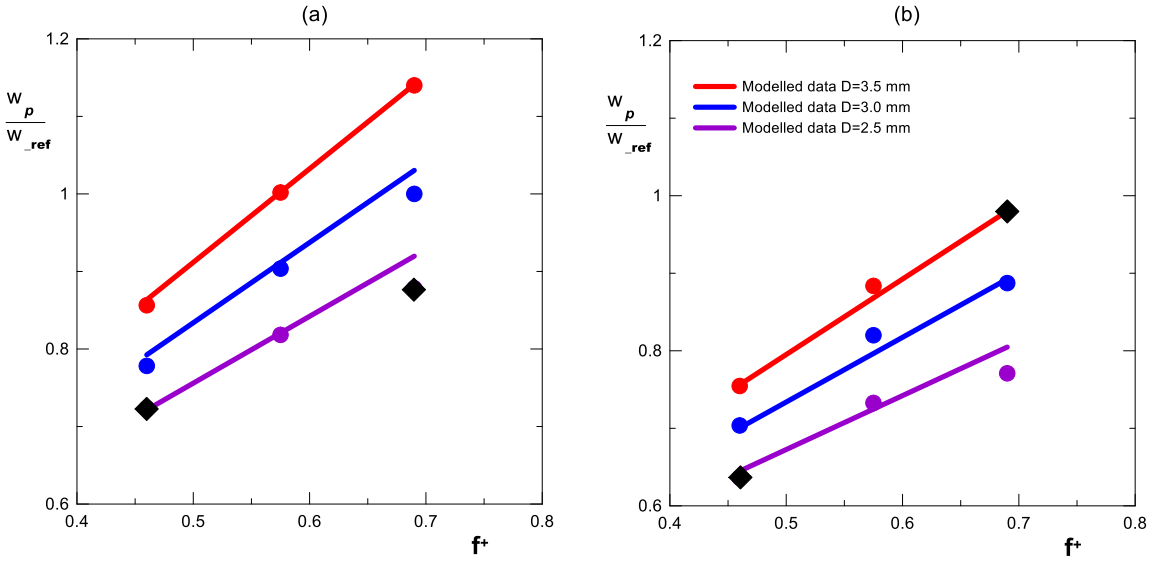

Fig. 6.31 Comparison between measured and modelled loss values at (a) LG and (b) HG

A further verification on the accuracy of the proposed POD-based technique has been provided choosing randomly four different tested conditions for the model education. Results are summarized in Fig. 6.32 where overall losses for both measured and modelled data are reported. As it can be seen, the model mimics very well the losses within the design space, making the proposed procedure independent from the chosen tested conditions. This reinforces the capability of reducing the data acquisition time by acquiring only few conditions which span each parameter variation within the design space and evaluate the remaining conditions within the design space, as a function of the acquired data.

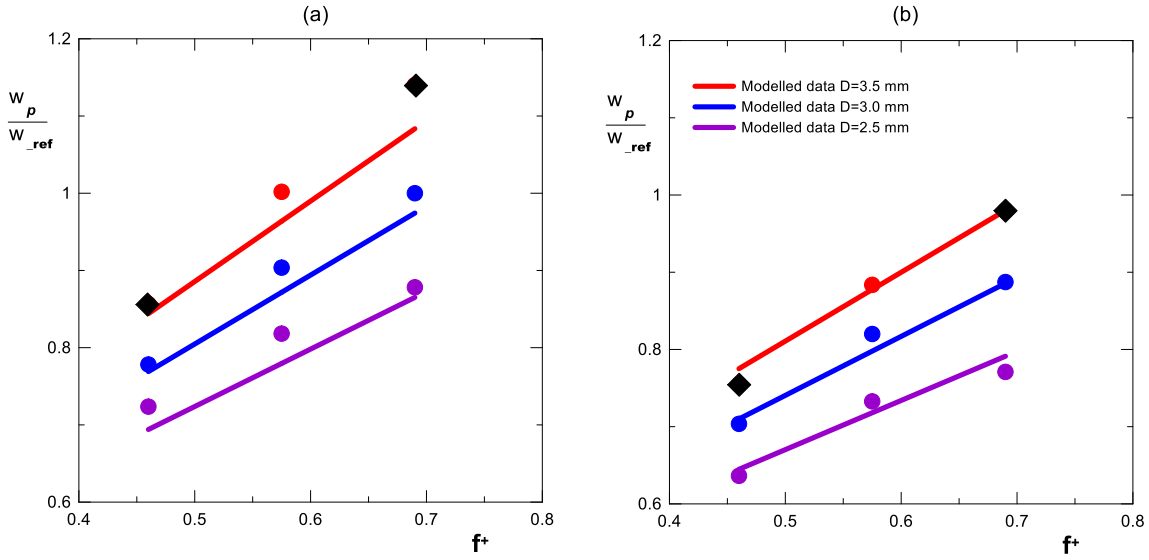

Fig. 6.32 Comparison between measured and modelled loss values with four different conditions for the model education at (a) LG and (b) HG

6.6.2 Generalization of the POD-based procedure

Since the POD-based technique previously introduced has proved its effectiveness in predicting total pressure loss distributions, it has been applied to datasets of higher dimension constituted by total pressure loss distributions acquired over two cascades characterized by significantly different deflection and solidity. This aims to further generalize the procedure exposed above. The main geometrical parameters of the cascades here considered are shown in Tab. 6.1 while the test matrix is shown in Fig. 6.33.

The total pressure distributions upstream and downstream of the cascades have been acquired by means of the experimental procedure exposed in chapter 4, The traverses have been sampled with 33 measuring points per pitch. For each measuring point 10000 samples have been collected at a sampling frequency of 1 kHz. Specifically, 30 conditions (i.e. different combination of Re number, flow coefficient and reduced frequency) for the first cascade and 36 for the second one have been acquired in order to cover real engine operative conditions.

The procedure has been applied twice this time. For the first cascade, the same steps in the same order as previously discussed have been applied while for the second cascade, the rank has been initially assumed aiming to further verify the capability of the procedure in

predicting losses. Specifically, total loss distributions of the first cascade have been arranged according to eq. 5.16 in order to apply POD. Note that in this case, the reference loss distribution is the mean of the total pressure loss distributions acquired for the different cases. As previously shown, the information derived from POD allows to identify the problem rank. In this case, the rank of the problem is 8 since 8 POD modes contain about 98% of the information, as shown by the cumulative contribution of POD modes reported in Fig. 6.34. A further verification of this rank has been done by reconstructing the original total pressure distribution using eq. 6.1. The result for the case Re = 160000, f^+ = 1.3 and φ = 0.4 is shown in Fig. 6.35 where 1^{st}, 8^{th} and full rank reconstructions are shown. It can be noted that 1^{st} order lacks in the complete loss reconstruction mainly in the peak region and also in the potential flow region. The extension to the 8^{th} order reproduces almost accurately the loss coefficient distribution in both the potential and wake regions due to the correction terms introduced by the intermediate modes (modes 2−8).

	Cascade 1	Cascade 2
Vane count	**7**	**7**
Vane chord	**100 mm**	**109 mm**
Pitch-to-chord ratio	**0.8**	**0.7**
Velocity peak position	**0.5 Cx**	**0.57 Cx**
Deflection angle	**99 deg**	**49 deg**

Tab. 6.1 Main geometrical parameters of the cascades used for the POD

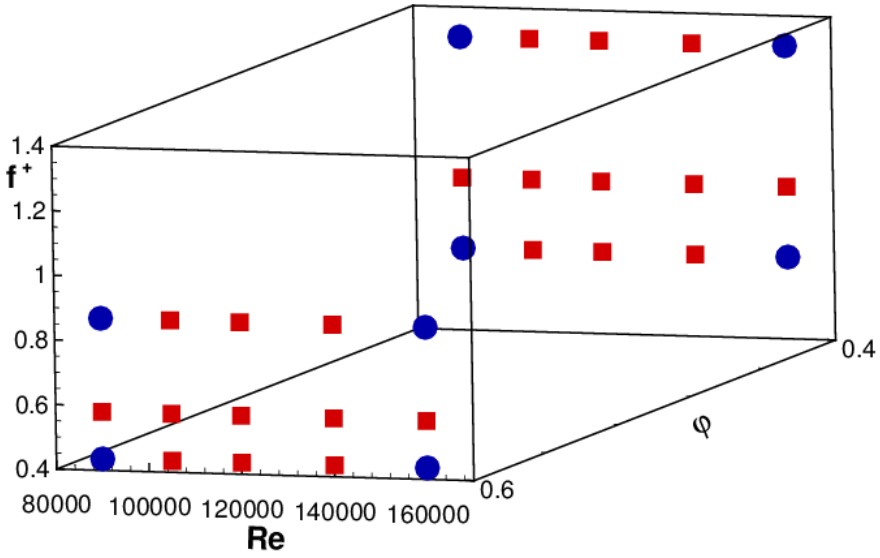

Fig. 6.33 Test matrix of experimental investigation

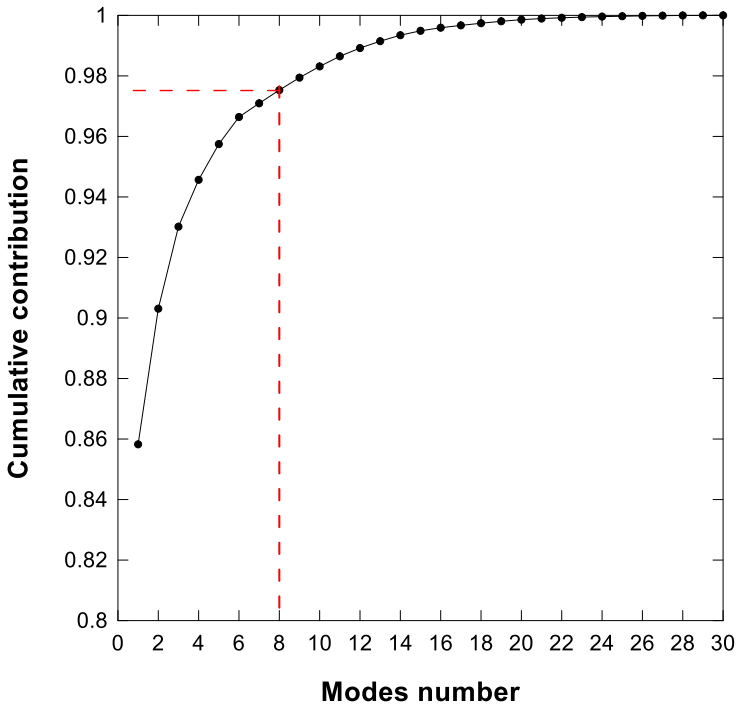

Fig. 6.34 Eigenvalues of the POD modes

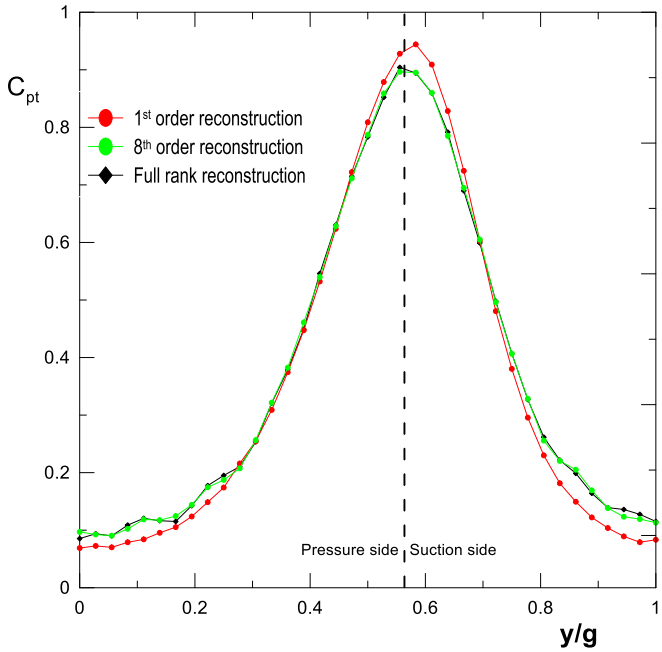

Fig. 6.35 Reduced order model representation of the loss coefficient for the case Re = 160000, f^+ = 1.3 and φ = 0.4

Now, the smooth kernel can be educated by means of LSM in the POD subspace provided by 8 conditions. In this case, the natural choice for the selection of the 8 points falls on the vertices of the cube (see blue dots in Fig. 6.33), while the best predictor functions obtained after an optimization procedure are $Re^{-0.2}$, $Re^{-0.5}$, $Re^{-0.2} \times f^+$, $Re^{-0.5} \times f^+$, $Re^{-0.2} \times \varphi$, $Re^{-0.2} \times$

$f^+ \times \varphi$ and a constant. Also in this case, physical considerations and visualization of the POD design coefficients have been considered for the evaluation of the best predictor functions.

Once tuned the smooth kernel, total pressure coefficients can be reconstructed in every point of the design space according to eq. 6.3. Results are reported in Fig. 6.35 where as previously, measured data are shown with dots for comparison. Also in this case, measurement uncertainty evaluated by means of the Bayesian method for a confidence region of 3σ, is reported in the plots as hatched areas. The four samples depicted in the pictures did not participate to the training and cover the variation of *Re*, f^+ and φ. Fig. 6.36(a) corresponds to the case *Re* = 105000, $f^+ = 0.87$ and φ = 0.4. The reader can note a good mimic between both measured and modelled data in both the pressure and suction side regions, as well as in the potential flow one. There is only a slight deviation between the peaks of the curves in this plot. However, prediction remains within the measurement uncertainty. The incoming wake reduced frequency is varied from 0.87 to 1.3 on the top left corner (Fig. 6.36(b)). Varying the incoming wake reduced frequency (Fig. 6.36(b)), the flow Reynolds number (Fig. 6.35(c)) or the flow coefficient (Fig. 6.36(d)) do not have again significant impact on the model performance. Indeed, all the physical effects are well estimated: the increase of the wake peak magnitude and its position along the pitchwise direction due to wake-boundary layer interaction. Freestream losses due to wake migration are also well captured. Once again, the effects of design space parameter variation on total pressure distributions are well captured in the POD subspace. This reinforces the motivation of using the POD subspace as a basis to predict data in every point in the design space. Additionally, looking at Fig. 6.36, it is also possible to notice that the data obtained from the POD-based procedure is smoother than the original ones, hence, the procedure acts as a filter, thus also contributing to reduce or eliminate stochastic errors corrupting the measurements (see for example [89]).

A quantitative comparison of losses predicted by the model can be done evaluating overall profile losses ω_p and comparing it to the measured data. Fig. 6.37 reports ω_p as a function of the flow Reynolds number, for the different values of incoming wake reduced frequency at the low flow coefficient, and one case at the high flow coefficient (violet curve). Data have been made dimensionless by the condition at *Re*=90000, $f^+ = 1.3$ and φ = 0.4. These plots confirm the main findings deduced from the total pressure loss distributions. The model is able to reproduce the Reynolds lapse rate measured for the different f^+ and φ conditions. Also, it clearly adjusts the loss level when the incoming wake reduced frequency is increased and exhibits also the proper sensibility to the flow coefficient variation (i.e., the lower flow coefficient the higher the losses).

Now, the potentiality of the procedure in extrapolating data is verified using the dataset of another cascade. In this latter example, the rank has been empirically tested on different combination of the flow conditions increasing their number from 8 to 10 and differences on the mode distribution below 1% have been observed. Thus, only data from 8 conditions have been used to first identify the reduced POD subspace. In the case that other flow parameters were to be included in the model, a proper redefinition of the rank should be done, for example progressively increasing the number of samples to be introduced in the snapshot matrix up to convergence. For this cascade, the conditions have been chosen with the same logic previously presented (i.e., the corners of the cube defining the design space. Additionally, also the same basis functions have been used for the education of the smooth kernel.

Fig. 6.38 summarizes the results of the loss distributions in the pitchwise direction, the measured data with measurement uncertainty are added for comparison and validation. Also in this case, only four cases are shown in order to verify the effects due to the variation of each parameter and these cases did not participate to the education of the reduced POD subspace. Fig. 6.38(a) corresponds to the condition Re = 120000, f^+ = 1.17 and φ = 0.4. Here, the model captures very well both the loss peak intensity and its position along the pitchwise direction. It can also be observed that in both the wake and potential flow regions, the two plots are practically superimposed and well within the measurement accuracy. Varying each design space parameter, i.e., moving along the arrows indicated on the top left of the figure, it can be seen that the model predicts very well the loss distributions. Only slight deviations on the wake suction side can be observed in Fig. 6.38(c). This confirms the potentiality of the proposed POD-based procedure in predicting total pressure loss distributions in the whole design space. Overall losses shown in Fig. 6.39 confirm the prediction capability of the proposed method. It can be observed that predicted data fits well the measurements and they have the same tendencies within the whole design space. The accuracy of the Reynolds lapse rate and the effects due to the parameter variation are thus adequately reproduced by the smooth kernel educated in the POD compressed space by means of 8 conditions instead of 36. This represents a powerful tool to reduce the amount of acquired data without significant degradation of accuracy. Thus, in a given design space, scale-resolving simulations and/or experimental investigations could be carried out spanning coarse grids with only limited effects on the overall estimation accuracy, once educated an appropriate smooth kernel in the POD space.

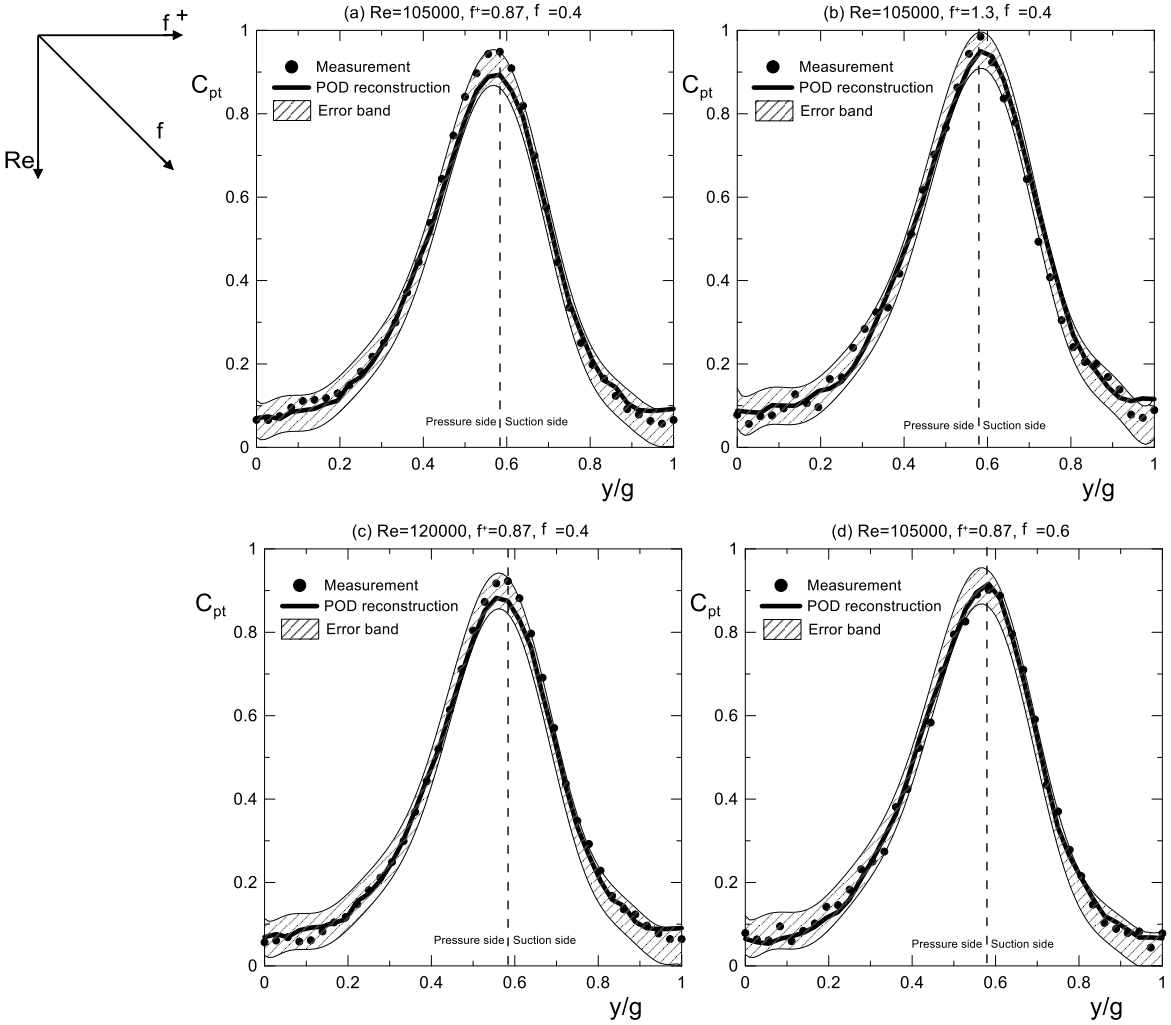

Fig. 6.36 Comparison between measured and predicted C_{pt} for the first cascade.

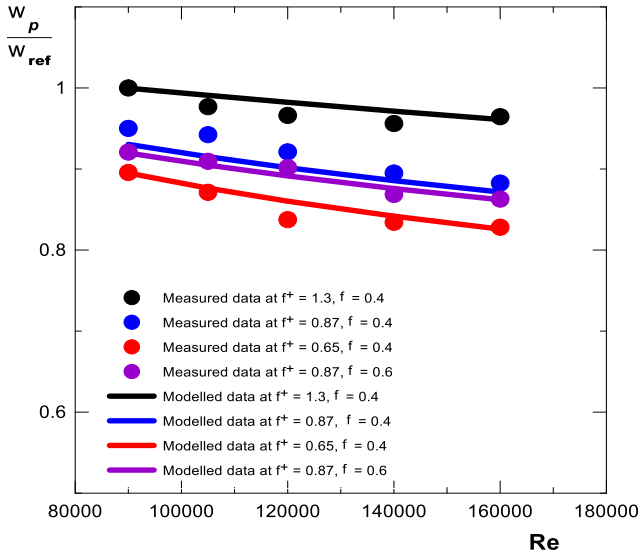

Fig. 6.37 Comparison between profile loss values of the first cascade

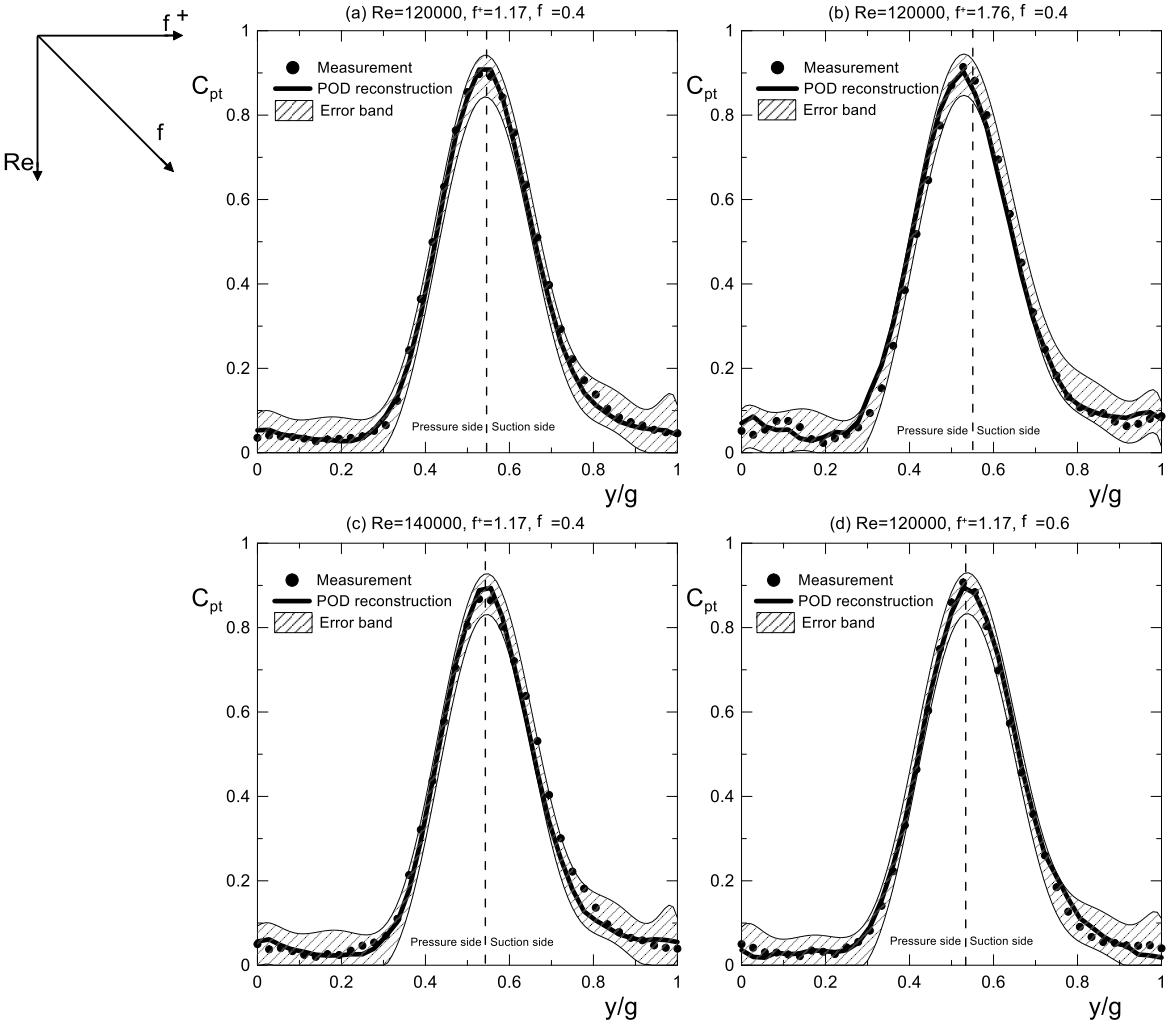

Fig. 6.38 Comparison between measured and predicted C_{pt} for the second cascade

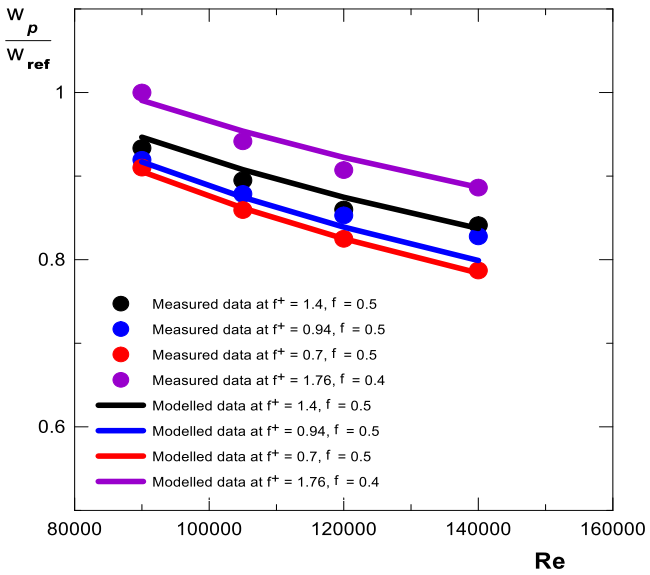

Fig. 6.39 Comparison between profile loss values of the second cascade

Chapter 7 Conclusion

In the present work experimental investigations on LPT cascades for aeronautical applications and post-processing of acquired data by means of POD have been done. Cascade testing aims to provide information to designers on the loss mechanism within LPT cascades and to give an overall view of the expected loss sensitivity to the most influencing parameters governing their operation. The numerical work instead aims to save time during experimental investigations and to reduce their cost through the identification of the number of tests really independent within a given design space.

Cascade testing have been conducted by means of an experimental technique based on the simultaneous acquisition of total pressure in both upstream and downstream of the cascade aiming to evaluate the total pressure drop and hence, the overall losses. This technique gives the possibility to discuss about the flow physics within the cascade like the wake migration and the advection of background turbulence, providing further insights on the loss mechanism while varying design parameters.

Prior to the loss evaluation, a deep characterization of both steady and unsteady inflows has been done by means of phase-locked measurements aiming to obtain different wind tunnel setups, and hence provide environment similar to real operation of an LPT stage. Therefore, loss evaluation under a large variety of design parameters has been conducted. Specifically, the effects on losses of flow Reynolds number, freestream turbulence intensity, vane solidity, incoming wakes parameters (bar diameter, bar count and axial gap) and incidence flow angle have been provided. Experimental results shown in the chapter dedicated to the results are in accordance with the literature confirming the potentiality of the experimental technique here shown in capturing the flow physics within the whole design space tested as well as providing the expected loss trend. Indeed, it has been shown that all the flow parameters tested affect mainly the upstream wake migration and its interaction with the vane suction side boundary layer. The potential flow field in the outer part of the vane wake has been shown to depend mainly on the axial gap between the moving bar system and the cascade under investigation, due to the high wake mixing prior to the cascade leading edge plane. Concerning the loss dependency, as Re, FSTI and axial gap between rotor and stator decrease losses increase. An opposite trend has been found for both incidence flow angle and wake turbulence, i.e., as they both increase LPT losses increase. The vane solidity instead, has provided a loss trend with a minimum corresponding to the intermediate value tested.

A POD-based procedure has been further developed and applied to data constituted by the total pressure loss coefficient when varying the unsteady inflow conditions following two main objectives:

i) the inspection of the unsteady losses generated in LPT cascades for different bar diameter, bar count and axial gap between rotor and stator

ii) the identification of the number of necessary conditions to be tested in this design space.

The data obtained varying the aforementioned parameters (18 conditions tested) has been shown to be adequately represented by a low-rank subspace spanned by the 4 dominant POD modes. Thus, the subspace provided by POD has been used to educate a smooth kernel with

low order polynomial functions of the influencing parameters. Results have confirmed that the kernel here educated is able to reproduce both loss distribution in the pitchwise direction and overall loss trend. Specifically, the peak loss magnitude, its position and the losses generated due to incoming wake-boundary layer interaction, as well as the loss level into the potential flow region due to incoming wake migration are well captured within the whole design space while remaining in the measurement accuracy.

The procedure has been applied to larger datasets than the previous one made of loss coefficients acquired on two cascades under the variation of different design parameters. This aimed to further generalize the predictive capability of the POD-based technique here proposed. Applied to the data obtained from a first cascade of 30 conditions, the same steps as in the previous case have been done but with diverse polynomial functions for the model education. In this specific case, the dataset has been shown to be adequately represented by a low-rank subspace spanned by 8 POD modes. Hence, a new smooth kernel has been educated with 8 tested conditions allowing the loss prediction. The kernel has been successively re-educated with data of a second cascade. During education the same low rank approximation, the same logic to sample the design space in a coarse grid, as well as the same polynomial functions have been adopted. Once again, the kernel here educated has been shown to adequately reproduce the pitchwise distribution of the loss coefficient: losses generated in the vane wake and in the potential flow region have been well modeled. Moreover, the smooth kernel also allows us to well describe the effects of reduced frequency and flow coefficient on the overall loss response.

Data reported into this work provide evidence for a generalization of the proposed procedure to coarse experiment or hi-fidelity computational test matrices, allowing for a significative reduction of time and costs. This procedure can offer a new tool for designers to optimize the unsteady operation of LPT blades when a large number of parameters are considered in the definition of the design space.

References

[1] Wisler, D. C., 1998, “The Technical and Economic Relevance of Understanding Boundary Layer Transition in Gas Turbine Engines,” Minnowbrook II, 1997 Workshop on Boundary Layer Transition in Turbomachines, J. E. LaGraff and D. E. Ashpis, eds., NASA/CP-1998-206958, pp. 53–64.

[2] Coull, J. (2017). Endwall loss in turbine cascades. Journal of Turbomachinery, 139.

[3] Dick, E. and Kubacki, S. (2017). Transition models for turbomachinery boundary layer flows: A review. International Journal of Turbomachinery, Propulsion and Power, 2(2):4.

[4] Pichler, R., Zhao, Y., Sandberg, R. D., Michelassi, V., Pacciani, R., Marconcini, M., and Arnone, A., 2019, “Large-Eddy Simulation and RANS Analysis of the End-Wall Flow in a Linear Low-Pressure Turbine Cascade, Part I: Flow and Secondary Vorticity Fields Under Varying Inlet Conditions”. ASME Journal of Turbomachinery 141(12):121005 (10 pages).

[5] Sandberg, R.D., Michelassi, V. The Current State of High-Fidelity Simulations for Main Gas Path Turbomachinery Components and Their Industrial Impact. Flow Turbulence Combust 102, 797–848 (2019).

[6] Curtis, E., Hodson, H., Banieghbal, M., Denton, J., Howell, R., and Harvey, N. (1997). Development of blade profiles for low-pressure turbine applications. Journal of Turbomachinery, 119(3):531–538.

[7] Soderberg, C. R.; 1949. Unpublished notes, Gas Turbine Laboratory, Massachusetts Institute of Technology (quoted in reference [Dixon, 1989])

[8] Coull, J. D., and Hodson, H. P., 2011. “Unsteady boundary-layer transition in low-pressure turbines”. J. Fluid Mech., 681, pp. 370–410.

[9] Simoni, D., Berrino, M., Ubaldi, M., Zunino, P., and Bertini, F. (July 1, 2015). "Off-Design Performance of a Highly Loaded Low-Pressure Turbine Cascade Under Steady and Unsteady Incoming Flow Conditions." ASME. J. Turbomach. July 2015; 137(7): 071009.

[10] Michelassi, V., Chen, L.-W., Pichler, R., and Sandberg, R. D., 2015. “Compressible direct numerical simulation of low-pressure turbines-part II: Effect of inflow disturbances”. Journal of Turbomachinery, 137(7), pp. 071005 1–12.

[11] Howell, R. J., Ramesh, O. N., Hodson, H. P., Harvey, N. W., and Schulte, V. (February 1, 2000). "High Lift and Aft-Loaded Profiles for Low-Pressure Turbines." ASME. J. Turbomach. April 2001; 123(2): 181–188.

[12] Hourmouziadis, J., 1989, “Aerodynamic Design of Low-Pressure Turbines,” AGARD Lecture Series, 167.

[13] Coull, J. D., Thomas, R. L., and Hodson, H. P. (April 27, 2010). "Velocity Distributions for Low Pressure Turbines." ASME. J. Turbomach. October 2010; 132(4): 041006.

[14] Berrino, M., Simoni, D., Ubaldi, M., Zunino, P., and Bertini, F. "Aerodynamic Loading Distribution Effects on Off-Design Performance of Highly Loaded LP Turbine Cascades Under Steady and Unsteady Incoming Flows." Proceedings of the ASME Turbo Expo 2016: Turbomachinery Technical Conference and Exposition. Volume 2B: Turbomachinery. Seoul, South Korea. June 13–17, 2016. V02BT38A048. ASME.

[15] Denton, J. D., 1993, "Loss Mechanisms in Turbomachines", ASME Journal of Turbomachinery, 115, pp. 621-656.

[16] Satta F., Simoni D., Ubaldi M., Zunino P., Bertini F., 2012, "Profile and Secondary Flow Losses in a High-Lift LPT Blade Cascade at Different Reynolds Numbers under Steady and Unsteady Inflow Conditions", Journal of Thermal Science, 21 (6), pp. 483-491.

[17] Giovannini, M., Rubechini, F., Marconcini, M., Simoni, D., Yepmo, V., and Bertini, F. (October 8, 2018). "Secondary Flows in Low-Pressure Turbines Cascades: Numerical and Experimental Investigation of the Impact of the Inner Part of the Boundary Layer." ASME. J. Turbomach. November 2018; 140(11): 111002.

[18] Marconcini, M., Pacciani, R., Arnone, A., Michelassi, V., Pichler, R., Zhao, Y., and Sandberg, R. (January 21, 2019). "Large Eddy Simulation and RANS Analysis of the End-Wall Flow in a Linear Low-Pressure-Turbine Cascade—Part II: Loss Generation." ASME. J. Turbomach. May 2019; 141(5): 051004.

[19] Sirovich, L., 1987. "Turbulence and the dynamics of coherent structures. part I-III". Q Appl Math, 45, pp. 561– 590.

[20] Berkooz, G., Holmes, P., and Lumley, J. L., 1993. "The proper orthogonal decomposition in the analysis of turbulent flows". Annual review of fluid mechanics, 25(1), pp. 539–575.

[21] Prandtl, L. (1904). Verhandlungen des dritten internationalen mathematiker-kongresses. Heidelberg, Leipeizig, pages 484–491.

[22] Anderson Jr, J. D. (2010). Fundamentals of aerodynamics. Tata McGraw-Hill Education

[23] Schlichting, H., "Boundary Layer theory", Mc Graw Hill, New York, (1979).

[24] Mayle, R. E. (October 1, 1991). "The 1991 IGTI Scholar Lecture: The Role of Laminar-Turbulent Transition in Gas Turbine Engines." ASME. J. Turbomach. October 1991; 113(4): 509–536.

[25] Zaki, T., 2013, "From Streaks to Spots and on to Turbulence: Exploring the Dynamics of Boundary Layer Transition", Flow Turbulence and Combustion, 91, pp. 451–473.

[26] Jacobs, R. G., Durbin, P. A., 2001, “Simulations of bypass transition”, Journal of Fluid Mechanics, 428, pp. 185-212.

[27] Hack, M.J.P.; Zaki, T.A. Streak instabilities in boundary layers beneath free-stream turbulence. J. Fluid Mech. 2014, 741, 280–315.

[28] Xu, Z.; Zhao, Q.; Lin, Q.; Xu, J. Large eddy simulation on the effect of free-stream turbulence on bypass transition. Int. J. Heat Fluid Flow 2015, 54, 131–142

[29] H. W. Emmons. The Laminar-Turbulent Transition in a Boundary Layer - Part I. Journal of Aeronautical Sciences, 18:490{498, July 1951. xxi, 13, 14, 15

[30] Schubauer GB, Klebanoff PS. Contributions on the mechanics of boundary layer transition. NACA TN 3489 and NACA rep1289.

[31] Jeon, W. P., Park, T. C., Kang, S. H., 2002, “Experimental Study of Boundary-Layer Transition on an Airfoil Induced by Periodically Passing Wake,” Experiments in Fluid, 32, pp. 229-241.

[32] Hodson, H. P., and Howell, R. J., 2005. “The role of transition in high-lift low-pressure turbines for aeroengines”. Prog. in Aerospace Sci., 41, pp. 419–454.

[33] Hatman A, Wang T. Separated-flow transition part 1— experimental methodology and mode classification. Presented at the ASME turbo expo, Stockholm, Sweden; 1998.

[34] Hatman A, Wang T. Separated-flow transition part 2— experimental results. Presented at the ASME turbo expo, Stockholm, Sweden, 1998.

[35] Hatman A, Wang T. Separated-flow transition part 3— primary modes and vortex dynamics. Presented at the ASME turbo expo, Stockholm, Sweden, 1998.

[36] Hatman A, Wang T. A prediction model for separated flow transition. Presented at the ASME turbo expo, Stockholm, Sweden, 1998.

[37] Speidel L., Beebinflussung der laminaren Grezschicht durch periodische Strbrungen der Zustr6mung, Z. Flugwiss. 9 (1957) 5.

[38] Meyer RX. The effect of wakes on the transient pressure and velocity distributions in turbomachines. ASME J Basic Eng, October 1958; 1544–52.

[39] Hodson HP. The development of unsteady boundary layers on the rotor of an axial-flow turbine. AGARD conference on viscous effects in turbomachines, AGARD CP-351, Copenhagen, June 1983.

[40] Hodson, H. P., and Dawes, W. N. (April 1, 1998). "On the Interpretation of Measured Profile Losses in Unsteady Wake–Turbine Blade Interaction Studies." ASME. J. Turbomach. April 1998; 120(2): 276–284

[41] Pfeil, H., Eifler, J., 1976, “Turbulenzverhältnisse Hinter Rotierenden Zylindergittern”, Forschung im Ingenieurwesen, 42, pp.27-32.

[42] Wu, X., Jacobs, R., Hunt, J. C. R., and Durbin, P. A., 2001, “Evidence of Longitudinal Vortices Evolved from Distorted Wakes in a Turbine Passage”. Journal of Fluid Mechanics, 446, pp. 199–228.

[43] Michelassi, V., Wissink, J. G., Rodi, W., 2002, “Analysis of DNS and LES of Flow in a Low-Pressure Turbine Cascade with Incoming Wakes and Comparison with Experiments”, Flow Turbulence and Combustion, 69, pp. 295-329.

[44] Stieger, R. D., and Hodson, H. P. (May 5, 2005). "The Unsteady Development of a Turbulent Wake Through a Downstream Low-Pressure Turbine Blade Passage." ASME. J. Turbomach. April 2005; 127(2): 388–394.

[45] Wissink, J.G., Rodi, W., Hodson, H.P.: The influence of disturbances carried by periodically incoming wakes on the separating flow around a turbine blade. Int. J. Heat Fluid Flow 27, 721–729 (2006)

[46] H. Pfeil, R. Herbst, and T. Schroder. Investigation of the Laminar-Turbulent Transition of Boundary Layers Disturbed by Wakes. ASME Journal of Engineering for Power, 105(1):130{137, January 1983. xxi, 13, 14, 19, 21

[47] Hammer, F.; Sandham, N.D.; Sandberg, R.D. The Influence of Different Wake Profiles on Losses in a Low-Pressure Turbine Cascade. Int. J. Turbomach. Propuls. Power 2018, 3, 10.

[48] Simoni, D., Ubaldi, M., Zunino, P.: Experimental investigation of the interaction between incoming wakes and instability mechanisms in a laminar separation bubble. Exp. Therm. Fluid Sci. 50, 54–60 (2013)

[49] Sarkar, S. Influence of Wake Structure on Unsteady Flow in a Low-Pressure Turbine Blade Passage. J. Turbomach. 2009, 131, 041016.

[50] Michelassi, V.; Chen, L.W.; Pichler, R.; Sandberg, R.; Bhaskaran, R. High-Fidelity Simulations of Low-Pressure Turbines: Effect of Flow Coefficient and Reduced Frequency on Losses. J. Turbomach. 2016, 138, 111006.

[51] Pichler, R.; Michelassi, V.; Sandberg, R.; Ong, J. Highly Resolved Large Eddy Simulation Study of Gap Size Effect on Low-Pressure Turbine Stage. J. Turbomach. 2017, 140, 021003.

[52] Zhang, X. F., and Hodson, H. (September 18, 2009). "Effects of Reynolds Number and Freestream Turbulence Intensity on the Unsteady Boundary Layer Development on an Ultra-High-Lift Low Pressure Turbine Airfoil." ASME. J. Turbomach. January 2010; 132(1): 011016.

[53] Volino, R. J., 2002, “Separated Flow Transition Under Simulated Low-Pressure Turbine Airfoil Conditions—Part 1: Mean Flow and Turbulence Statistics”, ASME Journal of Turbomachinery, 124, pp. 645–655.

[54] Volino, R. J., 2002, “Separated Flow Transition Under Simulated Low-Pressure Turbine Airfoil Conditions—Part 2: Turbulence Spectra”, ASME Journal of Turbomachinery, 124, pp. 656-664.

[55] Schreiber, H.-A., Steinert, W., and Kusters, B. (2000). Effects of Reynolds number and free-stream turbulence on boundary layer transition in a compressor cascade. In ASME Turbo Expo 2000: Power for Land, Sea, and Air, pages V003T01A068–V003T01A068. American Society of Mechanical Engineers

[56] Hall, D. and Gibbings, J. (1972). Influence of stream turbulence and pressure gradient upon boundary layer transition. Journal of Mechanical Engineering Science, 14(2):134–146.

[57] Abu-Ghannam, B. and Shaw, R. (1980a). Natural transition of boundary layers—the effects of turbulence, pressure gradient, and flow history. Journal of Mechanical Engineering Science, 22(5):213–228.

[58] Dhawan, S. and Narasimha, R. (1958). Some properties of boundary layer flow during the transition from laminar to turbulent motion. Journal of Fluid Mechanics, 3(4):418–436.

[59] Suzen, Y. B., Huang, P., Hultgren, L. S., and Ashpis, D. E. (2003). Predictions of separated and transitional boundary layers under low-pressure turbine airfoil conditions using an intermittency transport equation. Journal of Turbomachinery, 125(3):455–464.

[60] Dunham, J. (1972). Prediction of boundary layer transition on turbomachinery blades. In AGARD meeting on boundary layers in turbomachines, 1972.

[61] Thwaites, B. (1949). Approximate calculation of the laminar boundary layer. The Aeronautical Quarterly, 1(3):245–280.

[62] Ainley, D. G., and Mathieson, G. C. R., 1951, “A Method of Performance Estimation for Axial-Flow Turbines,” ARC Reports and Memoranda No. 2974.

[63] Craig, H., and Cox, H., 1970. “Performance estimation of axial flow turbines”. Proceedings of the Institution of Mechanical Engineers, 185(1), pp. 407–424.

[64] Dunham, J., and Came, P. M., 1970, “Improvements to the Ainley–Mathieson Method of Turbine Performance Prediction,” ASME J. Eng. Power 0022-0825, A92, pp. 252–256

[65] Kacker, S., and Okapuu, U., 1982. “A mean line prediction method for axial flow turbine efficiency”. Journal ofengineering for power, 104(1), pp. 111–119.

[66] Coull, J. D., and Hodson, H. P., 2012. “Predicting the profile loss of high-lift low pressure turbines”. Journal of turbomachinery, 134(2), p. 021002.

[67] Coull, J. D., and Hodson, H. P., 2013. “Blade loading and its application in the mean-line design of low-pressure turbines”. Journal of Turbomachinery, 135(2), p. 021032.

[68] Lumley, J. L. (1970). Stochastic tools in turbulence. Applied Mathematics and Mechanics,
vol. 12.

[69] Sirovich, L. (1987). Turbulence and the dynamics of coherent structures. part I-III. Q Appl Math, 45:561–590

[70] Payne, Lumley, “Large eddy structure of the turbulent wake behind a circular cylinder”, Phys. Fluids (1967), 10(9, part 2), pp. 194-196

[71] Lengani, D., Simoni, D., Ubaldi, M., Zunino, P.: POD analysis of the unsteady behavior of a laminar separation bubble. Exp. Therm. Fluid Sci. 58, 70–79 (2014)

[72] Lengani, D., Simoni, D., Ubaldi, M., Zunino, P., Bertini, F., and Michelassi, V., 2017. “Accurate estimation of profile losses and analysis of loss generation mechanisms in a turbine cascade”. Journal of Turbomachinery, 139(12), p. 121007.

[73] Lengani, D., Simoni, D., Pichler, R., Sandberg, R., Michelassi, V., and Bertini, F., 2018. “Identification and quantification of losses in an LPT cascade by POD applied to LES data”. International Journal of Heat and Fluid Flow, 70, pp. 28–40.

[74] Lengani, D., Simoni, D., Pichler, R., Sandberg, R., Michelassi, V., and Bertini, F., 2019. “On the identification and decomposition of the unsteady losses in a turbine cascade”. Journal of Turbomachinery, 141(3), p. 031005.

[75] Daniele, S., Dario, B., Matteo, D. et al. Modified Formulation of Laminar Kinetic Energy Transition Models by Means of Elastic-Net of a Big Experimental Database of Separated Flows. Flow Turbulence Combust 105, 671–697 (2020).

[76] Hussain, A., Reynolds, W.: The mechanics of an organized wave in turbulent shear flow. J. Fluid Mech. 41, 241–258 (1970)

[77] Laurent Graftieaux et al 2001 Meas. Sci. Technol. 12 1422.

[78] Van Oudheusden, B.W., Scarano, F., van Hinsberg, N.P., Watt, D.W.: Phase-resolved characterization of vortex shedding in the near wake of a square-section cylinder at incidence. Exp. Fluids 39, 86–98 (2005)

[79] Legrand, M., Nogueira, J., Tachibana, S., Lecuona, A., and Nauri, S. (2011b). Flow temporal reconstruction from non-time-resolved data part II: practical implementation, methodology validation, and applications. Exp. Fluids, 51(4):861–870.

[80] Lengani, D. and Simoni, D. (2015a). Recognition of coherent structures in the boundary layer of a low-pressure-turbine blade for different free-stream turbulence intensity levels. International Journal of Heat and Fluid Flow, 54:1–13.

[81] Davide, L., Simoni, D., Ubaldi, M. et al. Coherent Structures Formation During Wake-Boundary Layer Interaction on a LP Turbine Blade. Flow Turbulence Combust 98, 57–81 (2017)

[82] C.W. Rowley, T. Colonius, R.M. Murray, Model reduction for compressible flows using POD and Galerkin projection, Physica D: Nonlinear Phenom. 189 (2004) 115–129

[83] Noack, B. R., Papas, P., and Monkewitz, P. A., "The Need for a Pressure-Term Representation in Empirical Galerkin Models of Incompressible Shear Flows," Journal of Fluid Mechanics, Vol. 523, Jan. 2005, pp. 339–365.

[84] Bui-Thanh, T., Damodaran, M., and Wilcox, K., "Aerodynamic Data Reconstruction and Inverse Design Using Proper Orthogonal Decomposition," AIAA Journal, Vol. 42, No. 8, 2004, pp. 1505–1516.

[85] Dolci, Valentina; Arina, Renzo (2016). Proper orthogonal decomposition as surrogate model for aerodynamic optimization. In: INTERNATIONAL JOURNAL OF AEROSPACE ENGINEERING (ONLINE), vol. Volume 2016. - ISSN 1687-5974

[86] Kutz, J. N., 2013. Data-Driven Modeling & Scientific Computation: Methods for Complex Systems & Big Data

[87] Dellacasagrande, M., Barsi, D., Lengani, D. et al. Response of a flat plate laminar separation bubble to Reynolds number, free-stream turbulence and adverse pressure gradient variation. Exp Fluids 61, 128 (2020).

[88] Simoni, D., Lengani, D., Petronio, D., and Bertini, F. "A bayesian approach for the identification of cascade loss model strategy". In ASME Turbo Expo 2020: Turbomachinery Technical Conference and Exposition, ASME paper no. GT2020-14625.

[89] Raiola, M., Discetti, S., and Ianiro, A., 2015. "On PIV random error minimization with optimal POD-based low-order reconstruction". Experiments in Fluids, 56(4), p. 75.